STARS

University of Central Florida
STARS

Electronic Theses and Dissertations, 2004-2019

2010

Structural Characterization Of Sputter-deposited Ss304+xal (x = 0, 4, 7 And 10 Wt.%) Coatings And Mechanically Milled Ti, Zr And

Uma Maheswara Seelam
University of Central Florida

 Part of the Materials Science and Engineering Commons
Find similar works at: https://stars.library.ucf.edu/etd
University of Central Florida Libraries http://library.ucf.edu

This Doctoral Dissertation (Open Access) is brought to you for free and open access by STARS. It has been accepted for inclusion in Electronic Theses and Dissertations, 2004-2019 by an authorized administrator of STARS. For more information, please contact STARS@ucf.edu.

STARS Citation
Seelam, Uma Maheswara, "Structural Characterization Of Sputter-deposited Ss304+xal (x = 0, 4, 7 And 10 Wt.%) Coatings And Mechanically Milled Ti, Zr And" (2010). *Electronic Theses and Dissertations, 2004-2019*. 4206.
https://stars.library.ucf.edu/etd/4206

STRUCTURAL CHARACTERIZATION OF SPUTTER-DEPOSITED SS304+xAl (x = 0, 4, 7 AND 10 Wt.%) COATINGS AND MECHANICALLY MILLED Ti, Zr AND Hf POWDERS

by

UMA MAHESWARA RAO SEELAM

M.S., Banaras Hindu University, Varanasi, India (2004)

B.S., Indian Institute of Metals, Kolkata, India (2002)

A dissertation submitted in partial fulfillment of the requirements
for the degree of Doctor of Philosophy
in the Department of Mechanical, Materials and Aerospace Engineering
in the College of Engineering and Computer Science
at the University of Central Florida
Orlando, Florida

Spring Term
2010

Major Professor: C. Suryanarayana

© 2010 Uma Maheswara Rao Seelam

ABSTRACT

Study of the metastable phases obtained by non-equilibrium processing techniques has come a long way during the past five decades. New metastable phases have often given new perspectives to the research on synthesis of novel materials systems. Metastable materials produced by two non-equilibrium processing methods were studied for this dissertation- 304-type austenitic stainless steel (SS304 or Fe-18Cr-8Ni)+aluminum coatings produced by plasma enhanced magnetron sputter-deposition (PEMS) and nanocrystalline Ti, Zr and Hf powders processed by mechanical milling (MM). The objective of the study was to understand the crystallographic and microstructural aspects of these materials.

Four SS304+Al coatings with a nominal Al percentages of 0, 4, 7 and 10 wt.% in the coatings were deposited on an SS304 substrate by PEMS using SS304 and Al targets. The as-deposited coatings were characterized by x-ray diffraction (XRD), scanning electron microscopy (SEM), transmission electron microscopy (TEM) and three-dimensional atom probe microscopy (3DAP). Surface morphology and chemical analysis were studied by SEM. Phase identification was carried out by XRD and TEM. The microstructural features of all the coatings, as observed in the TEM, consisted of columnar grains with the columnar grain width (a measure of grain size) increasing with an increase in the Al content. The coatings had grains with average grain sizes of about 100, 290, 320 and 980 nm, respectively for 0, 4, 7 and 10 wt.% Al. The observed grain structures and increase in grain size were related to substrate temperature during deposition. XRD results indicated that the Al-free coating consisted of the non-equilibrium ferrite and sigma phases. In the 4Al, 7Al and 10Al coatings, equilibrium ferrite and B2 phases were observed but no sigma phase was found. In 10Al coating, we were able to demonstrate

experimentally using 3DAP studies that NiAl phase formation is preferred over the FeAl phase at nano scale.

During mechanical milling of the hexagonal close packed (HCP) metals Hf, Ti and Zr powders, unknown nanocrystalline phases with face centered cubic (FCC) structure were found. The FCC phases could be either allotropes of the respective metals or impurity stabilized phases. However, upon MM under high purity conditions, it was revealed that the FCC phases were impurity stabilized. The decrease in crystallite size down to nanometer levels, an increase in atomic volume, lattice strain, and possible contamination were the factors responsible for the transformation.

ACKNOWLEDGMENTS

First and foremost, the person I wish to thank is my advisor, Prof. C. Suryanarayana, for his guidance all through my doctoral program. He created funding opportunities for my current research and took the initiative to send me to the National Institute for Materials Science (NIMS) in Japan after seeing my interest in the field of electron microscopy. This made it possible for me to realize my passion for characterization of materials using advanced microscopy techniques. In addition, he has entrusted me with immense academic freedom in my choice of course work, research projects and working hours. Further, he has critically and patiently corrected my dissertation chapters and other manuscripts.

I would also like to thank Prof. Surya for his teaching. His courses 'Physical Metallurgy' and 'Crystallography and X-ray Diffraction' led me to discover answers to many of the subjective questions I had from my earlier education.

In addition, I sincerely thank all my other committee members— Dr. Helge Heinrich, Dr. N. Sastry Cheruvu, Dr.Kevin Coffey, Dr.Raj Vaidyanathan and Dr. Linan An—for their continual guidance and support.

I will never forget Dr. Heinrich here at UCF who helped me on several occasions in preparing my TEM samples and trained me on the advanced TEM techniques. Without his help, the coatings work would not have reached its current level of development.

Dr. N.S. Cheruvu of the Southwest Research Institute (SwRI) showed his willingness to help by sending me coated samples and relevant scientific information. Also, he made time for many telephone conversations which were useful in understanding experimental issues related to the coatings.

Dr. Kevin Coffey's critical research directions on several issues related to the sputter-deposition gave me insight and kept me on the track of positive thinking in my research on coatings. Dr.Raj Vaidyanathan and Dr. Linan An provided me valuable feedback on my research. Dr.Raj also gave suggestions on career possibilities. Again, I extend my thanks to all the members of my committee, as listed above.

In addition to the committee, I appreciate the help from Dr. R. Wei (SwRI, Texas), Dr. G. Barkhordarian (GKSS Research Center, Germany) and Dr. E. Ivanov (Tosoh SMD, Ohio). Dr. Wei gave me critical information several times on the conditions under which the coatings were prepared which eventually led me to correlate the effect of processing conditions on the microstructure. Dr. Barkhordarian carried out ultra high purity mechanical milling experiments, and Dr. Ivanov provided the chemical analysis of milled powders.

The most fruitful days of my research passed in NIMS during my visit in summer 2008 where I spent about 50 days doing the major part of my experimental work. My confidence in my results on coatings stems from my work in NIMS. I sincerely thank Prof. K. Hono, first, for accepting me for the Open Research Institute (ORI) fellowship program; second, for allowing me to work freely in his lab using their resources; and, finally, for guiding me at NIMS. I am also grateful to Dr. Ohkubo for his help in TEM and atom probe microscopy of my samples. Further, I thank each and every one of the Nanostructure Analysis Group at NIMS who helped me in many ways. I am grateful to them all.

I also thank Prof. Vimal Desai, former Director of AMPAC, UCF for admitting me with full funding, and also the former Chairs of MMAE, Dr. R. Kumar and Dr. D. Nicholson for

continuing my department teaching assistantship. I extend thanks to the staff and engineers at the Department of MMAE and Materials Characterization Facility (MCF) for their help.

I am grateful to my many friends at UCF. My roommates Arun, Anup, Afsaan, Sudip and Zahid contributed to peaceful living during the past four years. Dr. Hanif Khallaf, Kishore, Dr. Narayana, Bindu, Dr. Bo Yao, Dr. Sachin, Andrew Warren, Dr. Satyajeet, Dr. Mahadevan, and Dr. Prabhakar are among the many other friends and colleagues who helped me in various ways.

The support I receive from my family is very valuable to me. The love and faith of my mother and late father sustained me during this entire process. I thank my two sisters and brother for their invaluable support at crucial times. My maternal uncle D. Samba Siva Rao, and my advisors at Banaras Hindu University, Prof. G.V.S. Sastry and Prof. N.K. Mukhopadhyay, strongly supported and encouraged me in my higher studies in the USA.

I am grateful to the following funding sources: 1) AMPAC for the first year fellowship, 2) The Department of MMAE for supporting me as a TA for 8 semesters, 3) The SwRI, 4) ORI fellowship from NIMS, 5) Tuition waivers and travel grants from the Graduate Studies, UCF, and 6) Travel awards from the Student Government Association (SGA), UCF.

Finally, I extend my gratitude to all my teachers in MMAE/APMAC of UCF. The classroom experience at UCF is something that I am certainly grateful for. UCF has given me several resources for active learning, professional development and self-improvement. On the whole, my study here has led me to a broader vision of the world, allowing me to think beyond materials science. Hence I dedicate my dissertation to the University of Central Florida with my deepest respect.

This thesis is dedicated to:

The University of Central Florida

and

My Parents

TABLE OF CONTENTS

LIST OF FIGURES

LIST OF TABLES

LIST OF ABBREVIATIONS

3DAP:	Three-Dimensional Atom Probe
BCC	Body Centered Cubic
BF:	Bright Field
DF:	Dark Field
DP:	Diffraction Pattern
EDS:	Energy Dispersive Spectroscopy
EELS:	Electron Energy Loss Spectroscopy
EFTEM:	Energy Filtered Transmission Electron Microscopy
FCC:	Face Centered Cubic
FIB:	Focused Ion Beam
GIF:	Gatan Imaging Filter
GSZ:	Grain Structure Zone
HAADF:	High Angle Annular Dark Field
HCP	Hexagonal Close Packed
HRTEM:	High Resolution Transmission Electron Microscopy
IM:	Ion Milling
MA:	Mechanical Alloying
MM:	Mechanical Milling
NBD:	Nano Beam Diffraction
NDT:	Normalized Deposition Temperature
PEMS:	Plasma-Enhanced Magnetron Sputter-Deposition
PVD:	Physical Vapor Deposition
SADP:	Selected Area Diffraction Pattern
SEM:	Scanning Electron Microscopy
SS304:	Stainless Steel 304 (Austenitic grade steel with 18Cr-8Ni)
STEM:	Scanning Transmission Electron Microscopy
SwRI:	Southwest Research Institute, San Antonio, Texas
TEM:	Transmission Electron Microscopy
XRD:	X-ray Diffraction

CHAPTER 1: INTRODUCTION

1.1. Metastable Phases

Equilibrium is the state of minimum energy. It is usual that materials always tend to reach their equilibrium state. Given sufficient time, the minimum energy state is achieved. But sometimes, a state, which is not at the lowest energy level, can appear and continue to be present for a very long period of time. This particular state is called a metastable state. With respect to materials, several microconstituents can exhibit metastable states. Materials containing these metastable microconstituents (or metastable phases) can often possess properties better than the materials containing only equilibrium phases. One of the finest examples is the martensite phase in steels. The martensite is the responsible phase for the higher strength and hardness in carbon steels and martensitic stainless steels.

Metastable phases can be produced by variety of different non-equilibrium processing (NEP) methods [1]. Rapid solidification processing (RSP) [2], physical vapor-deposition (PVD) [3] and mechanical alloying/milling (MA/MM) [4] are some of the non-equilibrium processing techniques which are capable of producing metastable phases.

Two NEP techniques were used in the present investigation to study the metastable effects. They are sputter-deposition and mechanical milling. Sputter-deposition is one of the PVD processing techniques that is commonly used in thin film industry, while mechanical milling is a common industrial technique to produce ODS alloys.

1.2. Magnetron Sputter-Deposited Coatings

The increasing requirement for high technology materials with specific performance characteristics in various types of environments has dictated the use of new materials that possess near-surface properties different from their bulk properties. Coatings or surface modification treatments serve this purpose.

Magnetron sputter-deposition is a coating or deposition method which is widely known in the thin film industry. It is a process carried out in vacuum. It involves the use of ions from a gas-generated plasma to dislodge coating atoms or molecules from a target made of the material that will become the coating [5]. The coating thickness varies from a few nanometers to a few microns depending on the application. While the thickness is a few nanometers for the electronics applications, it could be a few micrometers for the hard coating applications [5-7].

One of the possible results of magnetron sputtering is the synthesis of coatings with extremely small grain sizes down to nanometer level. Nanocrystalline coatings produced by sputter deposition have been observed to possess superior resistance to high temperature cyclic oxidation [8-10]. Since the work of Wang in 1997 [8], there has been plenty of interest in the area of cyclic oxidation behavior of nanocrystalline materials. Several researchers produced nanocrystalline coatings and tested and found their cyclic oxidation response to be superior [11-13]. The main reason for the superior cyclic oxidation resistance was due to the greater mechanical stability of the oxide scale on nanocrystalline coatings compared to coarse-grained materials. Further, small quantities of oxidizing elements were enough to produce oxide scale because of their faster diffusivity through the grain boundaries in materials. Once the oxide scale forms, since its spallation resistance is very high compared to coarse-grained materials, it could protect the coated materials for long term.

1.3. Sputter-Deposited Stainless Steel 304+Al Coatings and Motivation

Most of the earlier research on nanocrystalline coatings and cyclic oxidation resistance was limited to a few tens to a few hundreds of hours. However, in order to use them in industrial applications, they need to be tested for longer durations. With this basic idea, Southwest Research Institute (SwRI) synthesized four stainless steel 304 (SS304)+Al coatings (0 to 10 wt.% Al in 304-steel) by sputter-deposition on SS304 substrate. Al has been chosen since it can resist the high temperature cyclic oxidation better than Cr. SwRI tested the sputter deposited coatings for 1000 cycles, each cycle constituting 50 minutes of heating at 750 °C and 10 minutes of cooling in air. The results of the cyclic oxidation showed excellent cyclic oxidation resistance of the Al added SS304 coatings compared to uncoated SS304 [14]. In order to correlate the cyclic oxidation resistance with microstructural features of the as-deposited, it was decided to conduct a detailed characterization of the coatings for their crystal structure and microstructure.

1.4. Objectives of the Present Work

The objectives of the present investigation are listed below.

(1) Studying the grain size of SS304+Al coatings,

(2) Studying the influence of Al on phase formation and microstructure,

(3) Understanding the metastable phase formation in these coatings, and finally

(4) Understanding the influence of experimental parameters of sputter-deposition on the coating microstructure.

1.5. Mechanical Milling of Hf, Ti and Zr Powders and Objectives

Mechanical milling (MM) is another NEP technique used in the present investigation on metastable phases. This process involves repeated cold welding, fracturing, and rewelding of powder particles in a high-energy ball mill. MM results in structural and microstructural modifications including formation of metastable phases, phase transformations, and synthesis of materials with ultrafine grain sizes, down to nanometer dimensions [4, 15].

During a detailed investigation on the effects of mechanical alloying on the amorphization behavior of non-ferrous Cu-Hf alloys, we noted the formation of a metastable face-centered cubic (FCC) phase with a lattice parameter of 0.4566 nm. Occurrence of such an FCC phase in the Cu-Hf system could not be explained on the basis of formation of a supersaturated solid solution of Hf in Cu achieved by mechanical alloying methods. It was also not possible to explain this observation on the basis of a metastable intermetallic phase with the composition of either Cu_2Hf or Hf_2Cu having the CaF_2-type crystal structure. Since it is possible that the equilibrium hexagonal close-packed (HCP) form of Hf could undergo an allotropic transformation to the FCC form under the non-equilibrium conditions of mechanical alloying, it was decided to investigate whether this is a possibility in the pure metal Hf. Since the group IV B metals, Ti, Zr and Hf behave in a similar way, the investigation was extended to Ti and Zr metals.

1.6. Chapters Outlook

While chapter 1 is the introduction, chapter 2 is on experimental procedure. Chapter 2 talks about the experimental steps followed in the present investigation which include characterization using XRD, SEM, TEM, 3DAP and also sample preparation for TEM and 3DAP using FIB technique.

Chapter 3 describes the grain size measurements of the four SS304+Al coatings. It considers the effects of Al addition and variation in normalized deposition temperature on the grain size and grain structure.

Chapter 4 studies the role of Al in influencing phase transformation. It identifies the different phases in the four coatings using XRD, TEM and equilibrium diagrams. Chapter 5 discusses the formation of two metastable phases, ferrite and sigma in SS304+0Al coating. Chapter 6 specially focuses on SS304+10Al microstructure dealing with the findings of intermetallic B2 phase and a layered structure at nano scale.

Chapter 7 studies formation of a metastable phase in the metal Hf while Chapter 8 extends the study to the other group IV B metals Ti and Zr including milling under ultra high purity environment. It helps in identifying the nature of phase transformations in mechanically milled Ti, Zr and Hf powders

1.7. References

1. C. Suryanarayana, ed., Non-equilibrium Processing of Materials, (series ed. R.W. Cahn) Vol. 2 (1999), Pergamon Press, Oxford.
2. T.S. Srivatsan and T.S. Sudarshan, eds., Rapid Solidification Technology: An Engineering Guide, (1993), Technomic Publishing Company, Inc., Lancaster, Pennsylvania.

3. D.M. Mattox, Handbook of Physical Vapor Deposition (PVD) Processing (1998), Noyes Publications, Park Ridge, New Jersey.
4. C. Suryanarayana, Mechanical Alloying and Milling (2004), Marcel Dekker, New York.
5. G.E. Dieter, ed., ASM Metals Handbook Volume 20: Materials Selection and Design. Vol. 20 (1997), ASM International, Materials Park, Ohio. *p*.1146.
6. P.H. Mayrhofer, C. Mitterer, L. Hultman, and H. Clemens, Microstructural design of hard coatings, Progress in Materials Science, 51 (2006), p.1032
7. R. Wei, J.J. Vajo, J.N. Matossian, and M.N. Gardos, Aspects of plasma-enhanced magnetron-sputtered deposition of hard coatings on cutting tools, Surface and Coatings Technology, 158-159 (2002), p.465
8. F. Wang, Oxidation resistance of sputtered Ni3(AlCr) nanocrystalline coating, Oxidation of Metals, 47 (1997), p.247
9. G. Cao, L. Geng, Z. Zheng, and M. Naka, The oxidation of nanocrystalline Ni3Al fabricated by mechanical alloying and spark plasma sintering, Intermetallics, 15 (2007), p.1672
10. G. Chen and H. Lou, Effect of Nanocrystallization on the oxidation behavior of a Ni–8Cr–3.5Al alloy, Oxidation of Metals, 54 (2000), p.155
11. Z. Liu, W. Gao, K.L. Dahm, and F. Wang, Oxidation behaviour of sputter-deposited Ni-Cr-Al micro-crystalline coatings, Acta Materialia, 46 (1998), p.1691
12. W. Gao, Z. Liu, and Z. Li, Nano-and microcrystal coatings and their high-temperature applications, Advanced Materials, 13 (2001), p.1001
13. Z. Liu, W. Gao, and Y. He, Oxidation behaviour of nanocrystalline Fe-Ni-Cr-Al alloy coatings, Materials Science and Technology, 15 (1999), p.1447
14. N.S. Cheruvu, *Nanostructured Coatings by Pulsed Plasma Processing for Alloys Used in Coal-Fired Environments*. 2008 (Report), Southwest Research Institute: San Antonio, Texas.
15. C. Suryanarayana, Mechanical alloying and milling, Progress in Materials Science, 46 (2001), p.1

CHAPTER 2: EXPERIMENTAL PROCEDURE

Four coatings of SS304+Al with different Al contents of 0, 4, 7 and 10 wt.% were received in the as-deposited condition. Approximate dimensions of the received coupons were 10 mm x 10 mm x 3 mm. The coatings were prepared by Plasma enhanced magnetron sputter-deposition (PEMS) at the Southwest Research Institute (SwRI), San Antonio, Texas.

The compositions of the 304-type austenitic stainless steel (SS304) target and substrate used for sputter-deposition are shown in Table 2.1. 304 steel coatings with different Al contents were deposited on top of the base material (substrate) SS304.

Table 2.1: Compositions (in wt.%) of the target and substrate used in the investigation

Element	Fe	Cr	Ni	Si	Mn	Mo	C	S	P	N
Target	Balance	18.52	8.13	0.41	1.36	0.33	0.010	0.16	0.026	-
Substrate	Balance	18.25	8.09	0.36	1.245	0.35	0.023	0.0016	0.029	0.32

The as-deposited coatings were characterized by x-ray diffraction (XRD), scanning electron microscopy (SEM), transmission electron microscopy (TEM) and three-dimensional atom probe (3DAP) techniques.

(i) XRD was used for phase identification, lattice parameter(s) and strain

(ii) SEM was used for surface morphology and chemical analysis

(iii) TEM was used for phase identification, microstructural analysis, and localized chemical analysis

(iv) 3DAP was used for nanostructure analysis at extremely small length scales

The sequence of experimental procedure is shown in Figure 2.1.

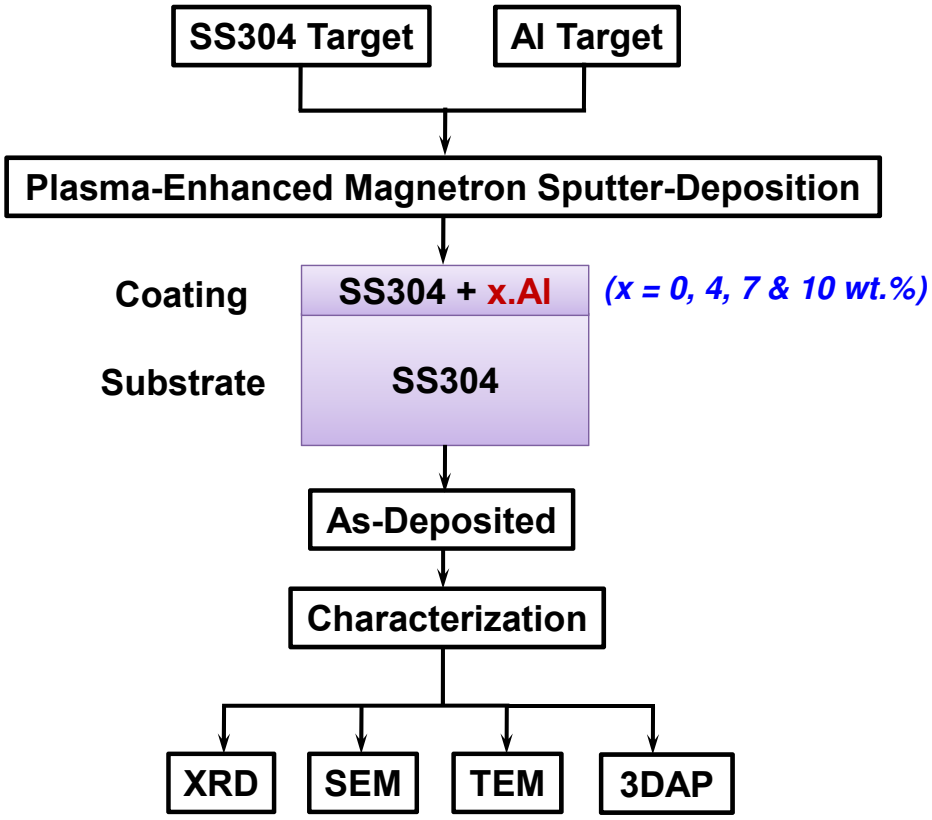

Figure 2.1: Line diagram of experimental procedure for the sputter-deposited coatings

When it comes to the microstructure of the coatings, two terms are commonly used in the context of the view of observation. One of them is viewing the sample from top, known as plan view or in-plane view. The second view is the front view or cross-section view. The cross-section view was mostly used in the present microstructural study. Figure 2.2 shows schematically the two types of views.

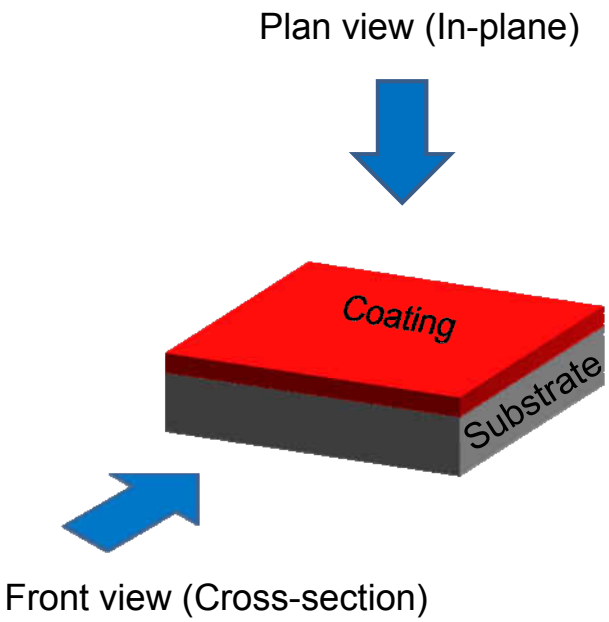

Figure 2.2: Two types of coating observation views (i) plan view or top view (ii) cross-section or front view

2.1. Coating: Plasma Enhanced Magnetron Sputter-deposition

Magnetron sputtering is a physical vapor deposition (PVD) technique in which the target atoms are sputtered by high energy ions of Ar (or other inert gaseous elements) and subsequently deposited on a substrate material. A magnetic field is applied over the sputtering target to confine the high-density plasma. The argon ions in the plasma are accelerated to the target. The collision of the ions with the cathode ejects particles of the target material. The substrate to be coated is positioned in front of the target, and the particles that strike the substrate condense to form an adherent coating.

Plasma enhanced magnetron sputter-deposition (PEMS) technique [1-2] was used to deposit the coatings. Enhanced plasma was used to increase the coating density. A schematic of the PEMS chamber is shown in Figure 2.3. A schematic of top view of the sputtering chamber is also shown in Figure 2.4. A few important things that need to be marked in the diagram are:

(i) There are two targets attached to the two magnetrons, one is SS304 and the second is Al.

(ii) There is a hot filament and a DC discharge power supply at the top of the chamber to produce plasma that can increase the coating density. This is independent of the plasma produced by the magnetrons. The hot filament is also capable of raising the temperature of the chamber since there is no cooling system in place.

(iii) There are two distinct rotation mechanisms called 2-fold or double rotation mechanisms; one of them is primary rotation of the central rod (rotates continuously at 6 revolutions per minute) and second is rotation of the hanging substrate-coupons around their own axis (rotates intermittently 5 times in each primary rotation, making the total revolutions to 6 x 5 = 30 rpm). This overall rotation mechanism is somewhat similar to planetary motion except in the point that the secondary rotation is not continuous.

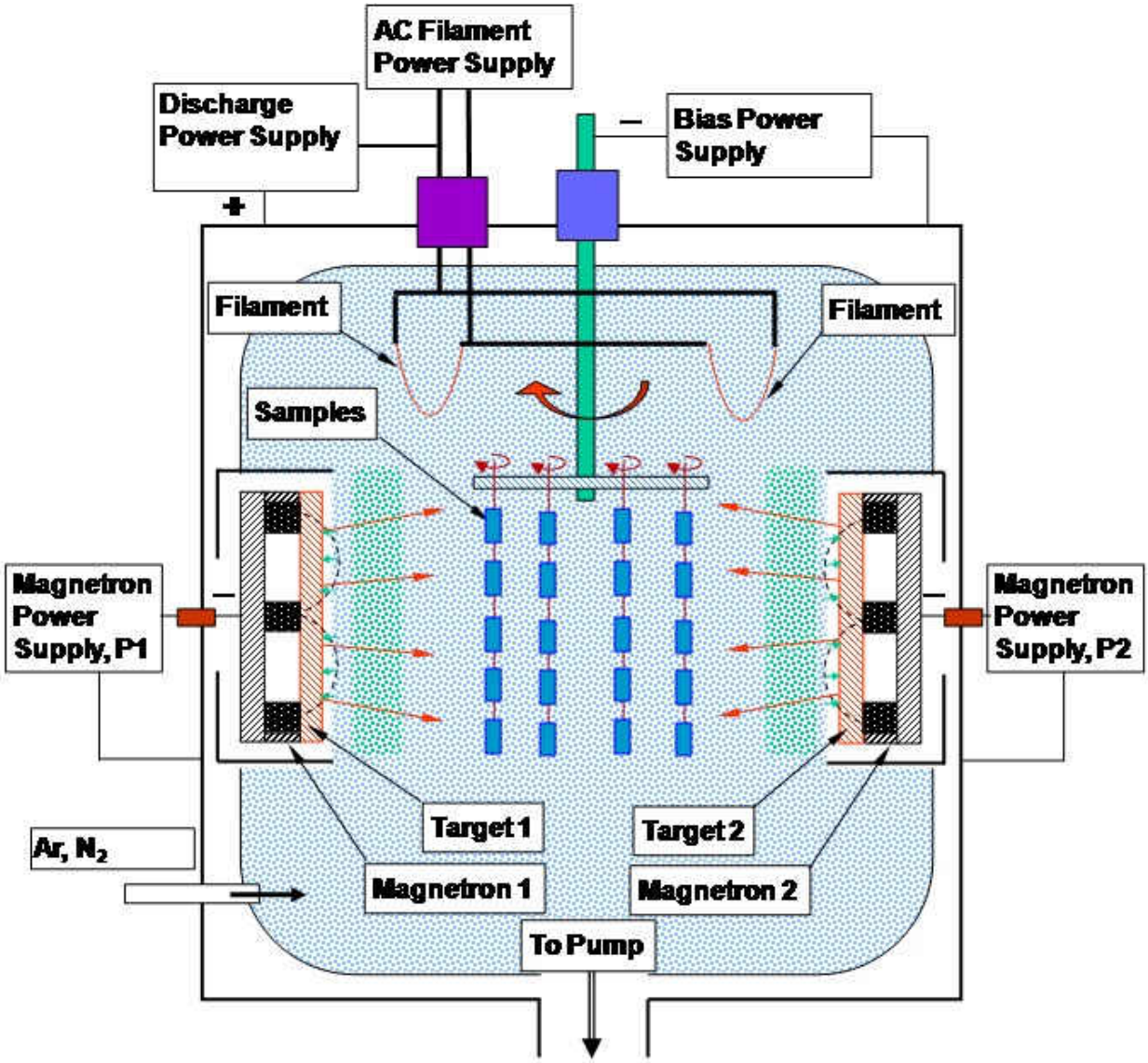

Figure 2.3: Schematic diagram of plasma enhanced magnetron sputter deposition system at Southwest Research Institute (Courtesy of SwRI)

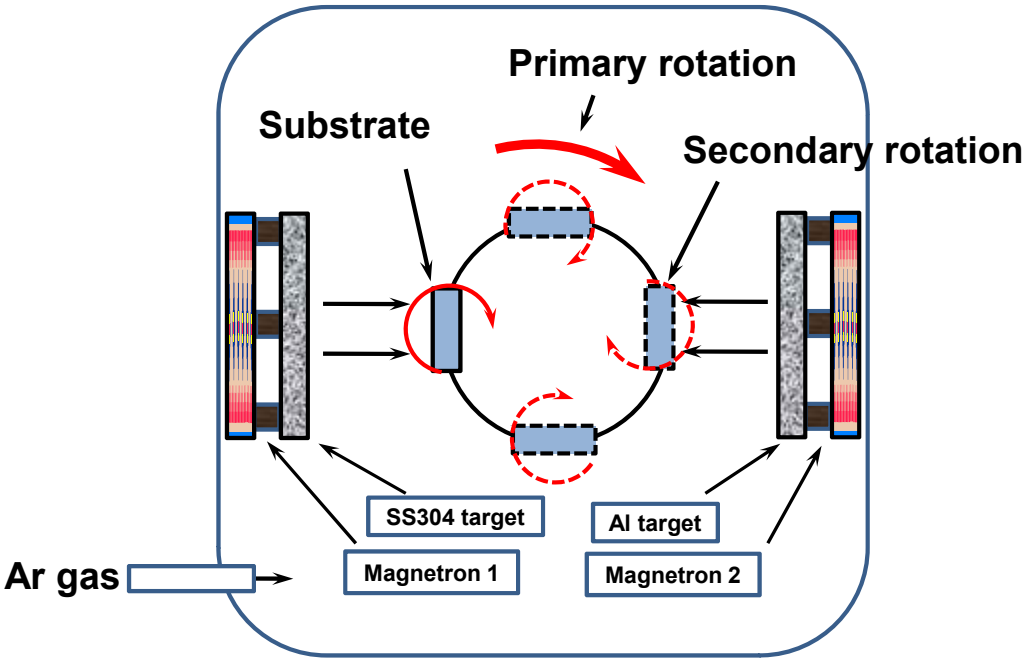

Figure 2.4: Magnetron sputtering chamber. Two targets, SS304 and pure Al, are facing each other

The sputter-deposition experimental conditions (variables) can be categorized into two groups. The first group contains the conditions that are independent of Al content and the second group consists of the conditions that are a function of Al content. Table 2.1 lists the conditions of the former case while Table 2.2 lists that of the latter case. Most notable experimental conditions are the rotation of SS304 substrate, power on Al target and Ar ion energy. One notable omission in the conditions is the substrate/deposition temperature. It was not measured.

Table 2.2: Fixed experimental parameters; these are not dependant on Al content

Parameter	Magnitude
Distance between target and substrate	85 mm
Power on SS304 target	4 kW
Primary substrate rotation	6 rpm
Secondary substrate rotation	30 rpm
Argon ion energy	40 eV
Bias voltage on substrate	40 V

Table 2.3: Experimental conditions used and the resultant coating thickness and deposition rates achieved as a function of Al content

Al Content (Wt.%)	Power on Al target (kW)	Ar gas pressure (milliTorr)	Deposition time (hours)	Coating thickness (µm)	Deposition rate (nm/s)
0	No target	2.51	4	27	1.9
4	0.4	2.79	5	28	1.6
7	0.7	2.78	5	28	1.6
10	1.1	2.55	4	32	2.2

Note 1: Bias voltage on magnetron targets is 300-500 volts depending on the power requirements

Note 2: Deposition temperature was not measured because of the substrate rotation

2.2. X-ray Diffraction (XRD)

XRD is a relatively simple, inexpensive yet powerful technique for phase identification. Hence, this technique was used as a preliminary step before doing any other characterization experiments. XRD characterization of the four as-deposited coatings was performed and useful information on crystal structure, lattice parameters, and consequently phase identification was obtained using the Bragg-Brentano method.

XRD of the coated samples was carried out using Rigaku X-ray Diffractometer. Cu K_α radiation ($\lambda = 0.15406$ nm) was used to record diffraction patterns between 2θ of 20 to 100° at 40 kV voltage and 30 mA current. The resultant *d*-spacings and lattice parameters were calculated and the phases were identified. The strain in the coatings was evaluated by Williamson-Hall approach [3-4].

2.3. Scanning Electron Microscopy (SEM)

A morphological study of the as-deposited SS304+Al coatings was performed using Hitachi SEM S3500. An acceleration voltage of 20 kV was mostly used for both imaging and compositional analysis using energy dispersive spectroscopy (EDS). The coatings were studied both in plan view and cross-section view. In analyzing the composition, several of the point EDS, line EDS, and area EDS scans were recorded.

2.4. Sample Preparation for TEM

Focused Ion Beam (FIB) and Ion Milling (IM) techniques were used to prepare thin samples for TEM study. The FIB technique is particularly suitable for preparing samples from coatings without destroying them and selecting preferred sites.

The samples of SS304 coating were prepared using FIB FEI 200, using In-situ FIB and Ex-situ FIB techniques [5]. The sample dimensions of the In-situ FIB were about 20 μm length and 12 μm width, while that of Ex-situ were 12 μm length and 5 μm width. In FIB, a variable current, starting from 7 nA to ending with 30 pA, at a voltage of 30 kV was used during the preparation of the thin foil specimen. Platinum metal was sputter-deposited on top of the thin sample area in order to protect it from damage by high energy Ga ion beam. Figure 2.5 shows the steps in ex-situ FIB sample preparation.

Ion milling was carried out using precision ion polishing system (PIPS). Mechanically thinned steel coatings were further thinned down to electron transparent level using Ar ions targeted on sample surface.

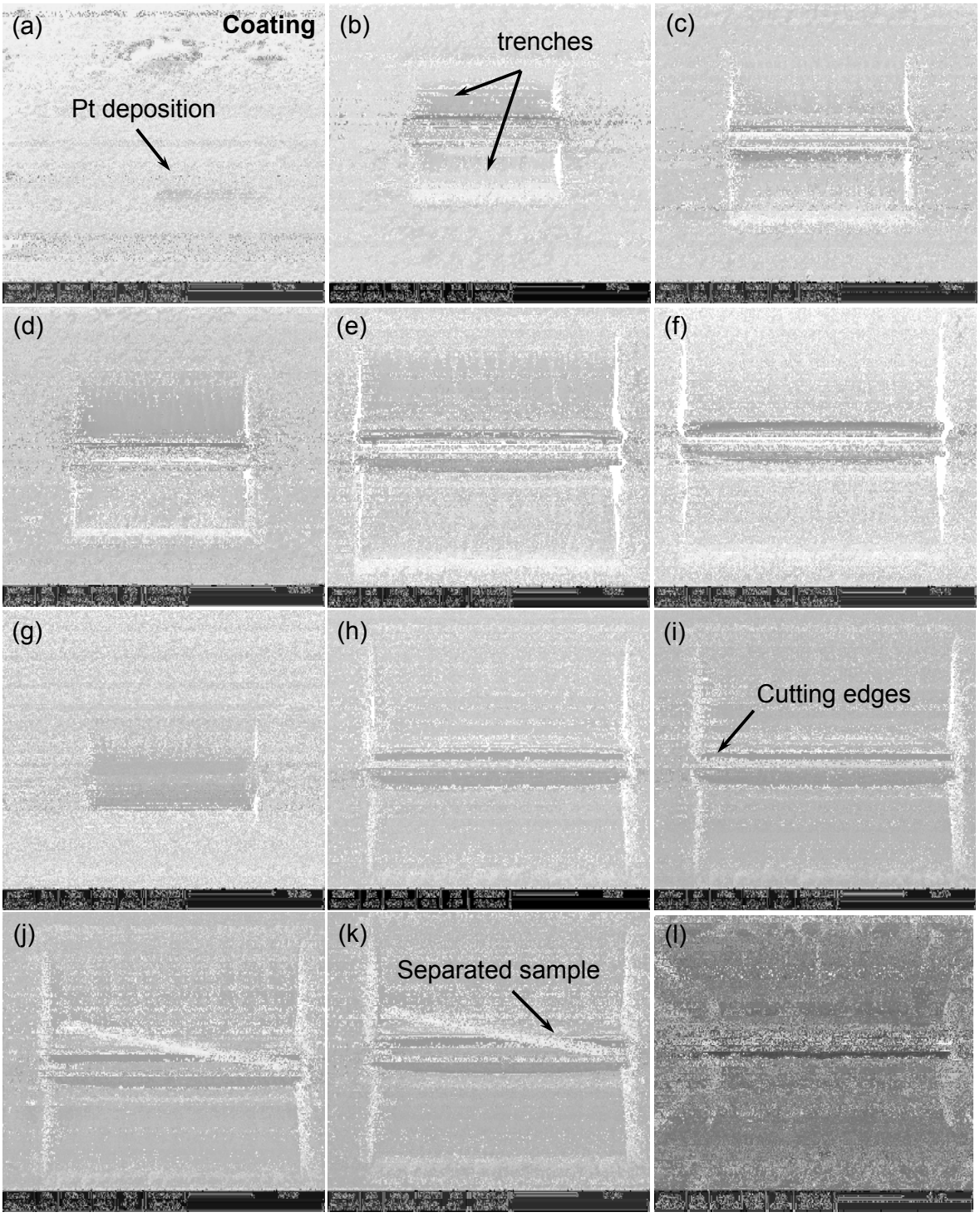

Figure 2.5: Series of FIB micrographs of ex-situ method showing the preparation of thin foil sample for TEM study. The sample is taken out using a polymeric needle under an optical microscope and placed on a carbon coated Cu grid.

2.5. Transmission Electron Microscopy

TEM was carried out on the FIB prepared samples using Philips FEI Tecnai F30, operated at 300 kV.

The following techniques of TEM were used to characterize the microstructural features, crystal structure, and chemical composition. Phases were identified with the electron diffraction while the grain size was measured in the bright field (BF) and dark field (DF) micrographs using Digital Micrograph software.

(i) Bright field, dark field, and selected area diffraction patterns (SADP)

(ii) Energy dispersive spectroscopy (EDS) for chemical analysis

(iii) Scanning transmission electron microscopy (STEM) for microstructural analysis in scanning mode, usually combined with EDS

(iv) Energy filtered transmission electron microscopy (EFTEM) for elemental distribution

(v) High resolution transmission electron microscopy (HRTEM) for studies at very high magnification and resolution

(vi) Nano beam diffraction (NBD) for identification of any minor variations in d-spacings

2.6. Sample Preparation for 3DAP

Needle samples with a tip radius of about 50-100 nm are required for the atom probe study. The most common techniques to prepare needle/wire samples are electropolishing and focused ion beam (FIB). Both methods were used but only FIB method succeeded in giving a good number of atom count (> 2 million) in the atom probe. The needle preparation is somewhat similar to In-situ FIB sample preparation for TEM described earlier. Ga contamination is an important issue while preparing the needle sample. Though it cannot be avoided completely, Ga

contamination can be minimized by FIB expertise. Use of a very low-energy ion beam is essential in the final stages of sample preparation. Figure 2.6 shows different steps in 3DAP needle sample preparation.

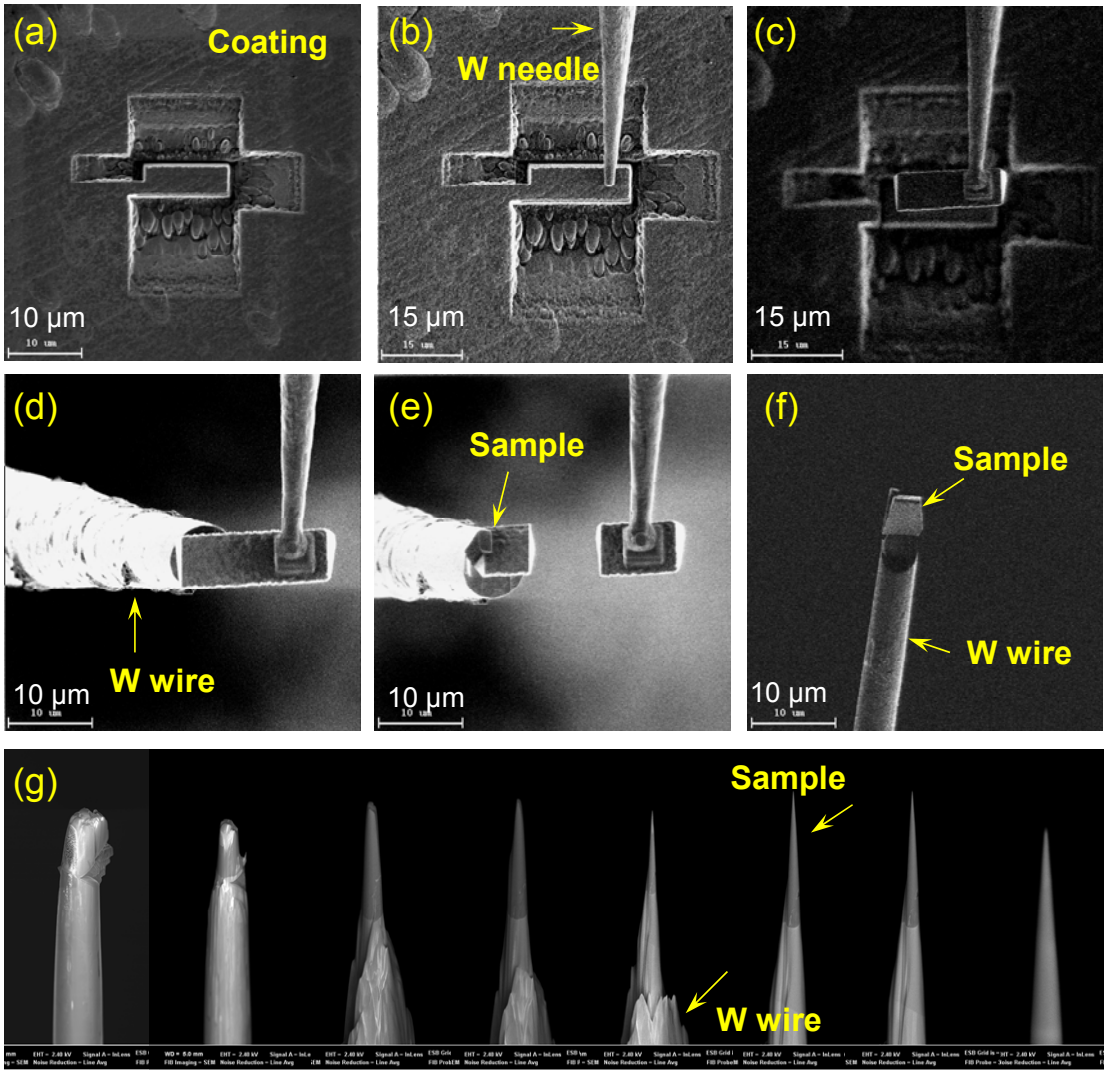

Figure 2.6: Steps in 3DAP sample preparation (a) milling of trenches on four sides of the coating leaving a small portion at the left end for holding, (b) bringing in tungsten needle for attaching, (c) lifting the sample with needle after cutting the bottom, (d) attaching the sample to a W wire, (e) welding the sample to W wire and cutting the remaining piece, (f) welded sample and W wire, and (g) series of thinning steps.

About 50-100 nm tip radius needles for 3DAP analysis were prepared using Hitachi FIB. The surface of the needle was cleaned by a low energy ion beam of 5 kV and 20 pA in Carl Zeiss CrossBeam FIB. Detailed preparation of needles for 3DAP was reported earlier [6].

2.7. Three-Dimensional Atom Probe (3DAP)

The needle sample is prepared by FIB and is immediately transferred to a vacuum chamber that is attached to the 3DAP microscope. Eventually, the sample is taken to the main 3DAP chamber where the actual acquisition of ions from the sample is done (Figure 2.7). The low temperature (-80° C) main chamber has suitable sized slots as sample holders. A very high voltage (2-16 kV) is applied on the 50 to 100 nm tip of the sample and high electrostatic field is created. Hence, field ionization begins on the tip of the needle and eventually the ions hit detector screen. From each ionic collision, the position of ion and its mass/charge ratio are obtained. After millions of such collisions, it is possible to identify the elements present in the sample by identifying the peaks in the plot of, number of collisions vs mass/charge ratio. Based on the peak fitting in the plot, the position of each atom (ion) can be back calculated and finally a 3 dimensional reconstruction can be obtained for each/all elements using the software called POSAP (Position assisted atomic probing). Figure 2.8 shows the principle of atom probe field ion microscopy.

Figure 2.7: 3DAP field ion microscope (Courtesy of NIMS, Tsukuba, Japan)

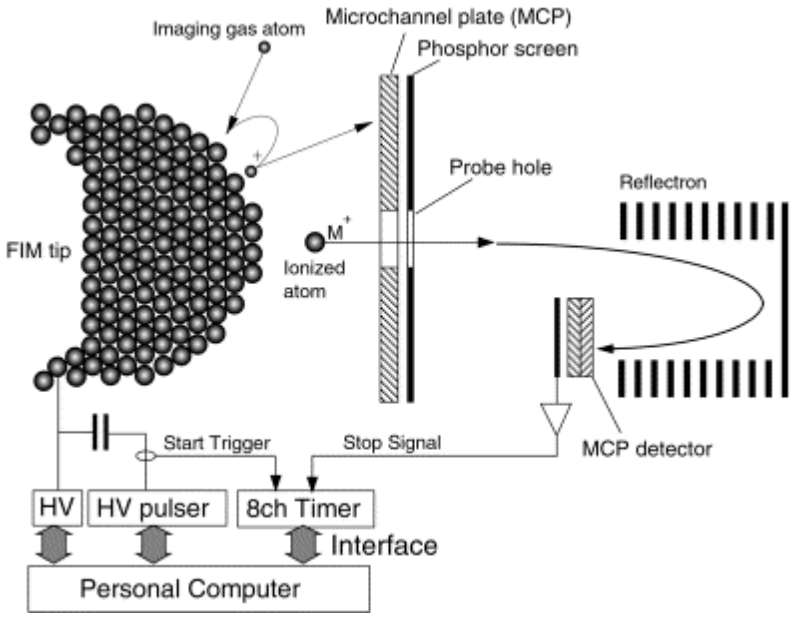

Figure 2.8: Schematic illustration for the principle of a field ion microscope and a conventional atom probe [7].

2.8. Mechanical Milling

Mechanical milling (MM) is a milling process that involves repeated cold welding, fracturing, and rewelding of powder particles in a high-energy ball mill. MM results in structural and microstructural modifications including formation of metastable phases, phase transformations, and synthesis of materials with ultrafine grain sizes, down to nanometer dimension [8-9].

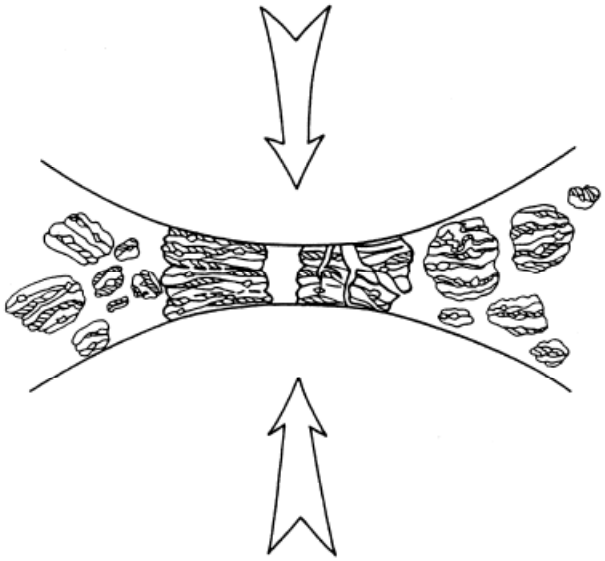

Figure 2.9: Mechanism of mechanical milling (Ball-powder collision of powder mixture) [8]

Elemental powders of Hf, Ti, and Zr (with > 99 wt.% purity) were milled in a high energy SPEX 8000D Mixer mill under two different conditions. One was the regular milling in which the loading and unloading of the powders was done inside a glove box filled with argon gas. The sealed container was then placed inside the mill, and milling was performed with air ambient surrounding the mill. A small amount of stearic acid was used as a process control

agent to prevent excessive cold welding of the powder and attaching itself to the walls of the milling container and the grinding media. The second was when the loading and unloading of the powders and also the milling were done inside an ultra-high purity (UHP) environment. This was achieved by handling of the powders, including milling, inside a glove box under an argon atmosphere. That is, the SPEX mill itself was placed inside the glove box. The argon atmosphere inside the glove box was continuously purified to keep the oxygen and water vapor level each below 1 ppm [10]. Thus, there is no chance for any gaseous contaminant to react with the milled powder despite the high reactivity of Hf, Ti,and Zr. No process control agent was used in this case. The milling media used were stainless steel containers and hardened stainless steel balls with a ball-to-powder weight ratio of 10:1 in both the type of experiments. X-ray diffraction (XRD) was conducted to evaluate the structural changes in the milled powder as a function of milling time. The diffraction patterns were recorded using Cu Kα radiation in the 2θ range of 10 to 90^{o} at a speed of 1.2^{o}/min, and were analyzed using standard procedures [4]. Standard wet chemical analysis was conducted to estimate the gaseous impurity levels in the powders after milling.

In the coming chapters beginning with chapter 3, microstructural and crystallographic characterization of the sputter deposited coatings SS304+Al coatings and mechanically milled Hf, Ti and Zr powders will be presented.

2.9. References

1. R. Wei, J.J. Vajo, J.N. Matossian, and M.N. Gardos, Aspects of plasma-enhanced magnetron-sputtered deposition of hard coatings on cutting tools, Surface and Coatings Technology, 158-159 (2002), p.465
2. P.H. Mayrhofer, C. Mitterer, L. Hultman, and H. Clemens, Microstructural design of hard coatings, Progress in Materials Science, 51 (2006), p.1032
3. B.D. Cullity and S.R. Stock, Elements of X-ray Diffraction (2001), 3rd. edition., Addison-Wesley Publishing Company, Massachusetts, USA.
4. C. Suryanarayana and M.G. Norton, X-Ray Diffraction: A Practical Approach (1998), Plenum Press, New York.
5. J. Li, T. Malis, and S. Dionne, Recent advances in FIB-TEM specimen preparation techniques, Materials Characterization, 57 (2006), p.64
6. D.J. Larson, D.T. Foord, A.K. Petford-Long, T.C. Anthony, I.M. Rozdilsky, A. Cerezo, and G.D.W. Smith, Focused ion-beam milling for field-ion specimen preparation: preliminary investigations, Ultramicroscopy, 75 (1998), p.147
7. K. Hono, Nanoscale microstructural analysis of metallic materials by atom probe field ion microscopy, Progress in Materials Science, 47 (2002), p.621
8. C. Suryanarayana, Mechanical alloying and milling, Progress in Materials Science, 46 (2001), p.1
9. C. Suryanarayana, Mechanical Alloying and Milling (2004), Marcel Dekker, New York.
10. T. Klassen, M. Oehring, and R. Bormann, Microscopic mechanisms of metastable phase formation during ball milling of intermetallic TiAl phases, Acta Materialia, 45 (1997), p.3935

CHAPTER 3: GRAIN SIZE OF SS304+Al COATINGS

3.1. Introduction

The present work has been undertaken to study how sputter deposition influences the grain size of SS304+Al coatings. Grain size measured only from TEM analysis is taken into consideration for the present study. Four coating mixtures of SS304 with different nominal compositions of Al- 0, 4, 7, and 10 wt.% were deposited on a SS304 substrate. These coatings were characterized for their grain sizes.

3.2. Results

In the present work, columnar type grains were observed in the cross-sectional TEM samples of all the coatings. The columnar grain width has been taken as a convenient measure. The present study considers columnar grain width as grain size. In other words, if we assume each columnar grain as a cylinder, the grain size is represented by the diameter of the cylinder. Figure 3.1 shows how the grain size was measured. The maximum columnar width of the grains was measured as the grain size. The size of each and every observed grain was measured in the coatings and was taken as a data point. All such data points were grouped for each coating composition and the grain size was plotted as a function of each measured grain number from the lowest to highest size. Standard deviation was calculated from the data points.

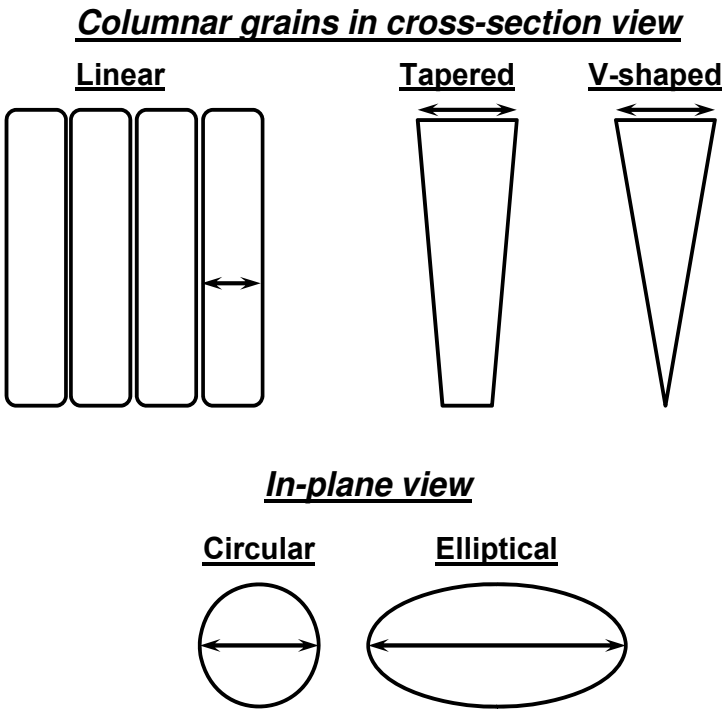

Figure 3.1: Method of measuring grain size

3.2.1. SS304+0Al Coating

Figure 3.2 shows a bright-field electron micrograph of the general microstructure of the as-deposited SS304 coating. The microstructure contains columnar grains perpendicular to the substrate, with their longitudinal direction parallel to the deposition direction. More than 100 grains were counted and the grain size is plotted from the smallest to the largest. The resultant distribution is shown in Figure 3.3. The grain size varied from 20 to 270 nm, with the average grain size of 95 nm and with a standard deviation of 50 nm. The corresponding histogram of the distribution of grain sizes is shown in Figure 3.4. It may be noted that about 60% of the grains are below 100 nm while the remaining 40% are in between 100 nm and 275 nm, i.e., in the submicron regime.

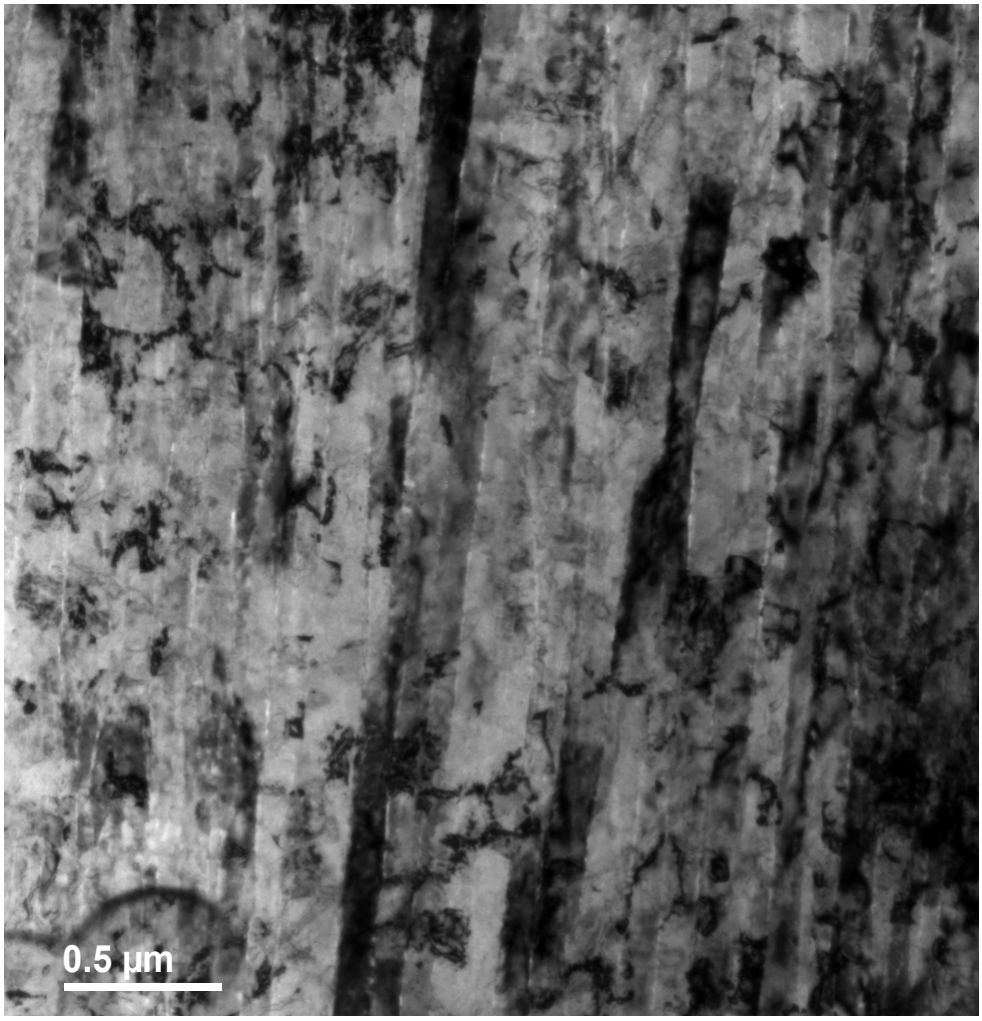

Figure 3.2: Typical BF electron micrograph showing the presence of columnar grains in the SS304+0Al coating. These columnar grains are oriented in a direction parallel to the direction of deposition.

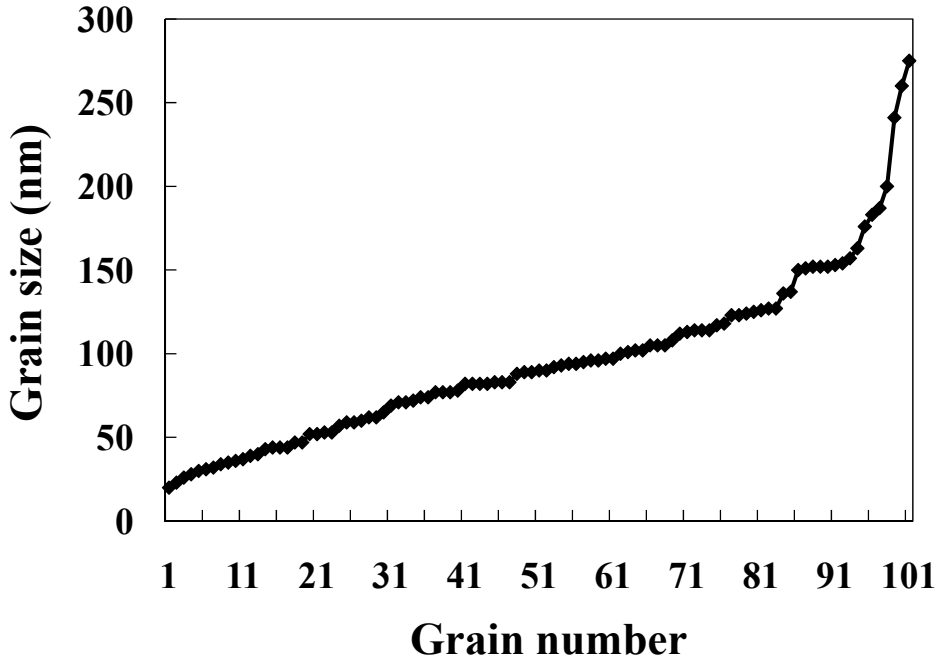

Figure 3.3: Variation of grain size in the SS304+0Al coating. The grain size varies from about 20 nm to 270 nm, and the average grain size is 95 nm.

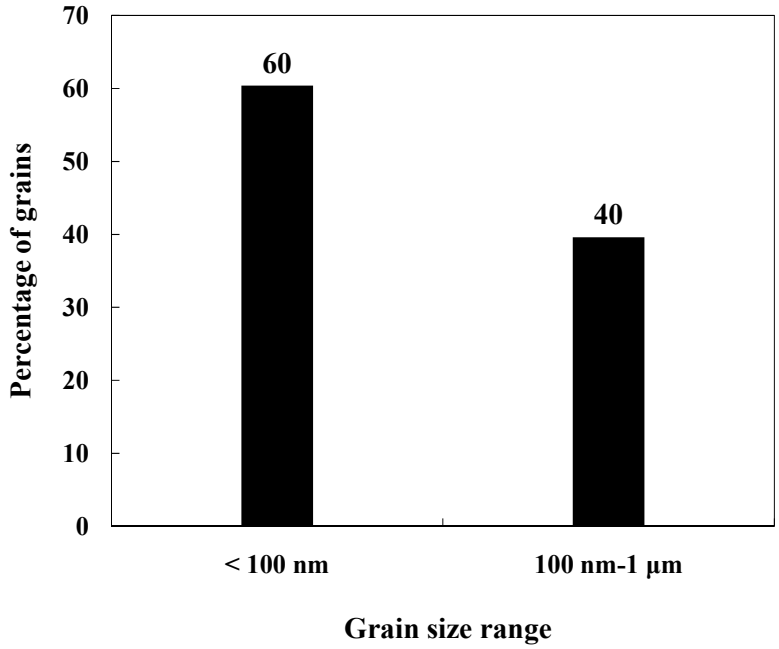

Figure 3.4: Histogram showing the grain size distribution in the SS304+0Al coating.

The 0Al coating appeared dense at lower magnifications with fully packed predominant nanocrystalline columnar grains. However, at higher magnifications and/or small out-of-focus conditions of electron beam in the BF mode, some porosity was observed. Figure 3.5 shows the nanopores which are distributed in the grain interiors or along the columnar grain boundaries.

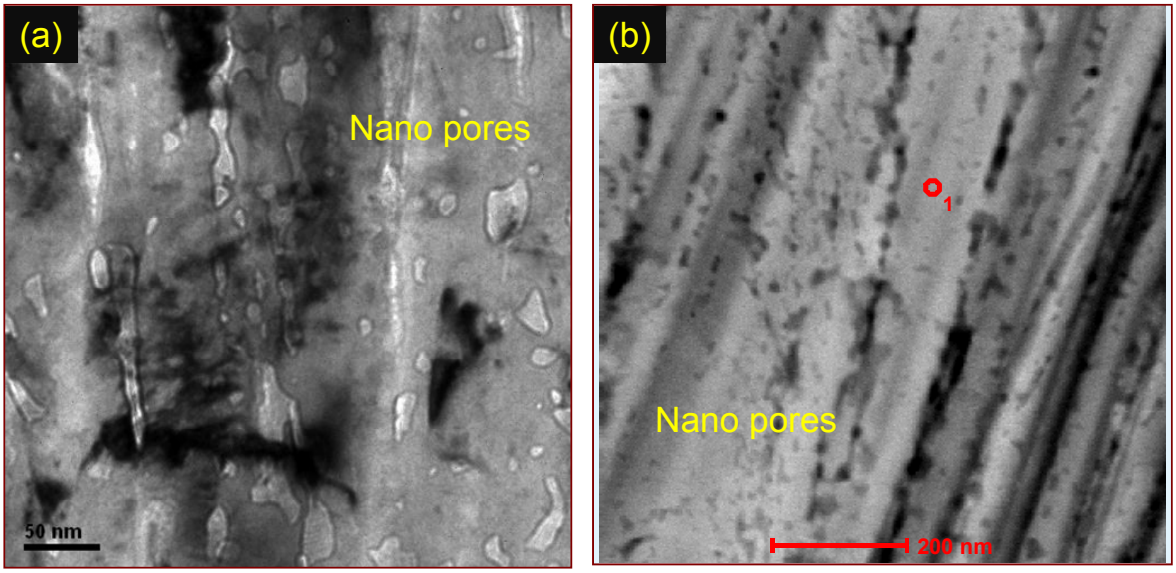

Figure 3.5: (a) BF TEM micrograph showing nano porosity in the grain interiors and along grain boundaries (b) STEM micrograph showing nano porosity. O_1 is an EDS spot.

3.2.2. SS304+4Al Coating

Typical bright-field electron micrographs from the SS304+4Al coating are shown in Figure 3.6 (a-c). The grain size in this coating varied from 30 nm to 1.2 μm. The average grain size was estimated to be 287 nm with a standard deviation of 280 nm. Figure 3.7 shows the variation of grain size in the sequence from the smallest grain to the largest grain in the observed area. It is seen from the histogram in Figure 3.8 that 33% of the grains are less than 100 nm and 63% of the grains are in between 100 nm and 1 μm. Unlike 0Al coating, this coating has no porosity.

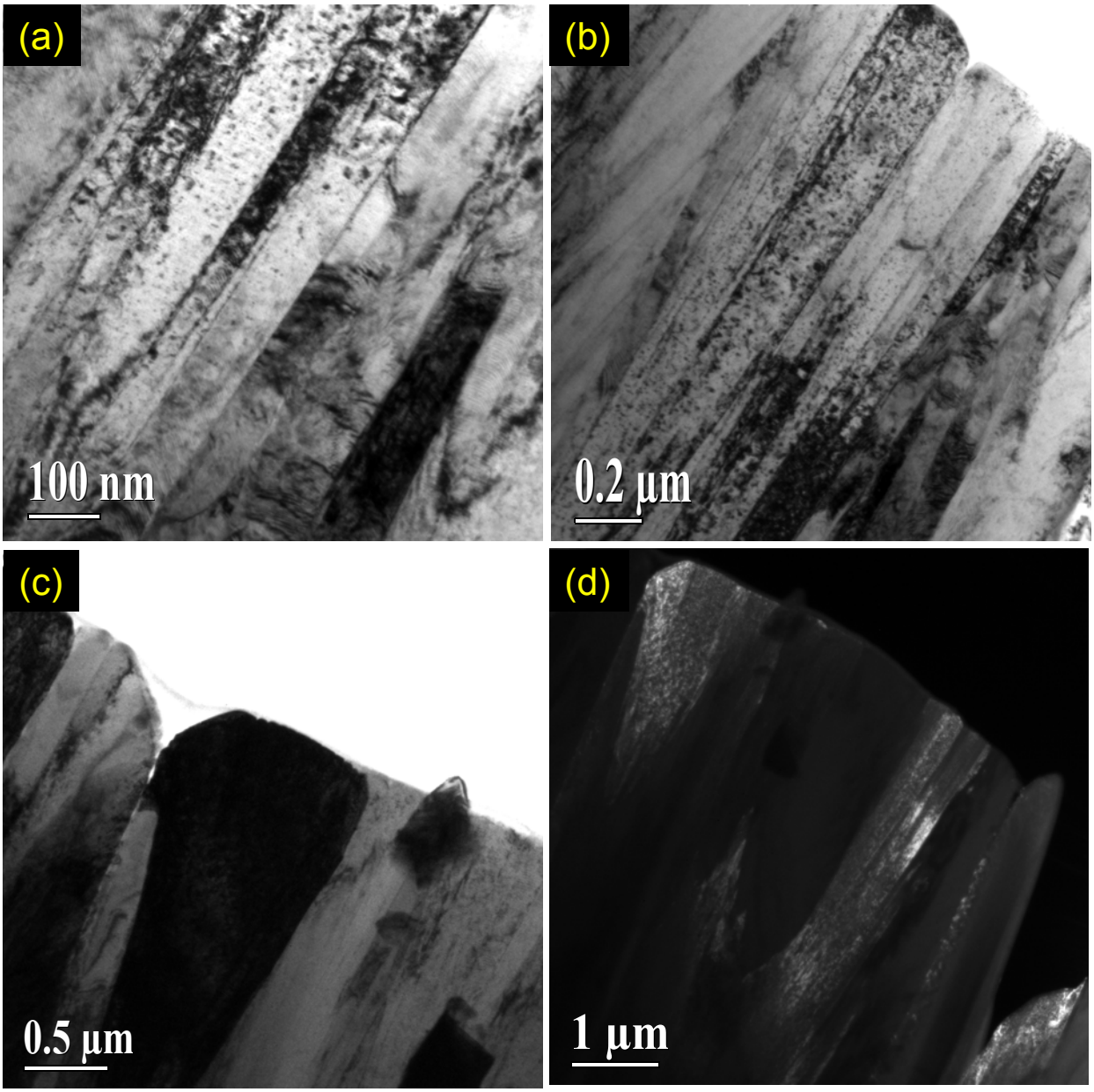

Figure 3.6: (a), (b) and (c) BF transmission electron micrographs from the SS304+4Al coating at different magnifications. (d) DF micrograph showing differently oriented grains

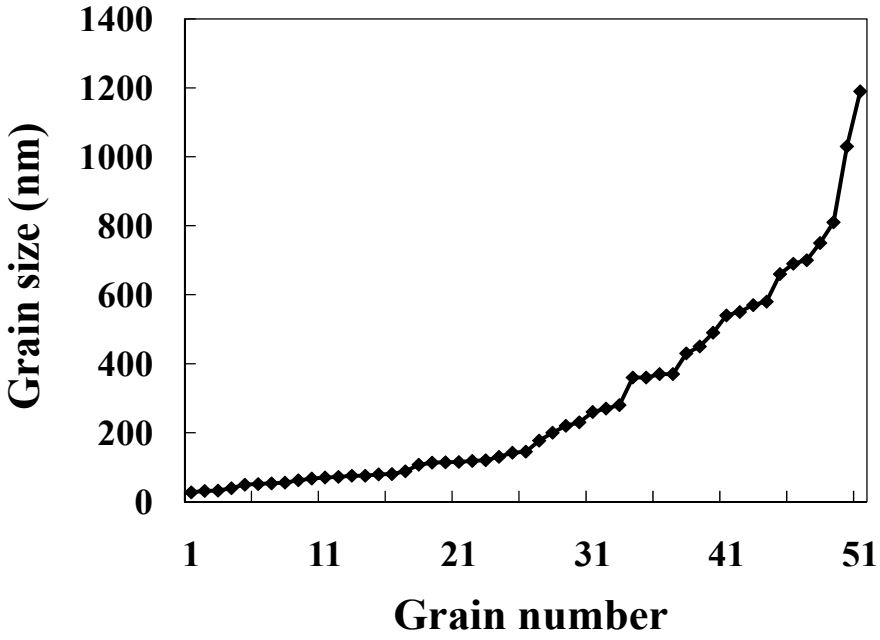

Figure 3.7: Variation of grain size in the SS304+4Al coating. The grain size varied in the range of 30-1200 nm, with an average value of 287 nm.

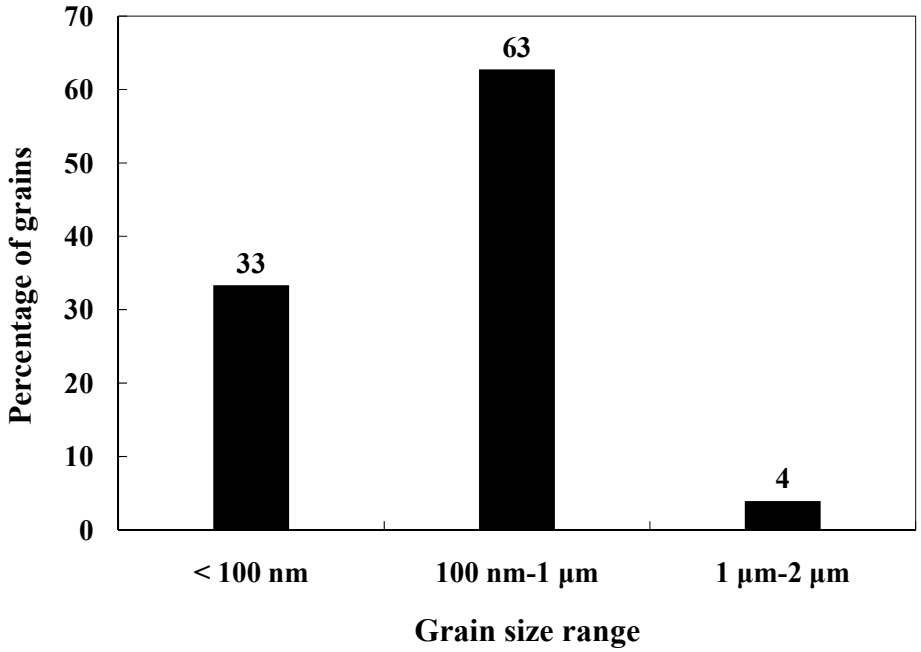

Figure 3.8: Histogram showing the grain size distribution in the SS304+4Al coating.

3.2.3. SS304+7Al Coating

The microstructure of the SS304+7Al coating is shown in Figure 3.9. The grain size for this coating was observed to vary from 20 nm to 1.6 μm. The grain size distribution is shown in Figure 3.10. The average grain size of 53 grains is 316 nm and the standard deviation is 330 nm. The columnar grains in this coating were often oriented randomly. The coating was dense with no porosity. Similar to the 4Al coating, about 34% grains are less than 100 nm and 65% of the grains are in between 100 nm and 1 μm (histogram in Figure 3.11).

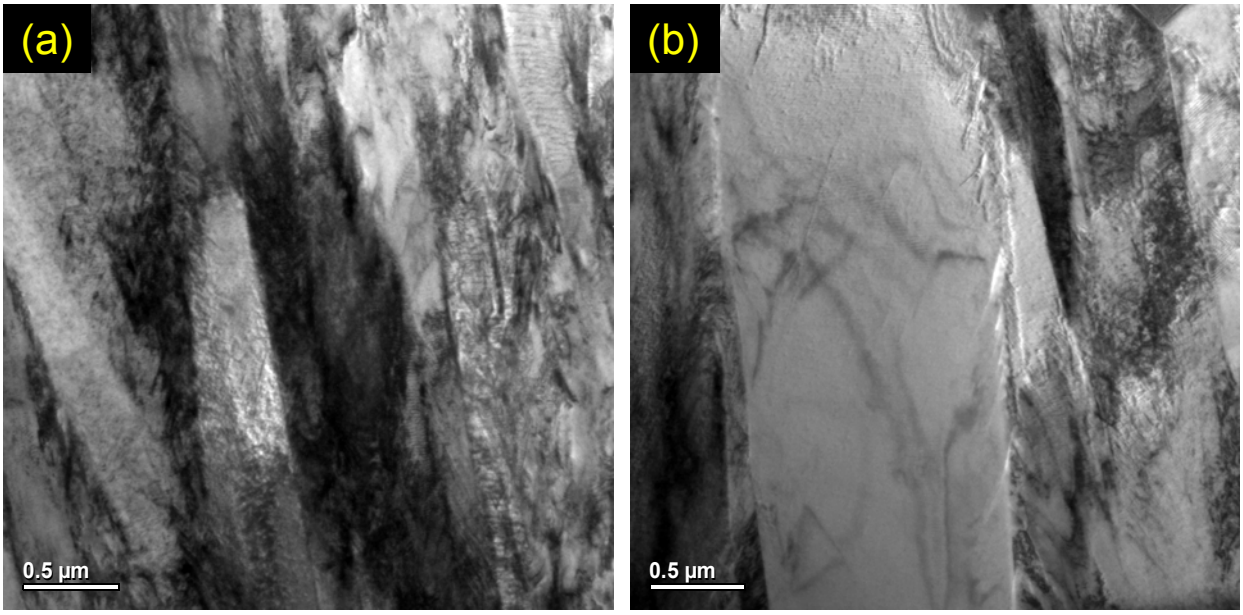

Figure 3.9: (a) and (b) Bright-field electron micrographs of the SS304+7Al coating. Dense columnar grains (without any porosity) were observed in this coating. A few grains are very large compared to others as seen from (b).

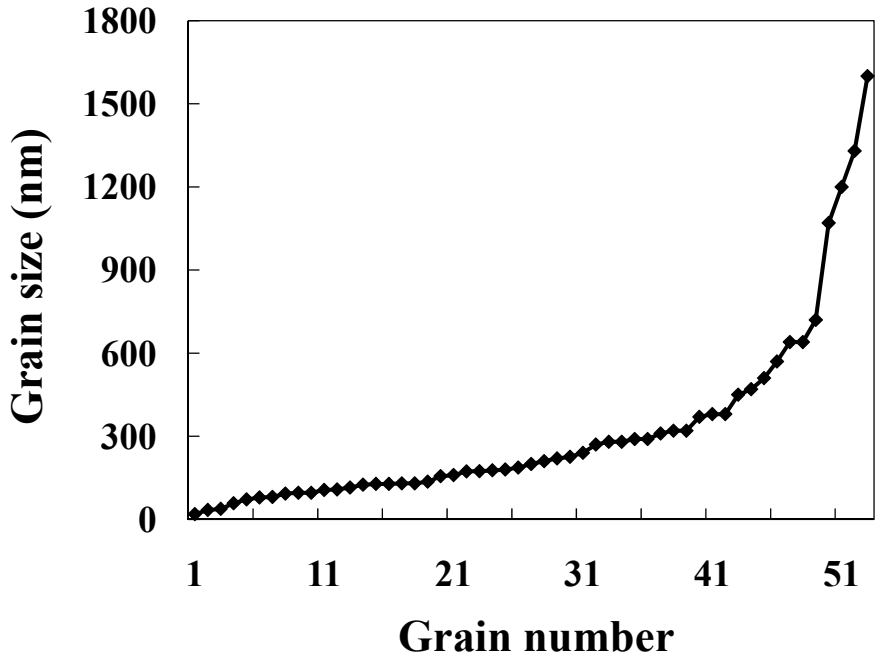

Figure 3.10: Variation of grain size in the SS304+7Al coating. The grain size varied from about 20 nm to 1.6 μm, and the average grain size is about 320 nm.

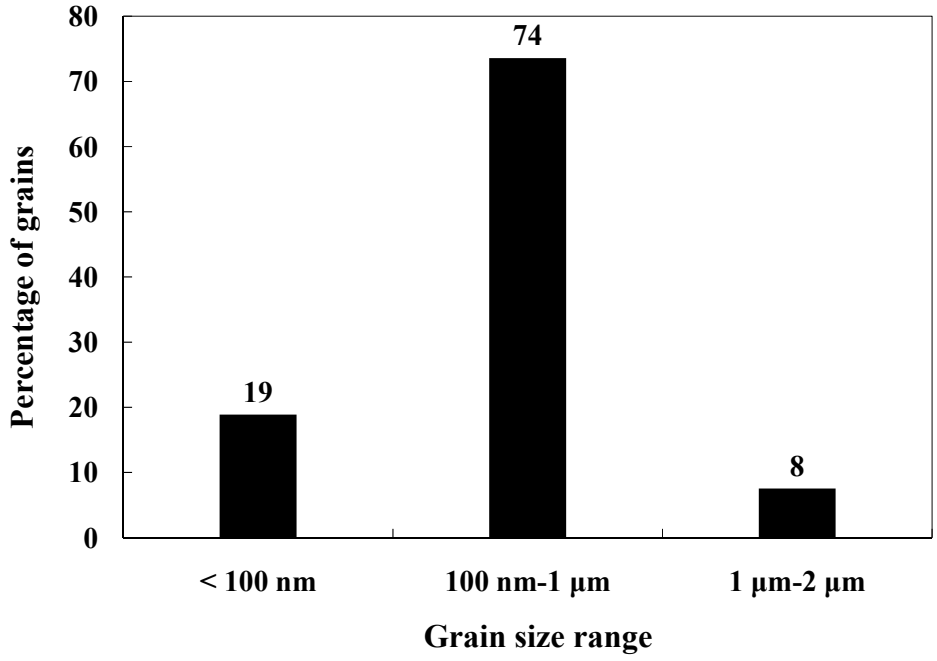

Figure 3.11: Histogram showing the grain size distribution in the SS304+7Al coating.

3.2.4. SS304+10Al Coating

Figure 3.12 shows a bright-field electron micrograph of the SS304+10Al coating. The microstructure of the cross section clearly shows uniformly distributed columnar grains which have grown in a direction perpendicular to the substrate, i.e., parallel to the direction of deposition. The average grain size of this sample was quite large and hence only a few grains (10 to 20) could be observed in each TEM sample. In order to study more grains, an in-plane sample was prepared. Figure 3.13 (a) and (b) are bright field TEM micrographs that show the distribution of grains in the in-plane sample at two different magnifications.

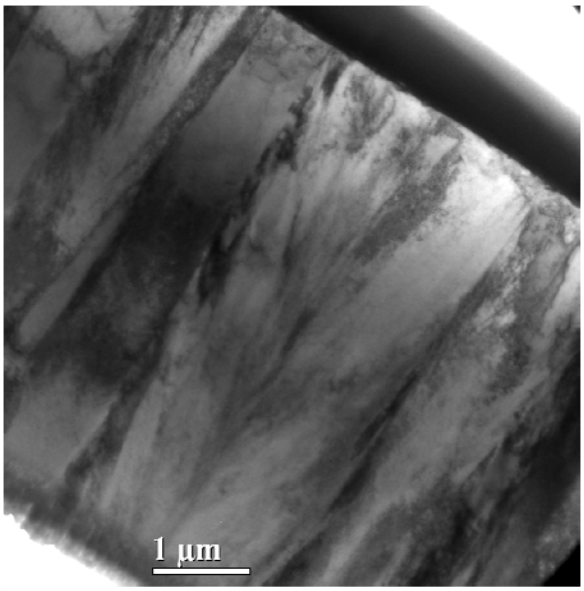

Figure 3.12: Microstructure of the SS304+10Al coating in the as-deposited condition.

The grain size was measured for more than 50 grains from four TEM samples. The grain size vs the grain number is plotted in Figure 3.14. The grain size was found to vary from as low as 130 nm to as high as 2.75 μm and the average grain size for this composition, from the columnar grains, was calculated to be 977 nm (Figure 3.14) and the standard deviation was 620 nm.

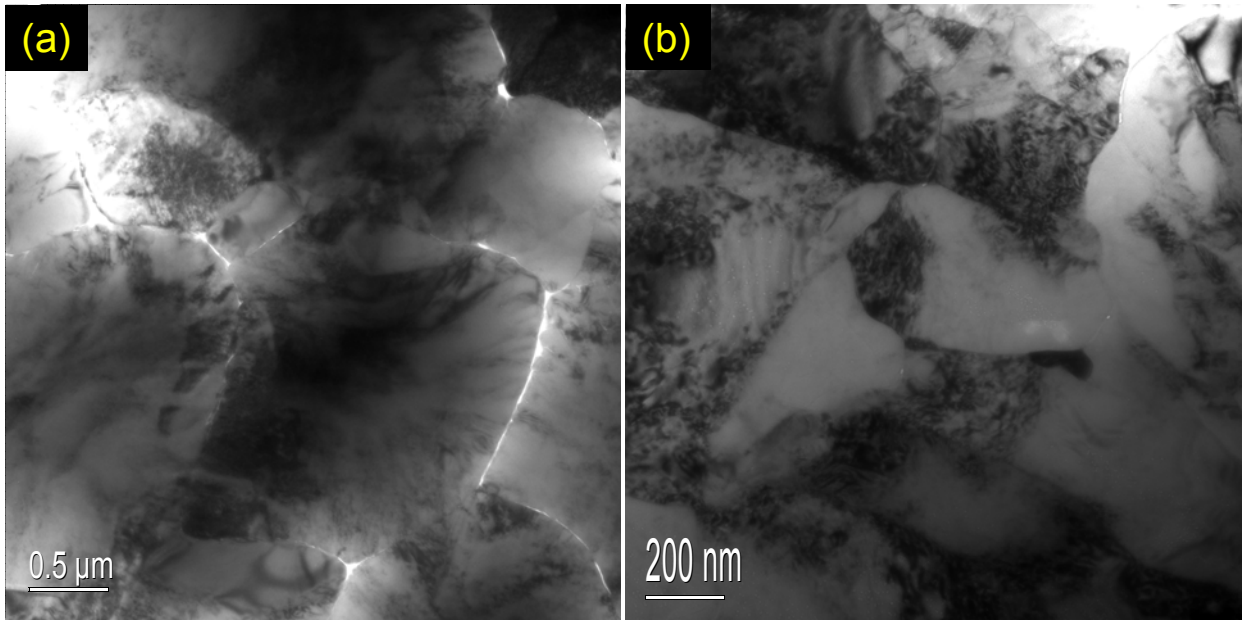

Figure 3.13: (a) BF TEM micrograph from in-plane sample of 10Al coating at a lower magnification showing grains. This ion-milled sample shows preferential removal at grain boundaries which appears porous. The grains typically look like equi-axed in the in-plane view. (b) BF micrograph at higher magnification revealing smaller grains that coexisting with larger grains.

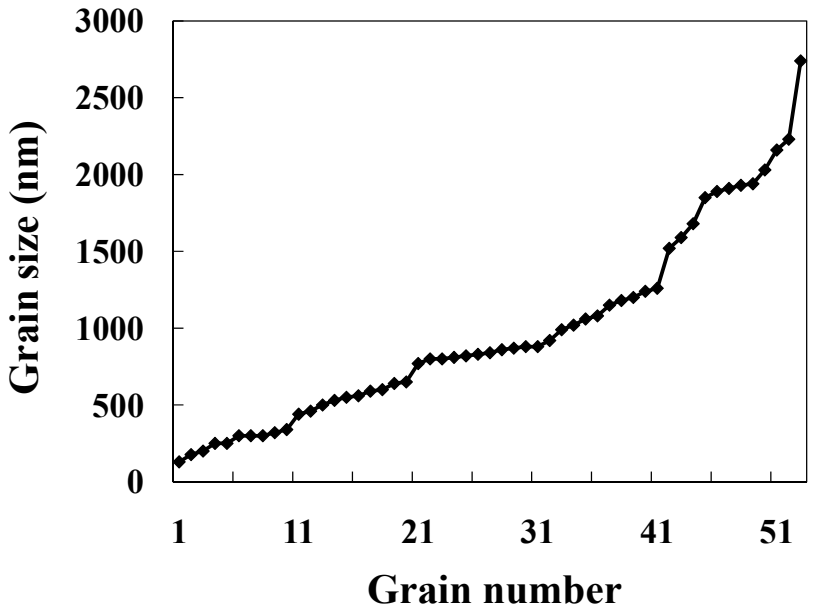

Figure 3.14: Variation of grain size in the SS304+10Al coating. The grain size varied from 130 nm to 2750 nm; the average grain size was estimated as 977 nm.

The grain size distribution of SS304+10Al can be seen in the histogram in Figure 3.15. While there are no columnar grains that have a size less than 100 nm, most of them (> 60%) are in the range of 100 nm to 1 μm. Also, about 30% of the grains are in the range of 1-2 μm, and about 8% of the grains with size > 2 μm are present.

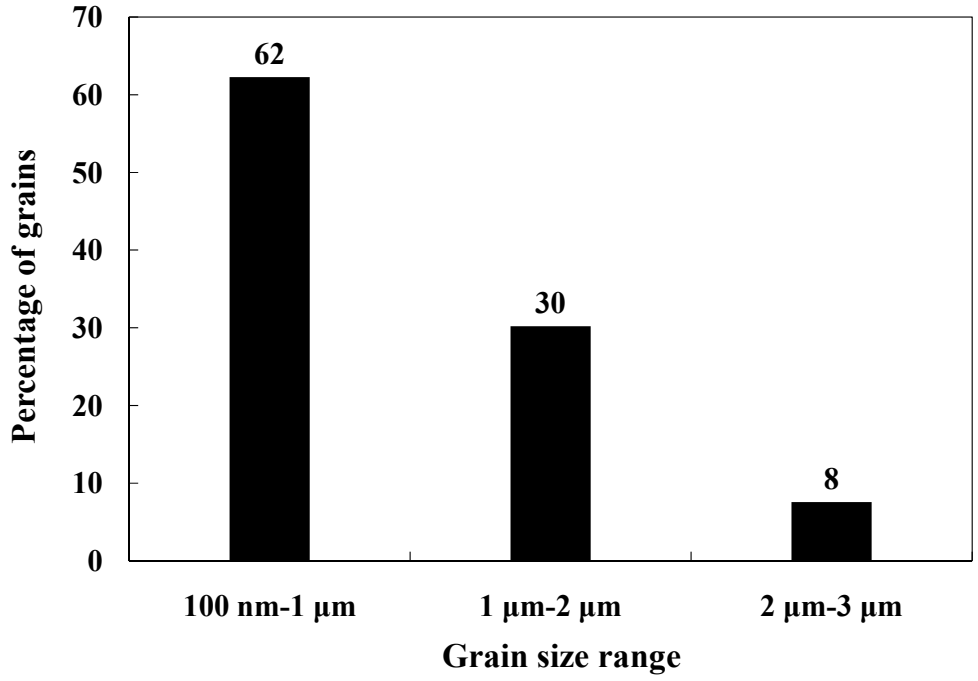

Figure 3.15: Histogram showing the grain size distribution in the SS304+10Al coating.

3.3. Discussion

3.3.1. Overall Grain Size

The variation of grain size in all the four coatings of SS304+Al is shown in Figure 3.16. The average grain sizes in the coatings are approximately 100 nm, 290 nm, 320 nm, and 980 nm, respectively. The grain size in these coatings increased with increasing Al content as noticed from Figure 3.16. The overall grain size variation with superimposed standard deviation is shown in Figure 3.17. Overall histogram of all four coatings is shown in Figure 3.18. Most of the grains are either sub-micron sized or nanocrystalline in nature.

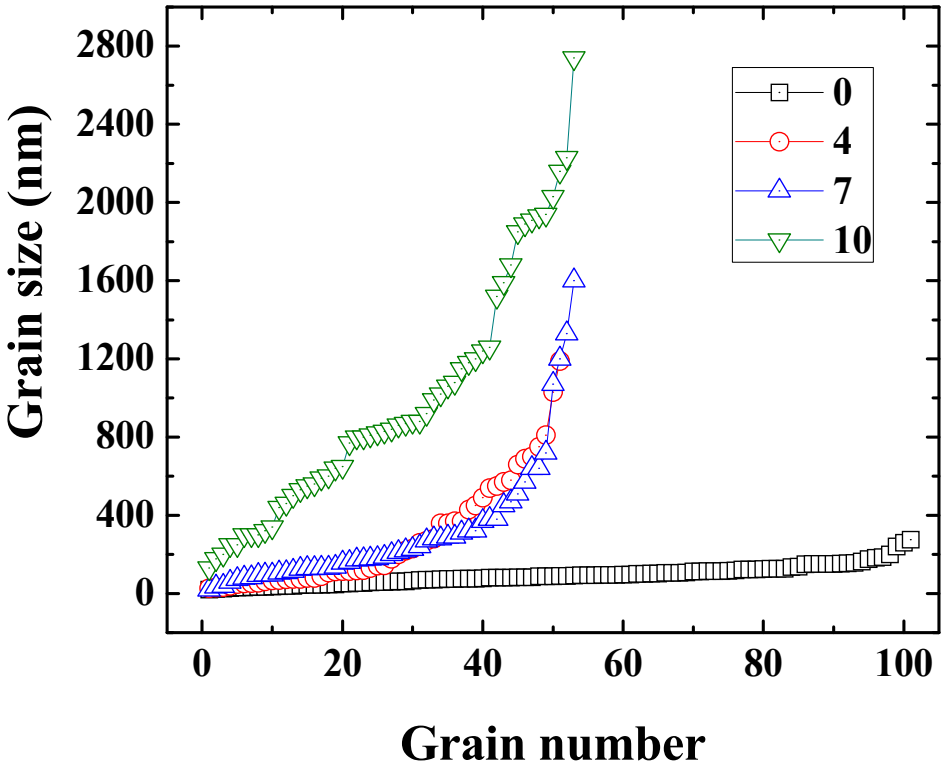

Figure 3.16: The variation of grain size in the SS304+Al coatings.

As observed from Figure 3.16, there is no significant difference in the distribution of grain sizes in 4Al and 7Al coatings. It can be inferred that there are only three types of grain size distributions in the four coatings. Presumably, a change of Al from 4 to 7 wt.% had no effect on the grain size. However, there is a significant increase in grain size from 0% to 4% and from 7% to 10% Al. In the following sections, reasons for such a variation in grain size during sputter deposition are discussed.

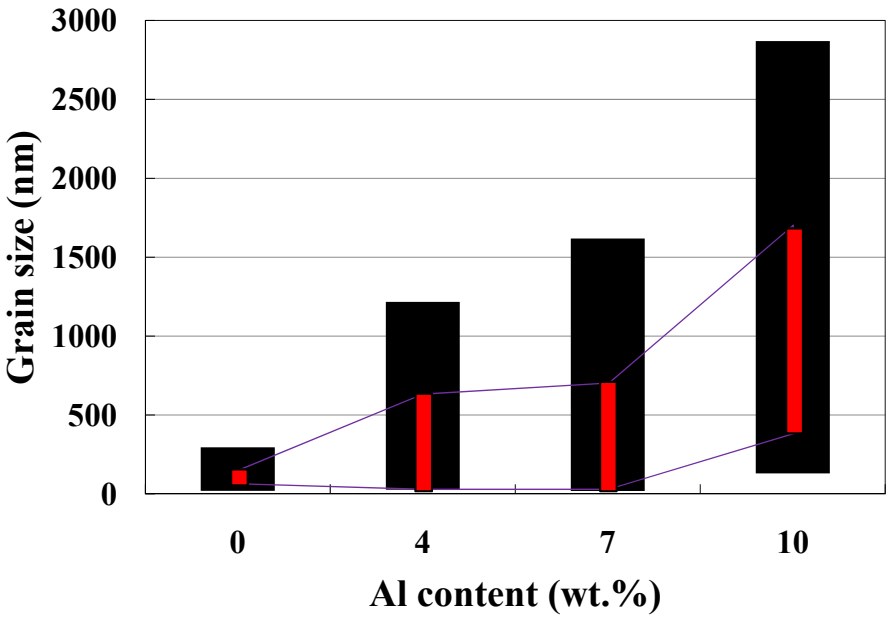

Figure 3.17: Effect of Al on the grain size in the SS304+Al coatings. The extreme bottom and top indicate minimum and maximum grain size. The red bars (color in electronic version) on the chart show standard deviation.

Figure 3.17 shows the minimum and maximum grain sizes and standard deviations of all the four coatings. In addition to the grain size, the standard deviation also varies in the coatings, while it is the minimum in SS304+0Al coating; the same is maximum in 10Al coating.

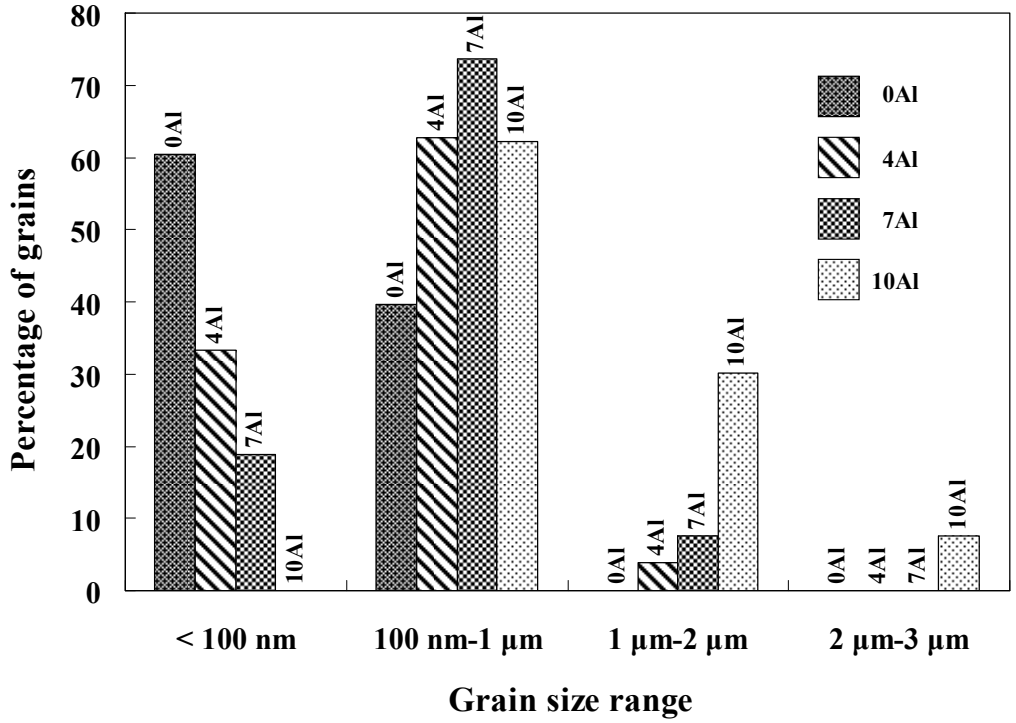

Figure 3.18: Histogram of 0, 4, 7 and 10 Al coatings and their grain size distributions.

Figure 3.18 shows bar chart of grain size distribution in the four ranges, one is the grain size range containing grains less than 100 nm, the second range is 100 nm to 1 µm, the third is 1 µm to 2 µm and the last is 2 µm to 3 µm. In the <100 nm range, increase in Al content shows decrease in the percentage of the grains. In contrary, the range between 100 nm to 1 µm exhibits an increase in the percentage of grains (except in 10Al). Similar trend can be extended to the range between 1 µm to 2 µm and 2 µm to 3 µm

3.3.2. Effect of Al Content on Grain Size

The overall grain size in sputter-deposited materials is influenced by nucleation and growth rates of grains during deposition. Nucleation is of two types- homogeneous and heterogeneous. In vapor deposition, the latter is generally dominant. In such cases, the effect of Al on heterogeneous nucleation becomes important. Heterogeneous nucleation rate is influenced

by substrate condition and the normalized deposition temperature (NDT), which is the ratio of deposition temperature and melting point of the depositing alloy. Since all the substrates were cleaned and polished under similar conditions before deposition, it is reasonable to assume that the grain size was not influenced by the substrate condition. On the other hand, effect of Al on the melting point and consequently on the normalized deposition temperature is negligible. On the whole, Al does not seem to have an apparent effect on heterogeneous nucleation rate.

The second parameter that could influence the grain size is the growth rate. It is possible that addition of Al can have an effect on the growth rate. One point to introduce here is that the deposition temperature used in for the SS304+Al coatings was is not high enough to cause growth by surface area minimization mechanism, which is usually applied in temperatures above recrystallization. A temperature of about 0.6 T_m is required for such grain growth, which is not expected in the current sputtering conditions.

Another mechanism by which grains grow in vapor deposited films is by impingement of similarly oriented grains. That means texture should be present in the sample. While we do have texture in the samples, Al effect is not consistent on the texture with respect to grain size. While 4Al and 10Al coatings show texture, only 10Al sample has larger grains. Hence the influence of Al on texture and hence on the grain size is ignored.

Overall, it is difficult to evaluate the effect of Al on the grain size. This aspect needs lot of further study in order to understand the influence of Al.

Nucleation and growth are generally functions of undercooling. In the present case, substrate temperature, by which we can measure the normalized deposition temperature, becomes important in estimating the grain size. Literature shows how the grain size and grain

structure (shape and morphology) are influenced by NDT in sputter-deposited samples. This will be considered in the following section.

3.3.3. Grain Structure Zones (GSZs)

Overall grain size and grain structure in sputter-deposited materials is primarily determined by normalized deposition temperature (NDT) which is defined as T_s/T_m where T_s is the substrate temperature and T_m is the melting point of the material. The nucleation and growth rates are also important in determining grain sizes. However, they are also eventually influenced by NDT (T_s/T_m). Based on the observed microstructures of the four coatings, it is possible to obtain a reasonable estimate of T_s/T_m. The following section describes how different grain structures are established as a function of T_s/T_m.

Figure 3.19 shows various zones with different grain sizes. By studying the various structure zone models in the literature [1-5], the grain structure in the different coatings can be characterized. In this chapter, the zones are called 'grain structure zones' (GSZ). The following content correlates different zones with microstructures of the four coatings.

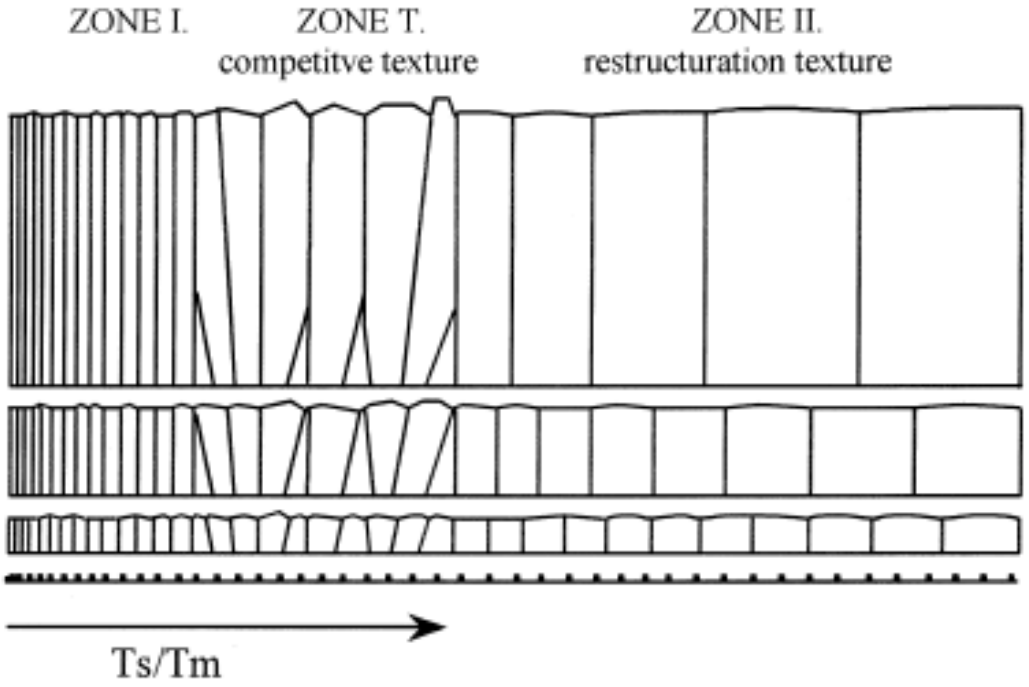

Figure 3.19: Grain structure zone (GSZ) diagram; main characteristics of grain structure zones with respect to the substrate temperature (after Barna and Adamik [1]). Similar description of grains can be found in the Thornton diagram [4]

In zone I, the film is composed of fibers of small diameter (few nm) determined by the nucleation density [1]. The crystalline fibers grow out of the primary nuclei and proceed to the top of the film. The fibers are often collected into bundles. This is a rather homogeneous structure along the thickness of the film with increasing diameter of fibers by increasing T_s/T_m. The crystals contain probably high density of defects and the grain boundaries are porous. This structure belongs to the temperature interval 0 to 0.2 $T_{m,}$ where neither bulk diffusion nor self surface diffusion is significant.

The 0Al coating has microstructure containing nanocrystalline fibrous (few nm to few tens of nm) grains with porosity at/inside the grain boundaries. Since these microstructural features are characteristic of zone I, the coating was understood to be done in zone I. The NDT

(T_s/T_m) of this coating is therefore up to 0.2. Considering the case of 4Al coating, it has several linear nanocrystalline grains like in 0Al coating, but majority of the grains are sub-micron sized with greater than 100 nm in size. Further, the coating rarely has any porosity. Both these factors eliminate the chance to consider the 4Al coating belonging to zone I.

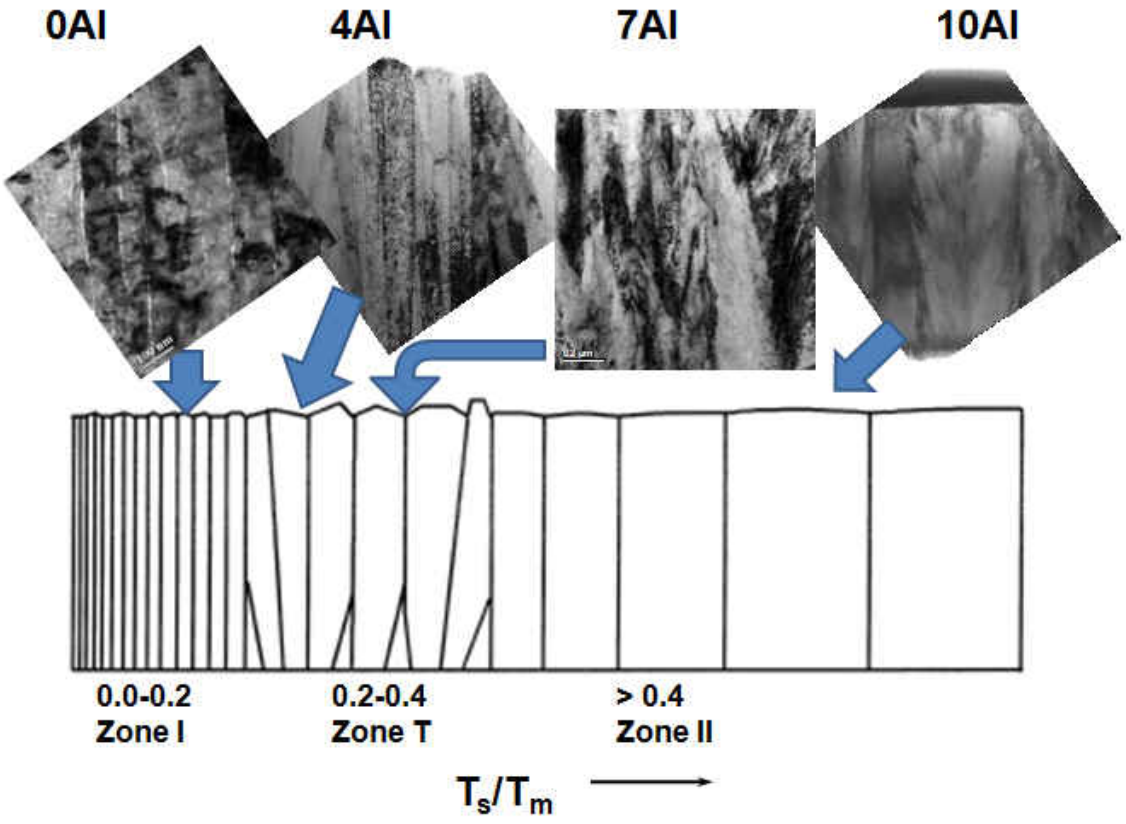

Figure 3.20: Summary of GSZ identification in SS304+Al coating from bright field TEM microstructures

In zone T, the structure is inhomogeneous along the film thickness. It has fine crystallites at the substrate, composed of V-shaped grains in the next thickness range while can be columnar in the upper part of thick films. This zone belongs generally to the temperature interval of 0.2 < NDT < 0.4.

The presence of nanocrystalline grains together with non-linear V-shaped grains along the film thickness, infer that the 7Al coating was deposited in zone T. Hence the NDT estimated for this coating is about 0.3 in between 0.2 and 0.4. The case of 4Al coating is somewhat ambiguous. As mentioned above, it has a mixture of both nanocrystalline and sub-micron columnar grains. In some places grains are very linear while in some other areas they are V-shaped or tapered. Comparing the grain size distribution of 4Al and 7Al coatings from Figure 3.16, where the distribution is very similar, it is suggested that 4Al coating also belongs to the zone T.

Zone II represents a homogeneous structure along the film thickness composed of columnar grains penetrating from the bottom to the top of the film. The grain boundaries are nearly perpendicular to the film plane. This zone is characteristic of high substrate temperatures NDT > 0.4.

Similar microstructure with large vertical columnar grains was indeed observed in 10Al coating and hence it is understood that the coating was deposited in zone II. Figure 3.20 summarizes the identification process.

Once the above zones and corresponding T_s/T_m for the coatings are identified, it is possible to estimate the T_s if the melting points of the alloys used for the coatings are known. The alloys used for the coatings are Fe-18Cr-8Ni-Al with Al contents of 0, 4, 7 and 10 wt.%. Melting points of these alloys were estimated from ternary Fe-Cr-Ni and Fe-Ni-Al phase diagrams (shown in Figure 3.21).

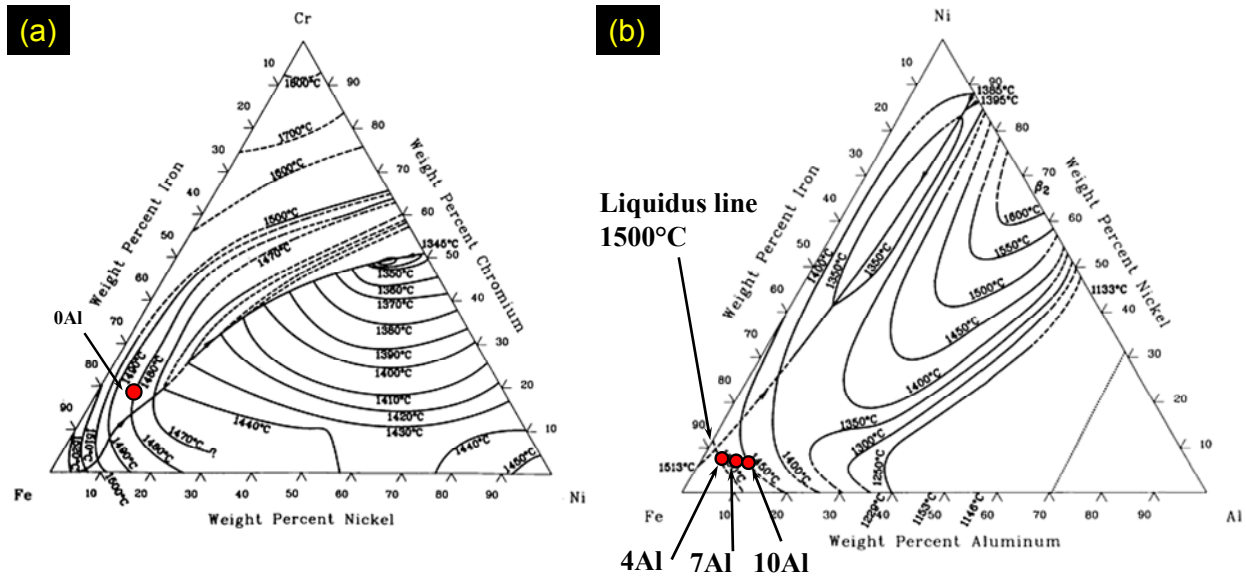

Figure 3.21: (a) Liquidus projection of ternary Fe-Cr-Ni phase diagram; melting point of Fe-18Cr-8Ni is found out to be about 1480 °C. (b) Liquidus projection of Fe-Ni-Al ternary phase diagram; melting points of 4, 7 and 10 wt.% Al coatings are found to be approximately 1500 °C, 1475 °C and 1450 °C respectively [6].

Figure 3.21 shows the liquidus projections of Fe-Cr-Ni and Fe-Ni-Al alloy phase diagrams. The melting points of the four alloys were read from the ternary alloy phase diagrams. The values for 0, 4, 7 and 10% Al coatings are 1480, 1500, 1475 and 1450 °C respectively. Table 3.1 relates various coatings, GSZs and corresponding T_s/T_m values and finally substrate temperatures.

Table 3.1: Derivation of approximate substrate temperatures, T_s from GSZ diagram using the grain structure obtained from electron microscopy.

Wt.% Al	**T_m, °C**	**Comments and correlation to GSZ**	**Zone**	**T_s/T_m**	**T_s, °C**
0	1480	Predominantly nano fibrous grains with porosity	Zone I	< 0.2	< 78
4	1500	Composed of nano and sub-micron sized columnar grains, with no porosity	Zone T	~ 0.3	~ 259
7	1475	Composed of nano and sub-micron sized columnar grains, without porosity	Zone T	~ 0.3	~ 251
10	1450	Predominantly large and vertical columnar grains without porosity	Zone II	> 0.4	> 416

3.3.4. Reasons for Variation in Substrate Temperatures

Sputter-deposition on SS304 substrates was carried out using plasma enhanced magnetron sputtering (PEMS). The "enhanced plasma" was generated in the sputtering chamber using tungsten filament with the purpose of increasing the coating density. This plasma is in addition to magnetron plasma, which is always there during magnetron sputtering. While the enhanced plasma increases the Ar ion flux by 25 times and increases the deposition density, it also raises the deposition temperature. In addition to the temperature raise caused by the enhanced plasma, atomic impingement during sputter deposition itself can increase the temperature of the coating, depending on deposition time and other sputtering variables. This increased temperature could have significant effect on the microstructural features of the deposits. Continuous dual-fold rotation mechanism of the substrates during PEMS makes it almost impractical to measure the temperature by direct methods.

3.4. Conclusions

The grain size of SS304+Al (with 0, 4, 7 and 10 wt.% Al) sputter deposited coatings has been studied. The average grain sizes are about 100, 290, 320 and 980 nm respectively. In 0Al fibrous grains containing porosity indicated that the coating was deposited at very low temperature of zone I. In 4Al and 7Al coatings, mixed types of linear, tapered and V-shaped grains together with nano and sub-micron size clearly pointed to the transition deposition zone which is zone T. Large vertical columnar grains of 10Al coating indicated a NDT of > 0.4 which is in zone II. Hence, it is obvious that the grain size variation is closely related to GSZs or T_s/T_m value which in turn is related to T_s, the substrate temperature. Higher substrate temperatures, especially in 10Al coating, led to a large increase in grain size. Hence the substrate temperature is the primarily parameter that is responsible for the grain size variation. Effect of Al on the grain size is difficult to understand with such a large variation in substrate temperatures.

3.5. References

1. P.B. Barna and M. Adamik, Fundamental structure forming phenomena of polycrystalline films and the structure zone models, Thin Solid Films, 317 (1998), p.27
2. C.R.M. Grovenor, H.T.G. Hentzell, and D.A. Smith, The development of grain structure during growth of metallic films, Acta. Metall, 32 (1984), p.773
3. I. Petrov, P.B. Barna, L. Hultman, and J.E. Greene, Microstructural evolution during film growth, Journal of Vacuum Science & Technology A: Vacuum, Surfaces, and Films, 21 (2003), p.S117
4. J.A. Thornton, Influence of apparatus, geometry and deposition conditions on the structure and topography of thick sputtered coatings, Journal of Vaccum Science and Technology, 11 (1974), p.66
5. J.A. Thornton, High rate thick film growth, Annual Review of Materials Science, 7 (1977), p.239

6. T.B. Massalski, ed., Binary Alloy Phase Diagrams, 2nd edition (1990) ASM International, Materials Park, Ohio.

CHAPTER 4: PHASE IDENTIFICATION IN SS304+Al COATINGS

4.1. Introduction

Phase identification is a major step in understanding microstructure. In the previous chapter, grain size of Al-added 304-type austenitic stainless steel (SS304) was presented. The objective of this chapter is to identify the phases present in the four coatings containing various Al contents starting from 0 to 10 wt.%.

Two major steps were involved in phase identification of the sputter-deposited SS304+Al coatings. The first step was XRD characterization as it helps in identifying phases in a much faster, easier and more economical way than TEM. It was done before doing any TEM. The second step was TEM characterization which has unique advantages of identifying phases locally, finding the distribution of phases, and identifying their chemistry. The crystallographic method (electron diffraction) was predominantly used to identify the phases in the present TEM study.

4.2. Results

4.2.1. X-ray Diffraction

It is known that 304-type stainless steel belongs to austenitic grade. In order to make sure of this aspect, XRD of both target and substrate was carried out. In agreement, XRD patterns of SS304 target and SS304 substrate were observed to be having predominantly the austenite. Figure 4.1 shows the XRD pattern of SS304 target. It has FCC crystal structure with a lattice parameter of about 0.36 nm. A minor amount of ferrite was also observed in the target.

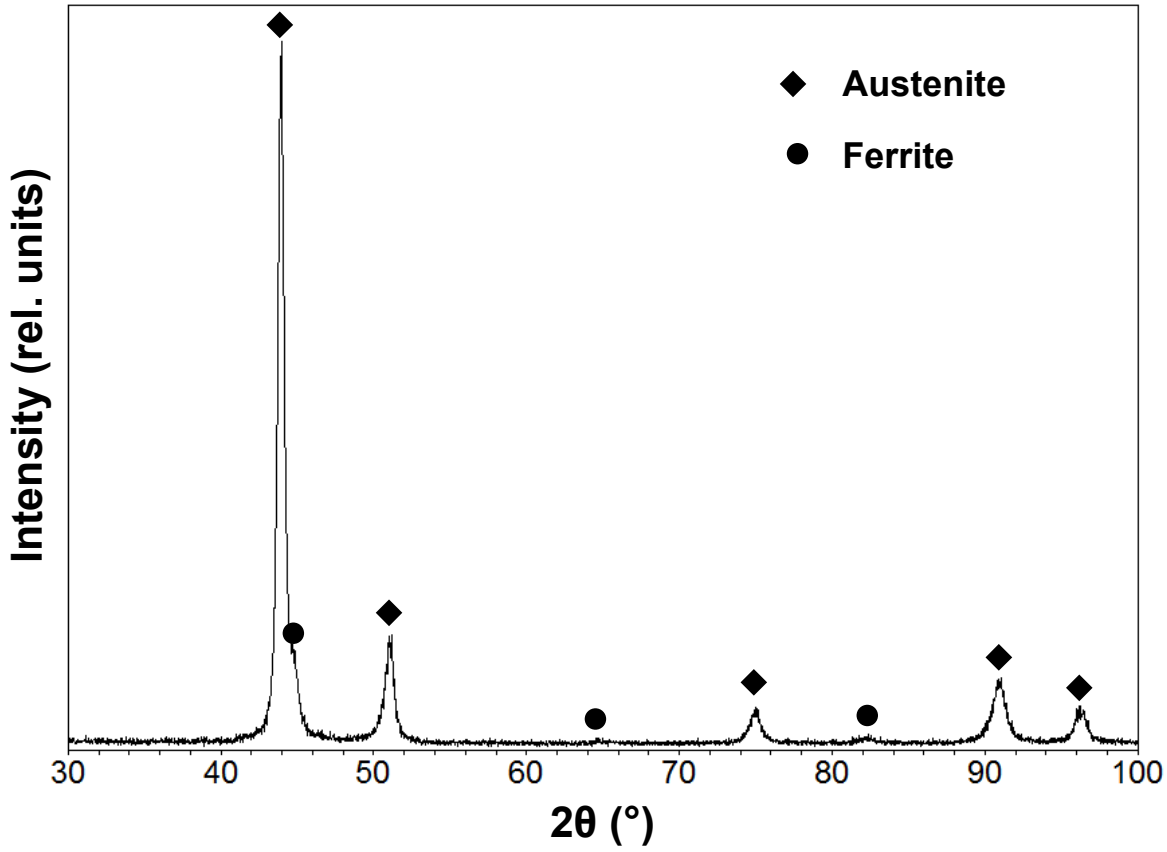

Figure 4.1: XRD pattern of the SS304 target showing predominantly the austenite

Of the four coatings, 0Al sample (SS304 on SS304 substrate) showed the most complex XRD pattern (See Figure 4.2). Individual peak indexing is also given in the Figure 4.2, which demonstrates that there are two phases, one is the ferrite (α) and the second is the intermetallic phase sigma (σ). The lattice parameter of the observed α phase is 0.2872 nm. The lattice parameters for the tetragonal sigma phase are a = 0.884 nm and c = 0.458 nm.

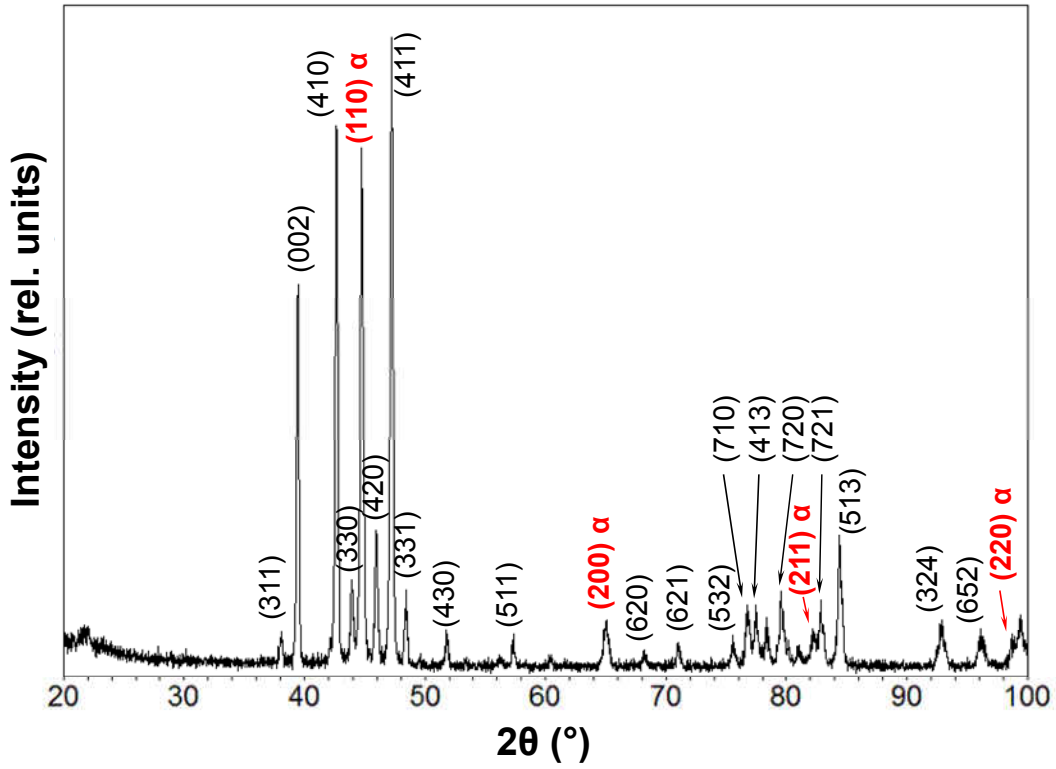

Figure 4.2: XRD pattern of 0Al coating. Two phases were found, one was ferrite (marked with symbol α in bold font) and second was sigma (remaining all peaks)

Figure 4.3 shows XRD patterns of all the four coatings. In the figure, peaks corresponding to the sigma phase are not labeled in 0Al, since a comprehensive indexing was done in Figure 4.2. Regarding 4Al and 7Al coatings, the vertical lines in Figure 4.3 indicate (110), (200), (211) and (220) peaks of ferrite phase. An unidentified peak could also be noticed at 2θ of 46.5° in 4Al coating.

Figure 4.3 shows the XRD pattern of SS304+10Al coating marked as 10Al. Five peaks are observed and are indexed. Based on their *d*-spacings and indexing, the phase identified is B2. Based on the superlattice peak of B2 phase (at 2θ of about 31° - (100) peak), B2 phase was identified in the coating. However, all other superlattice peaks are absent in the range from 20-100°. Another observation is that the most intense peak in the pattern is (200), even though (110) peak should be the most intense in B2. This indicates that there is preferred orientation in the (002) of the coating.

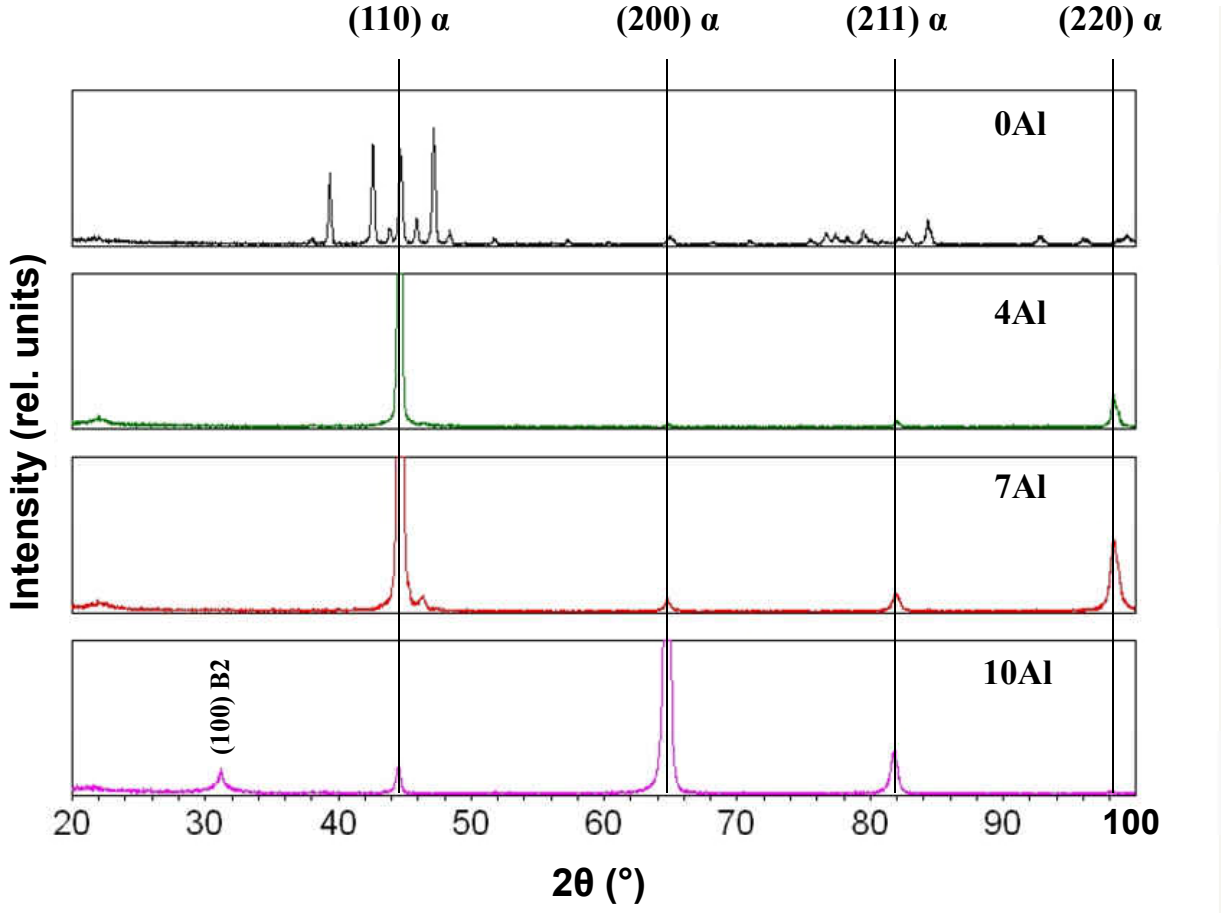

Figure 4.3: XRD patterns of SS304+Al coatings. In 0Al coating, except the four α peaks (vertical lines), all other belong to σ phase.

For measuring *d*-spacings, peaks have been fitted to pseudo-Voigt profile together with 'linear background'. Precise lattice parameters have been calculated for the ferrite/B2 phases in the four coatings using Nelson-Riley function from the *d*-spacings of planes. The resultant precise lattice parameters of the ferrite phases in coatings are listed in Table 4.1. The value of '*a*' was observed to be increasing with increasing Al content.

Table 4.1: Summary of the precise lattice parameters (PLP or *a*) of the SS304+Al coatings, as identified from the X-ray diffraction patterns. Note that PLP in SS304+0Alcoating (0.2875 nm) is slightly larger than the lattice parameter measured from the (220) peak (0.2872 nm).

Sample	Wt.% Al	PLP, *a* (nm)
SS304+0Al	0	0.2875
SS304+4Al	4	0.2881
SS304+7Al	7	0.2885
SS304+10Al	10	0.2885

4.2.2. Transmission Electron Microscopy

4.2.2.1. SS304+0Al Coating

Figure 4.4 shows a couple of bright field micrographs of the overall microstructure of SS304+0Al coating. Vertically aligned columnar grains have been observed in the coating. Description of grain structure, size distributions etc were given in the previous chapter.

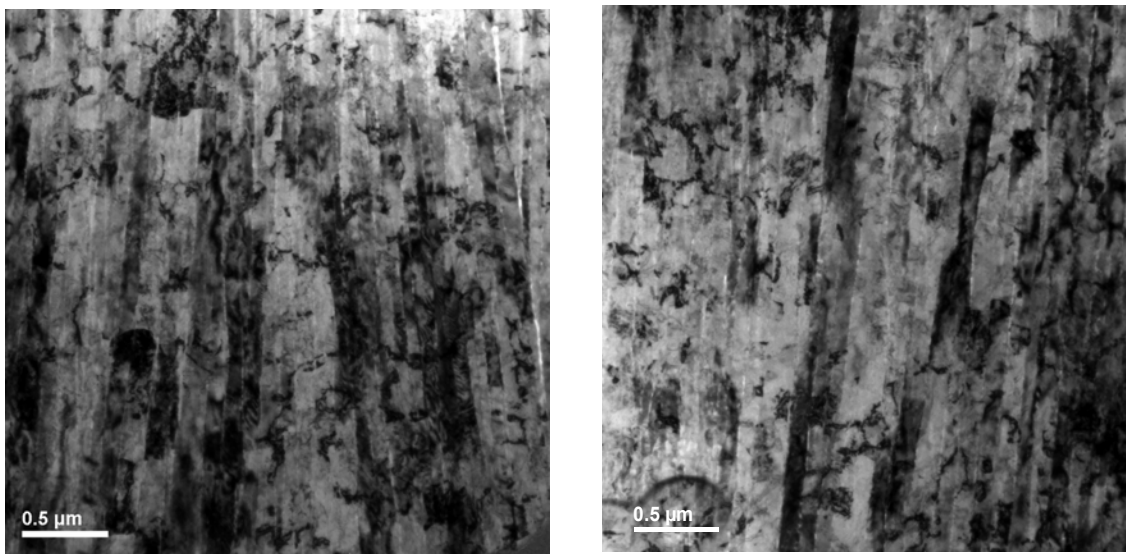

Figure 4.4: TEM bright field images of SS304+0Al coating showing vertical columnar grains

Figure 4.5 shows a ring DP with indexing. There are two types of rings in the DP, continuous and discontinuous. Continuous rings belong to the ferrite phase while discontinuous or spotty rings belong to the sigma phase.

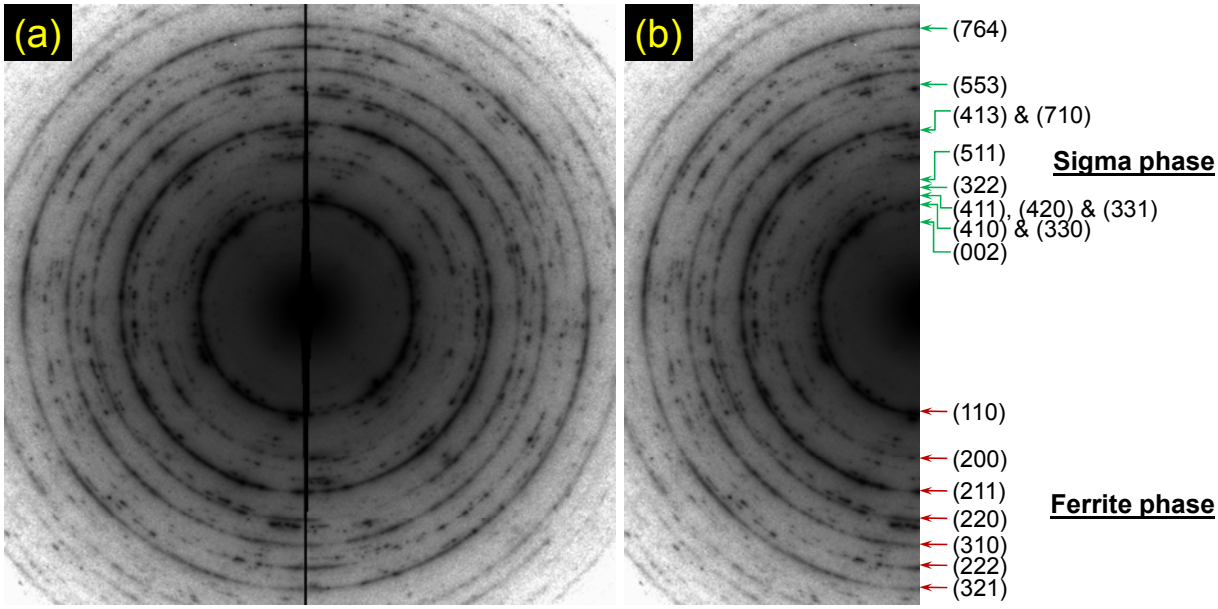

Figure 4.5: Ring DP (a) 360° (b) 180°, with indexing that demonstrates the presence of two phases α and σ

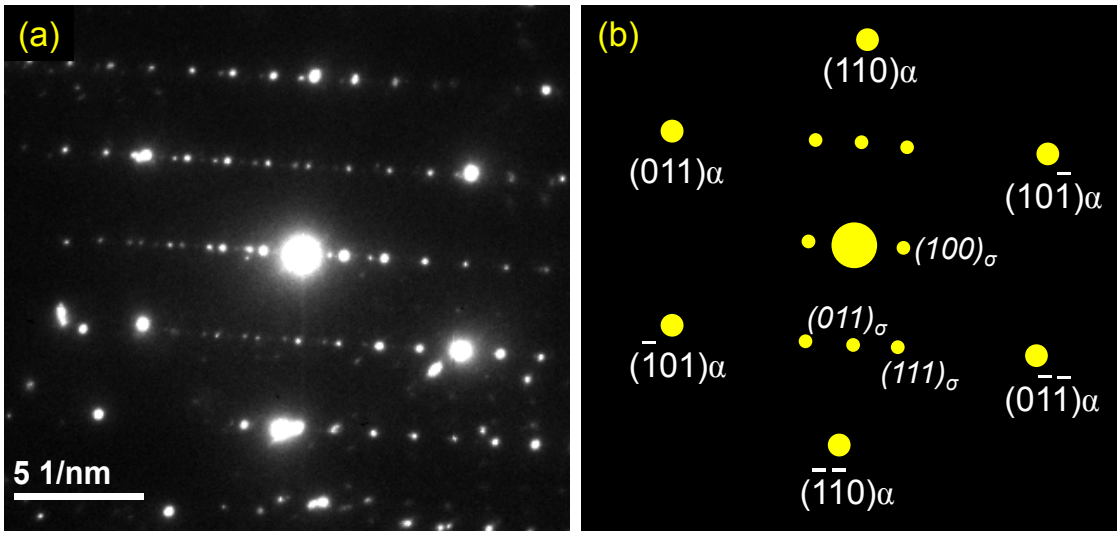

Figure 4.6: (a) SAD pattern from a composite region of matrix and precipitate in 0Al coating and (b) corresponding indexing that shows the lower intense spots near transmitted beam belong to the sigma phase. Electron beam was parallel to $[1\bar{1}1]$ direction of α and $[0\bar{1}1]$ direction of σ.

In addition to the ring DP, SADPs were also recorded. Figure 4.6(a) shows one such DP with indexing in Figure 4.6(b). The ferrite spots are intense while sigma spots are relatively less intense and closer to the transmitted beam because of the larger lattice with tP30 structure. In this alloy coating, the results of XRD and TEM complement each other. Both show the presence of ferrite and sigma phases.

4.2.2.2. SS304+4Al Coating

A typical BF and DP from SS304+4Al are shown in Figure 4.7. In agreement with XRD of the 4Al coating, ferrite phase was observed in TEM DPs. A minute amount of B2 phase was also present, which was inferred from the faint superlattice (100) type spots in [001] zone axis as shown in Figure 4.7(b).

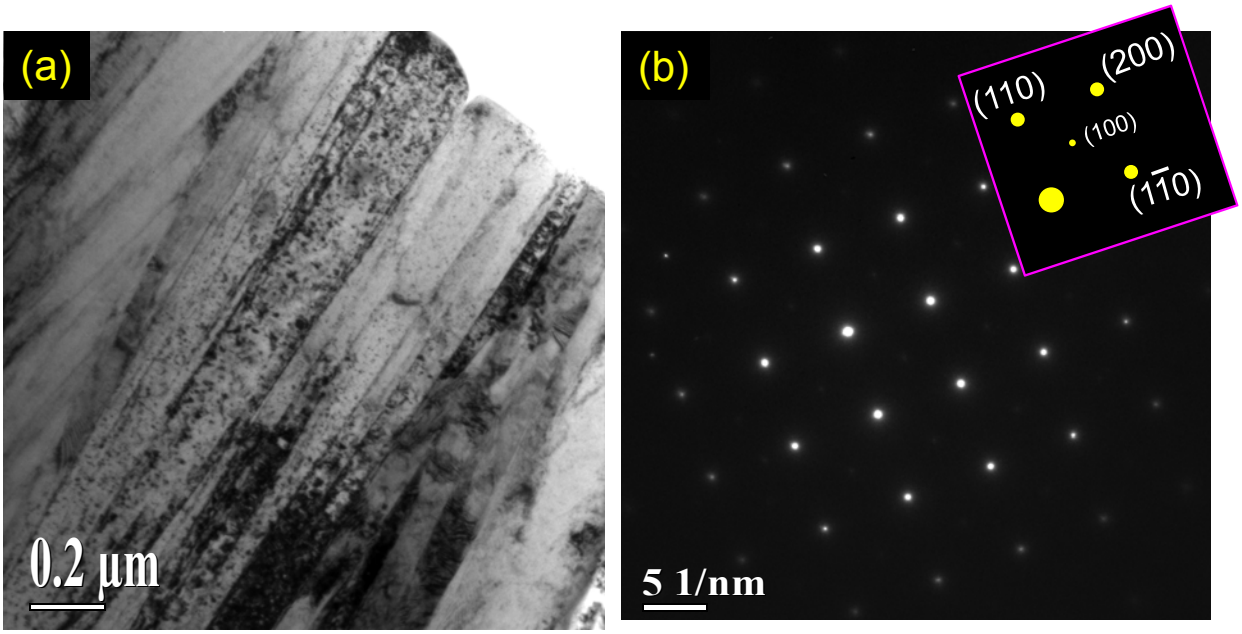

Figure 4.7: (a) Densely packed columnar grain structure in bright field TEM micrograph of the SS304+4Al coating. (b) SAD pattern from a single grain. Inset indexing reveals the presence of α with [001] zone axis. Presence of B2 phase can also be sensed from the superlattice spots in DP- although the intensity of those spots is very less.

4.2.2.3. SS304+7Al Coating

Figure 4.8 shows a BF, DF and ring DP from the SS304+7Al coating. The DF was taken from the enclosed spots (shown circled in Figure 4.8(c)). The DF hence contains the information of several grains. Indexing of the ring DP from the same location is shown in Figure 4.8(c). The indexing clearly indicates the presence of a BCC phase, which is nothing but α phase. A brief mention, about a (100) spot that is closer to the transmitted beam shown in Figure 4.8(d), is that it belongs to ordered B2 phase. For additional information on α and B2 phases, DP analysis was done in different orientations. Figure 4.9(a) shows a single crystal DP with [111] zone axis; *d*-spacings confirmed the presence of α. The presence of second phase B2 was also revealed from single crystal DP. Figure 4.9(b) shows typical DP from [001] zone axis making the presence of superlattice B2 phase clear.

This particular composition, SS304+7Al, exemplifies the importance of the TEM technique in phase identification compared to XRD. In the XRD, no peaks corresponding to the ordered or superlattice structure were seen. But in TEM, the presence of superlattice plots in SADPs and hence the ordering was clearly observed. The reason why XRD could not identify the ordering perhaps is that the ordering could be too localized and small in quantity.

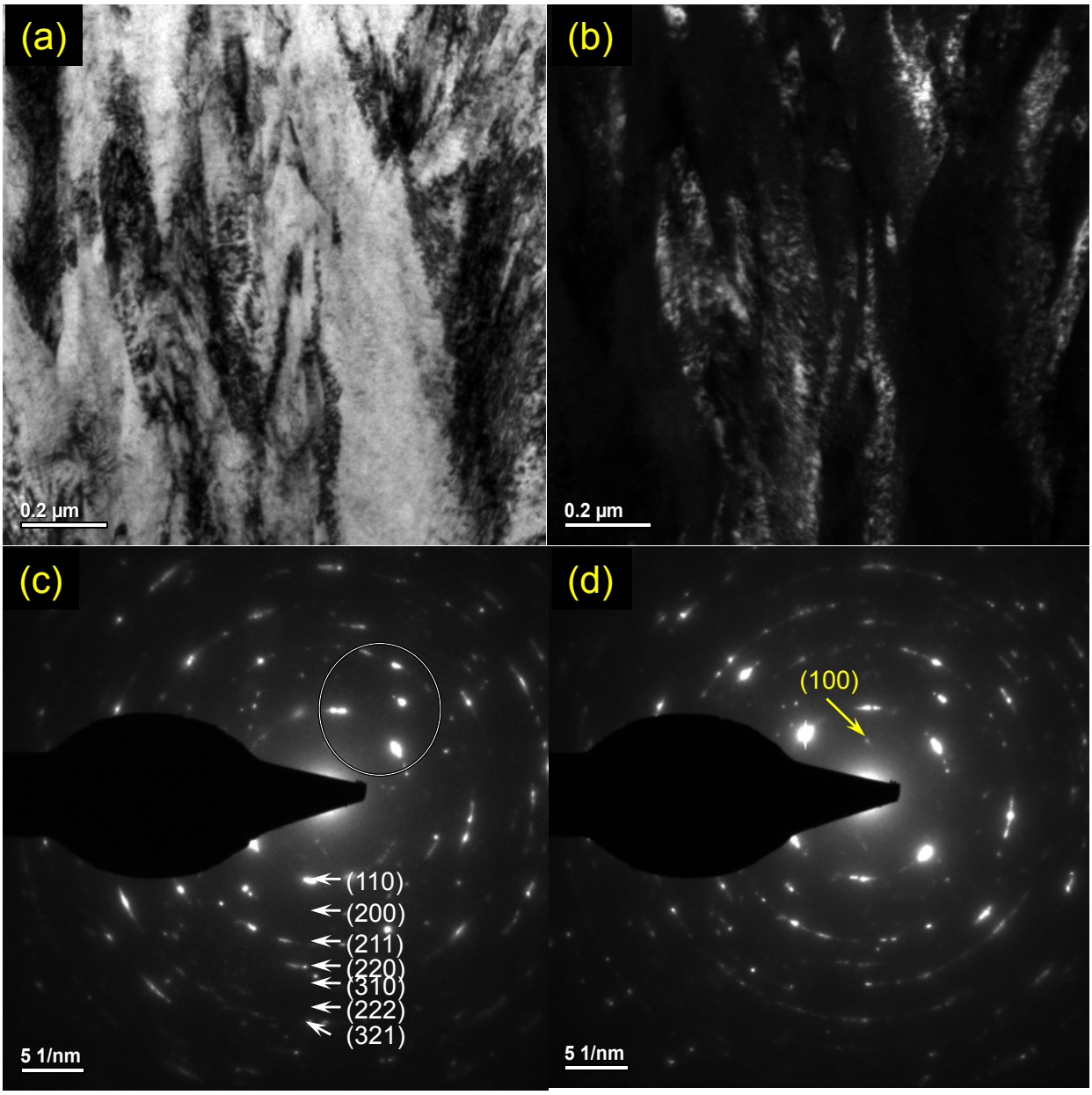

Figure 4.8: (a-d) Series of TEM BF, DF and DPs of SS304+7Al coating. DF was taken from the marked area in (c). The indexing of ring pattern in (c) shows that the primary phase is α. A B2 superlattice (100) spot can also be seen similar DP in (d).

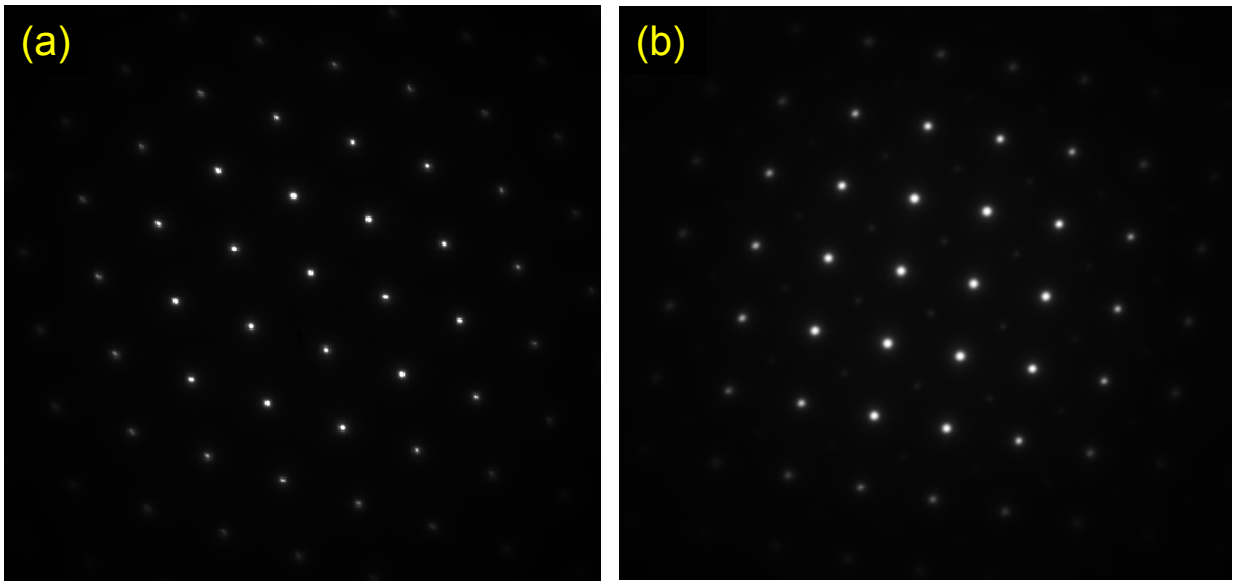

Figure 4.9: SADPs from of SS304+7Al coating. (a) Electron beam parallel to $[1\bar{1}1]$ (b) Electron beam parallel to [001]

4.2.2.4. SS304+10Al Coating

The difference between the TEM studies of this coating and other three coatings (with less Al), is that both cross-sectional and in-plane samples study was carried out in this coating whereas only cross-sectional study was carried out in the remaining three. Not only this additional in-plane sample helped in counting more grains, for the grain size study in the previous chapter, it also helped in detailed microscopic study. As noticed earlier in XRD, two phases (i) α-phase (ferrite) and (ii) B2 ordered phase were also identified in TEM. Complementing the XRD results, TEM studies also showed the existence of B2 phase and/or α-phase, whose presence was confirmed by SADPs at several regions of both samples. Figure 4.10(a-c) shows BF, DP with indexing from a cross-sectional sample. The DP belongs to the central grain of the microstructure.

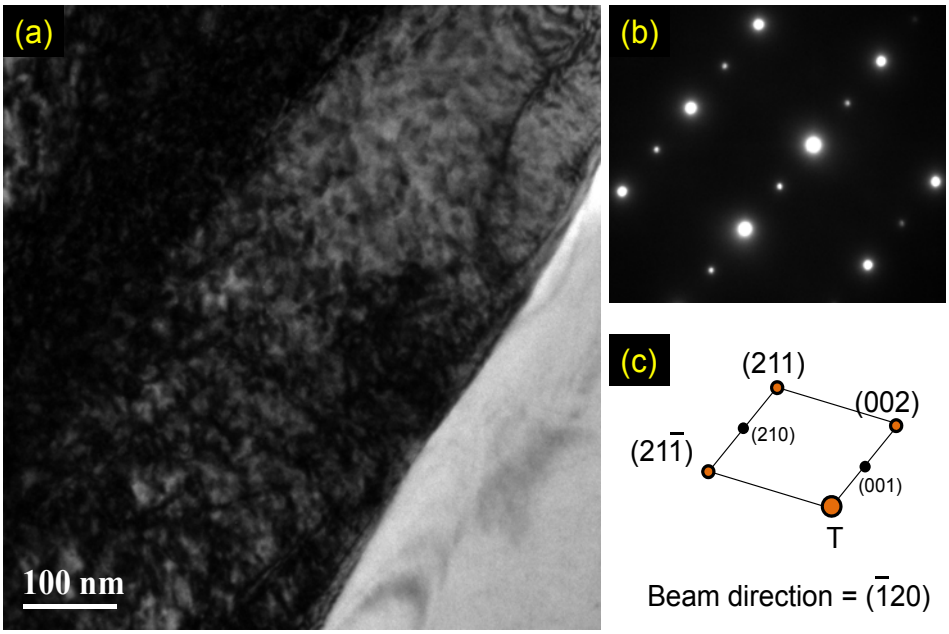

Figure 4.10: (a) bright field micrograph of SS304+10Al caoting. (b) DP showing the presence of both fundamental and superlattice spots (c) Indexing as shown in simulated DP

In order to identify the distribution of B2 phase and hence distinguish it from ferrite, high magnification study was carried out. Figure 4.11 shows BF, DF and SADP from [001] zone axis. DF, which was taken from circled $(0\bar{1}0)$ superlattice spot, shows tiny crystals of B2 distributed all over the microstructure. In some areas of DF, the distribution was denser than the other. From such an uneven distribution, it could be assessed that B2 phase was not uniform. The discontinuity was caused by the absence of B2 in several locations where α phase was present. Hence it can be understood that there are two phases. This observation is found to conform to equilibrium phases present as per phase diagram, which will be brought out in a later section of this chapter.

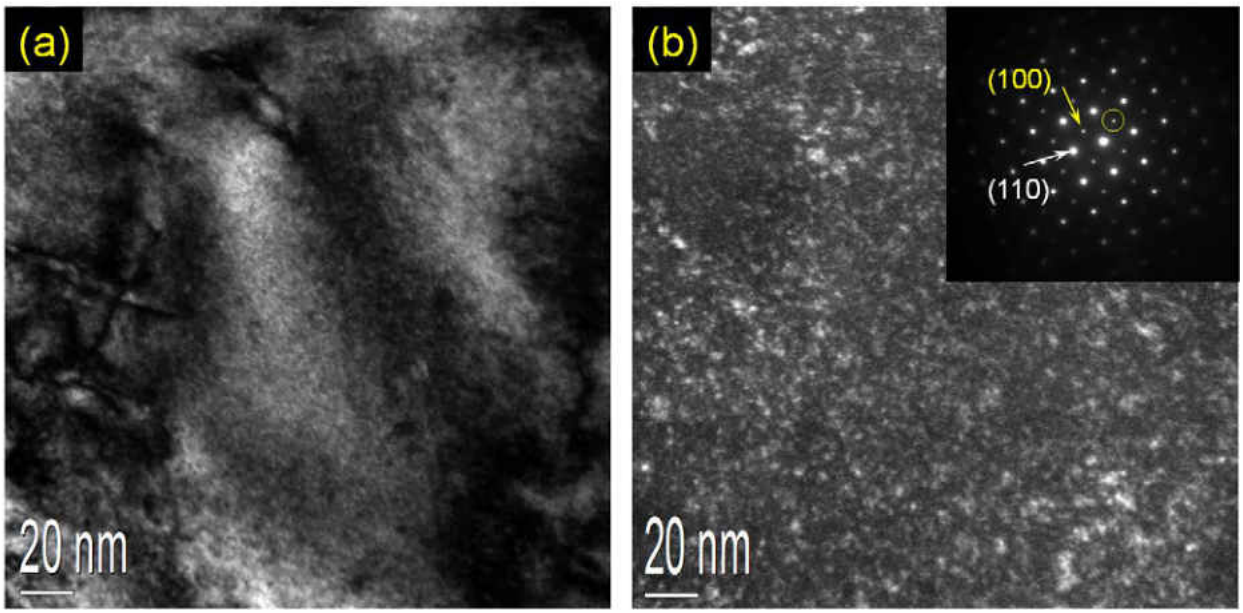

Figure 4.11: (a) Bright field micrograph at high magnification from SS304+10Al coating. (b) Corresponding DF micrograph taken from (100) superlattice spot showing the presence of tiny B2 crystallites < 5 nm in size. Inset shows the 4-fold DP from [001] zone axis.

4.3. Discussion

From the nominal composition, possible equilibrium phases have been identified from the phase diagrams. The Fe-Cr-Ni phase diagram was used for 0Al coating while the Fe-Ni-Al phase diagram was used for the remaining three coatings.

4.3.1. Phases in SS304+0Al Coating

Figure 4.12 shows the XRD pattern of the SS304 taregt and SS304+0Al coating. Two phases in each sample were identified from indexing of the target and coating. Target contains predominant phase as austenite (γ) and the minor phase as ferrite (α). However, the phases observed after PEMS are different. As identified earlier, the phases present in the coating are ferrite and sigma. Both these phases are non-equilibrium phases.

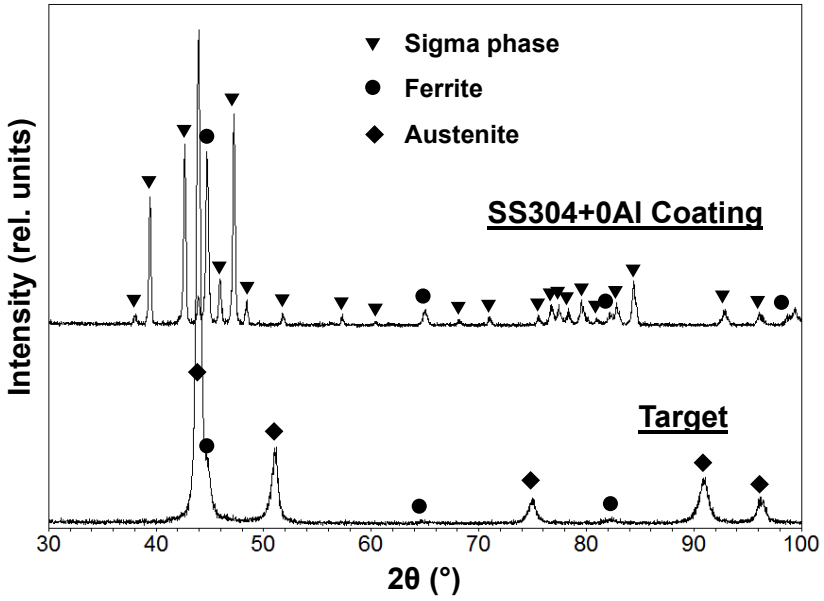

Figure 4.12: Overlaid XRD patterns of SS304 target and SS304+0Al coating

Sigma phase is an intermediate phase with tetragonal (tP30) crystal structure with composition AB, where A and B are transition metals. Unlike line compounds, this intermediate phase has a broad composition range. It is known to be present in at least 43 binary systems [1]. It is observed to be stable at relatively high temperatures. Formation of ferrite in sputter-deposited SS304 was observed earlier [2-3]. A separate chapter (Ch.5) is devoted to study the non-equilibrium phase formation of ferrite and sigma phases.

4.3.2. Phases in SS304+Al Coatings

SS304+Al alloys make a quaternary system (Fe-18Cr-8Ni+Al). In order to find the equilibrium phases of these alloys, an assumption is made to reduce the quaternary system to a ternary one. That is, assuming Cr behaves similar to Fe, thus reducing the system to ternary Fe-8Ni-Al compositions. Since the melting points, of the binary alloys Fe with Cr up to about 20 wt.%, or with Ni up to about 10 wt.%, are about 1500 °C, the above assumption seems to be reasonably valid to evaluate melting points of the SS304+Al. Figure 4.13 shows the ternary Fe-Ni-Al phase diagrams at 20 °C and 600 °C. Phase formation of the Al added coatings SS304+Al, has been assessed from these two phase diagrams. The three filled circles indicate the three compositions corresponding to 4, 7, and 10 wt.% Al.

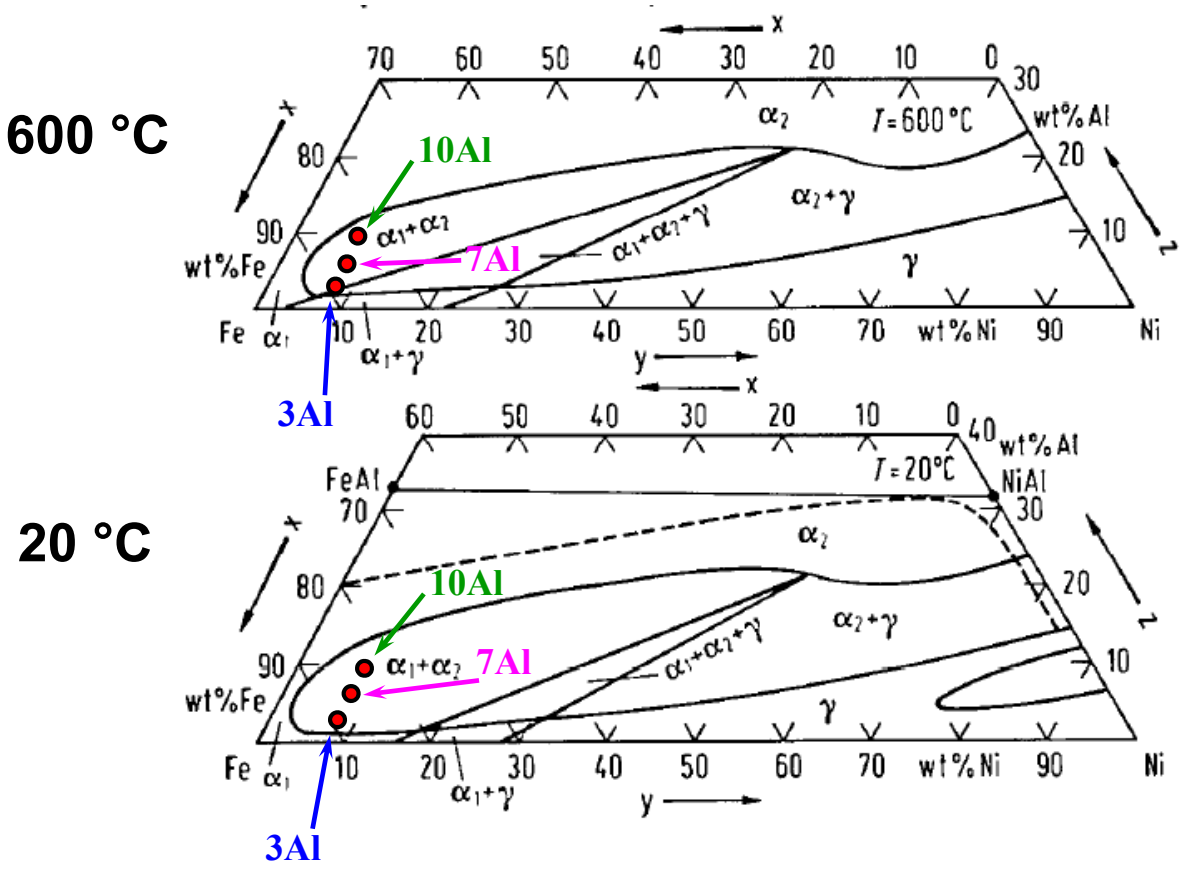

Figure 4.13: Truncated ternary Fe-Ni-Al phase diagram at two temperatures [4]. Phases present are only two- ferrite (marked as α_1) and B2 (marked as α_2). Phase boundaries between single phase α_2 and γ (bottle shaped) are not changing with change in temperature from 20 and 600°C. It indicates that the temperature has only a limited effect on the quantities of ferrite and B2 phases. However, it can be noticed that increase in the Al content increases the relative amount of B2 phase.

Right from 20 °C to 600 °C, the three compositions have the same phases, ferrite (marked as α_1) and B2 (marked as α_2). But their relative quantities are different with different Al contents. As expected, and also noticed from the phase diagrams, the amount of B2 phase increases with increasing Al content. In TEM phase identification, it was indeed found that B2 phase existed in all the Al-added coatings and that the intensity of superlattice spots increased with Al content (Figure 4.14) indicating larger B2 quantity. Hence, there is a strong correlation between the phase diagram data and experimental results in terms of phases present. Assuming the SS304+xAl is following the Fe-Ni-Al phase diagram, a conclusion can be made that Al-added SS304 sputter-deposition led to equilibrium phases. The ternary Fe-Ni-Al phase diagram also indicates that B2 phase is the primary phase and α is a secondary phase in 10Al coating.

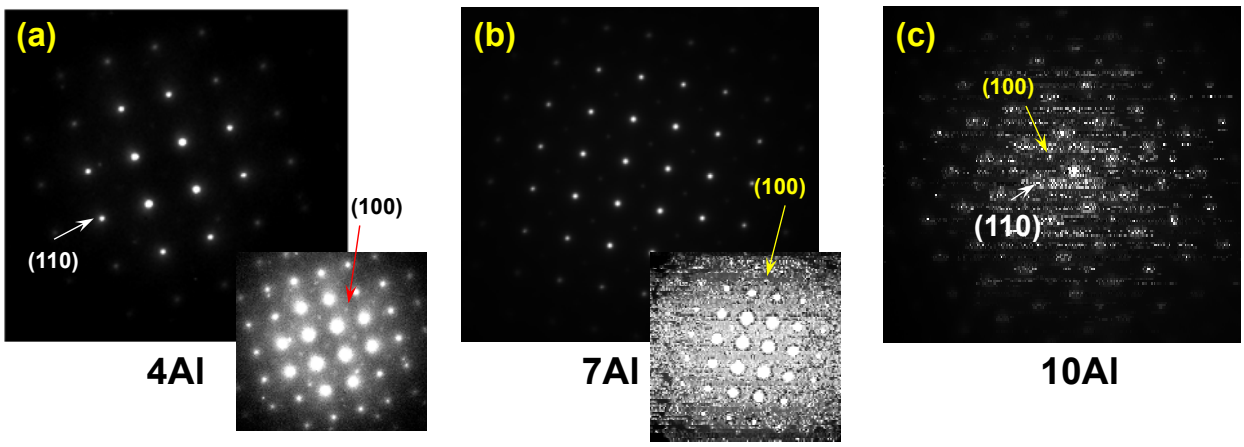

Figure 4.14: (a-c) SADPs from [001] zone axes of SS304+4Al, 7Al and 10Al coatings showing ordering. Note that the (100) spot intensity relative to (110) intensity is increasing with increasing Al content. The subordinate DPs of SS304+4Al and 7Al coatings are enhanced for better visibility of (100) spots.

Table 4.2: Summary of the phases identified from XRD, TEM as compared to the equilibrium data.

Wt.% Al	Phases from XRD	Phases from TEM	Phases from equilibrium diagrams
0	α and σ	α and σ	mostly γ
4	α	α and B2	α and B2 [4]
7	α	α and B2	α and B2 [4]
10	B2	α and B2	α and B2 [4]

As seen from Table 4.2, sigma phase is absent in any Al added coatings. This indicates that addition of 4 wt.% Al could eliminate sigma phase formation in SS304, the reason being, that Al is a strong ferrite and B2 stabilizer.

4.4. Conclusions

Phase identification was carried out by x-ray diffraction and electron diffraction methods. In 0Al, α and σ phases were present. In SS304+4Al, 7Al and 10Al coatings, α and B2 phases were present although their relative amounts varied with Al content. Phase diagram correlation showed that α and σ phases in SS304+0Al coating are non-equilibrium phases. On the other hand the α and B2 in the Al-added SS304 coatings are equilibrium phases. TEM was more sensitive to the phases present as it identified B2 phase even in SS304+4Al coatings.

4.5. References

1. J.M. Joubert, Crystal chemistry and calphad modeling of the sigma phase, Progress in Materials Science, 53 (2008), p.528
2. S.D. Dahlgren, Equilibrium phases in 304L stainless steel obtained by sputter-deposition, Metallurgical Transactions, 1 (1970), p.3095
3. S.D. Dahlgren, E.D. McClanahan, J.W. Johnston, and A.G. Graybeal, Microstructure of sputter-deposited 304L stainless steel, Journal of Vacuum Science and Technology, 7 (1970), p.398
4. T. Nakamichi, *7.2.1.5 bcc-type magnet alloys with spinodal decomposition*, H.P.J. Wijn, Editor. 1992, SpringerMaterials - The Landolt-Börnstein Database. (http://www.springermaterials.com) DOI: 10.1007/10028076_15.

CHAPTER 5: FORMATION OF FERRITE AND SIGMA PHASES IN SS304+0Al COATINGS

5.1. Introduction

Normal solidification conditions promote face-centered-cubic (FCC) structure in 304-type austenitic stainless steels. However, from the previous chapter (Ch.4), it was noted that metastable phases, ferrite and sigma had formed during the deposition of SS304 by PEMS processing. The purpose of the present chapter is to understand the reasons by which these two phases are forming. The observation of ferrite phase has been widely reported in sputter-deposited austenitic stainless steels [1-10],. In addition to vapor deposition, formation of ferrite from austenitic SS304 was also observed during rapid solidification [11-12], laser processing [13], and mechanical alloying [14]. However, formation of the sigma phase has been reported rarely in sputter-deposited steels [15], although it has been reported during heat treatment of the austenitic stainless steels [16-18].

Sigma phase is an intermediate phase with a tetragonal (tP30) crystal structure with the composition AB, where A and B are transition metals. Unlike line compounds, this intermediate phase has relatively broad composition range. It is generally observed in alloy systems containing elements having similar atomic radii and is more stable at relatively high temperatures. It is known to be present in at least 43 binary systems [19]. Technologically, it is a harmful phase as its presence embrittles the alloys under consideration.

The sigma phase is commonly observed in Fe-based alloys containing high Cr, Mo and V, which are subjected to prolonged heat treatment at high temperatures. If the steel is quenched through the temperature zone of sigma in the phase diagram, the phase is not expected to form. This is because the kinetics of the phase formation are very slow. In binary Fe-Cr, Fe-Mo, and

Fe-V alloys, the sigma phase is stable till 830 °C, 1611 °C and 1252 °C, respectively [20]. Table 5.1 lists the ranges of temperature and composition for sigma phase stability.

Table 5.1: Equilibrium composition and temperature range for sigma phase stability of in binary Fe-based alloys

Fe-M	**Temperature Range (°C)**	**Composition Range**	
		(Wt.% M)	**(At.% M)**
Fe-Cr	440-830	42.7 to 48.2	44.5 to 50.0
Fe-Mo	1235-1611	56.3 to 69.2	42.9 to 56.7
Fe-V	Room temperature-1252	30.0 to 65.0	32.0 to 67.1

In addition to the above binary alloys, steels containing three or more elements are also prone to sigma phase formation. Particular to Fe-Cr-Ni alloys, the sigma phase was predicted to be present in the range at least from 427°C [21] to more than 900°C [20]. The objective of this chapter is to study the influence of various factors that could possibly cause the sigma phase during the PEMS processing of SS304+0Al coatings.

5.2. Results

5.2.1. X-ray Diffraction

Figure 5.1 shows the XRD patterns of SS304 target and the sputter-deposited coating. As identified from the previous chapter, the SS304+0Al coating contains the ferrite phase with a lattice parameter of 0.2872 nm and the sigma phase with the lattice parameters, a = 0.8840 nm and c = 0.458 nm.

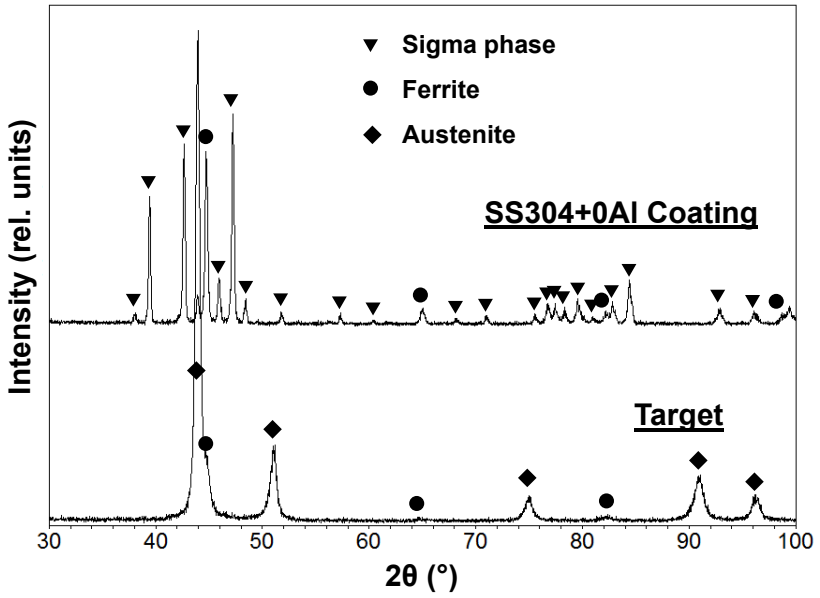

Figure 5.1: Overlaid x-ray diffraction patterns of SS304 target (bottom) and SS304+0Al coating (top); while austenite is the major phase in SS304, ferrite phase and sigma phase were observed in the PEMS coating.

5.2.2. Scanning Electron Microscopy

Typical planar and cross-sectional views of the SS304+0Al coating are shown in Figure 5.2. The appearance of equi-axed type grain structure in in-plane can be noticed (But they are columnar grains). The cross-section view shows the columnar grains in microstructure.

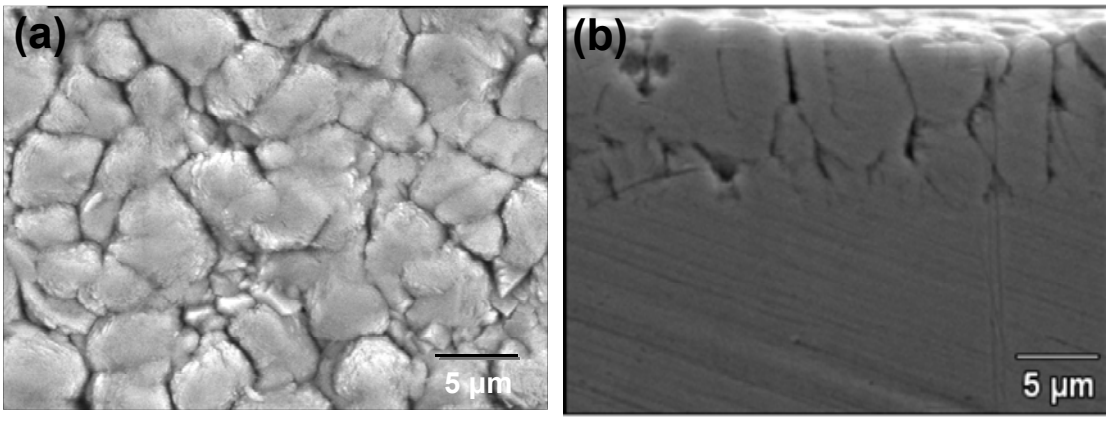

Figure 5.2: SEM micrographs showing the SS304+0Al coating in (a) in-plane view and (b) cross-section view

The composition of SS304 coating was measured from several locations using EDS in SEM. Several x-ray line and area scans including x-ray mapping have been employed to evaluate the elemental distribution and consequently to identify the presence of sigma phase. Table 5.2 compares the average composition of the 0% Al coating with that of target and substrate. Important point to notice is that average Ni content was less than the target composition while average Cr composition was more than average. Attention was paid especially to the Ni depletion and Cr enrichment issue as this observation has been consistent.

Table 5.2: Composition of the SS304 target, substrate and coating (wt.%). Cr and Ni values indicate that Ni is less in quantity in the coating than the substrate while Cr is more.

	Fe	**Cr**	**Ni**	**Mn**	**Si**	**Trace Elements**
0% Al Coating (x-ray mapping)	72.27	**19.82**	**6.99**	0.56	0.35	-
0% Al Coating SwRI SEM	72.00	**20.20**	**7.00**	0.40	0.40	-
Coating (line scan)	71.27	**23.02**	**4.92**	0.45	0.34	-
Target (Manufacturer)	71.05	18.52	8.13	1.36	0.41	0.53
Substrate (Manufacturer)	71.33	18.25	8.09	1.25	0.36	0.72
Substrate (line scan)	71.37	**17.96**	**8.10**	1.99	0.59	-

Figure 5.3(a) shows the cross-sectional SEM micrograph of the SS304 coating. The coating thickness is roughly about 8 µm. However, the coating thickness mentioned in the Ch.2 was 27 µm. Few sides of the coatings showed significantly lesser coating thickness. The Figure 5.3 is from one of such locations. EDS line scan was carried out across the interface between coating and substrate in the SS304+0Al sample (the downward arrow). The corresponding composition profile is shown in Figure 5.3(b). Significant difference in the composition of Cr and Ni contents in the coating and substrate was noticed. Higher Cr and lower Ni were observed in the coating. At several locations in the coating, Cr content reached up to 30 wt.% while in the same location Ni content reduced up to 2 wt.%.

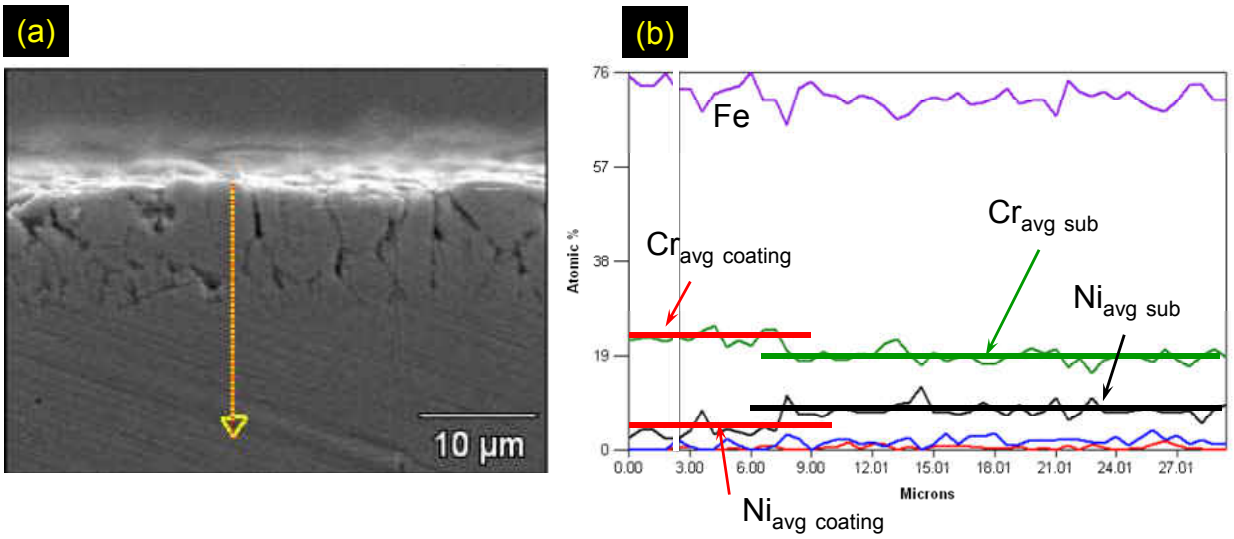

Figure 5.3: (a) SEM micrograph showing the SS304+0Al coating on SS304 substrate (b) Typical EDS line scan across the coating substrate interface showing the distribution of Fe, Cr, Ni, Mn and Si. The horizontal lines indicate average Cr and Ni compositions of the substrate and coating. Table 5.2 shows the average contents

5.2.3. Transmission Electron Microscopy

Figure 5.4 shows a bright field (BF) electron micrograph of the overall microstructure of the as-deposited SS304 coating.

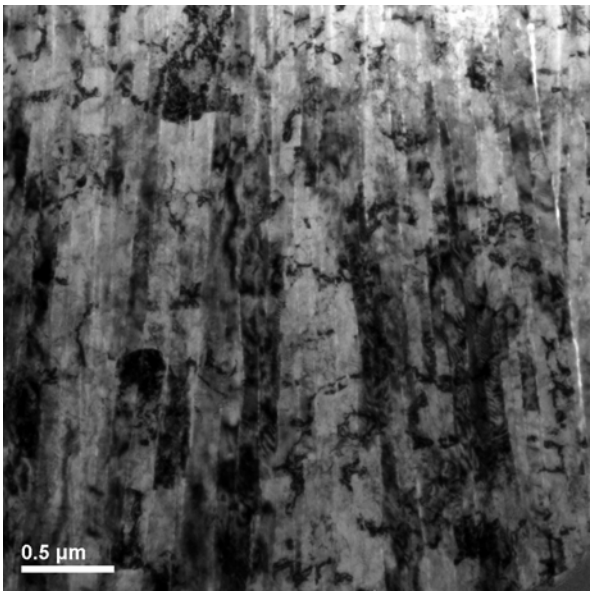

Figure 5.4: TEM Bright-field micrograph of the SS304 coating. Columnar grains can be observed throughout the sample.

Figure 5.5 shows BF, DF and DP and its indexing from a region containing σ phase. Indexing of the DP was possible only on the basis of sigma phase. DF was recorded from the encircled spot Figure 5.5(c). Figure 5.5(b) shows the distribution of sigma phase.

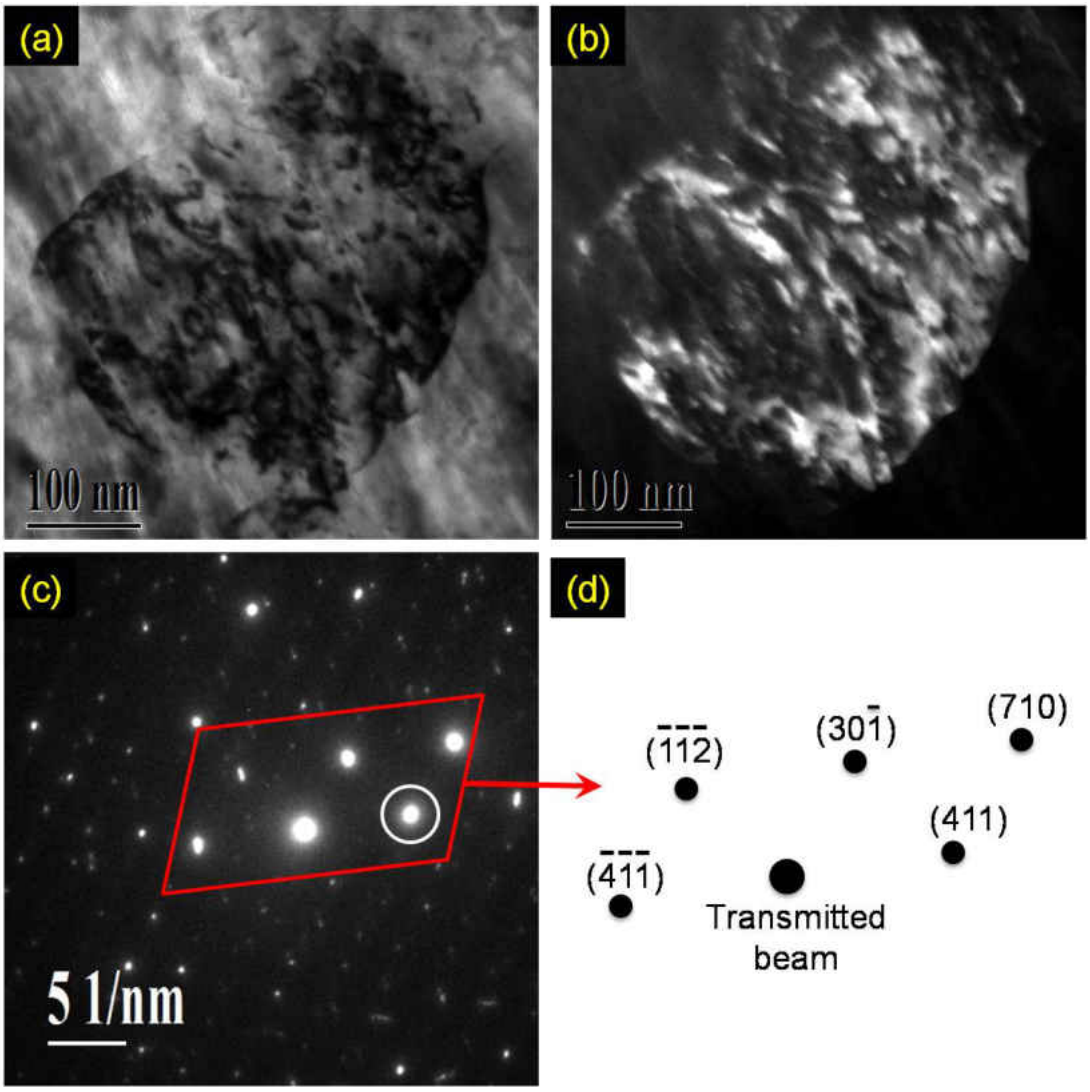

Figure 5.5: (a) Bright-field, (b) dark field TEM micrographs and (c) electron diffraction pattern from a region corresponding to sigma phase. Dark field micrograph was taken from the encircled spot of sigma phase. (d) Indexing of the spot pattern

5.3. Discussion

It is known that under normal solidification conditions austenite is the stable phase in 304-type austenitic stainless steel (SS304). However, formation of metastable phases, ferrite and sigma, was noticed in the sputter-deposited SS304. The following discussion addresses the formation of both phases.

5.3.1. Formation of Ferrite Phase

Our observation of the formation of ferrite in sputter-deposited SS304 was in agreement with the earlier work [1-10]. In addition to vapor deposition, formation ferrite from austenitic SS304 was also observed during rapid solidification [11-12], laser processing [13], and mechanical alloying [14].

A few different explanations were put forth by researchers to explain the formation of ferrite. Zhang et al. [8] related the formation to moderate Ni depletion during sputter-deposition from the SS304 target. Cusenza et al. [9] further developed the idea and related it to the nanocrystalline grain size of the sputter-deposit. They also considered the effect of Ni and substrate temperature during deposition. Since Ni is a strong austenite stabilizer, the quantity of Ni becomes an important factor while considering the austenite to ferrite transformation during sputter-deposition. Figure 5.6 elaborates the influence of Ni and substrate temperature on phase formation in several austenitic stainless steels. As per the schematic, a minimum of 9-10 wt.% Ni at lower temperatures (< 300 °C) or a substrate temperature of 650 °C with minimum of 6-7 wt.% Ni are the prerequisites for the appearance of austenite in sputter-deposited SS304.

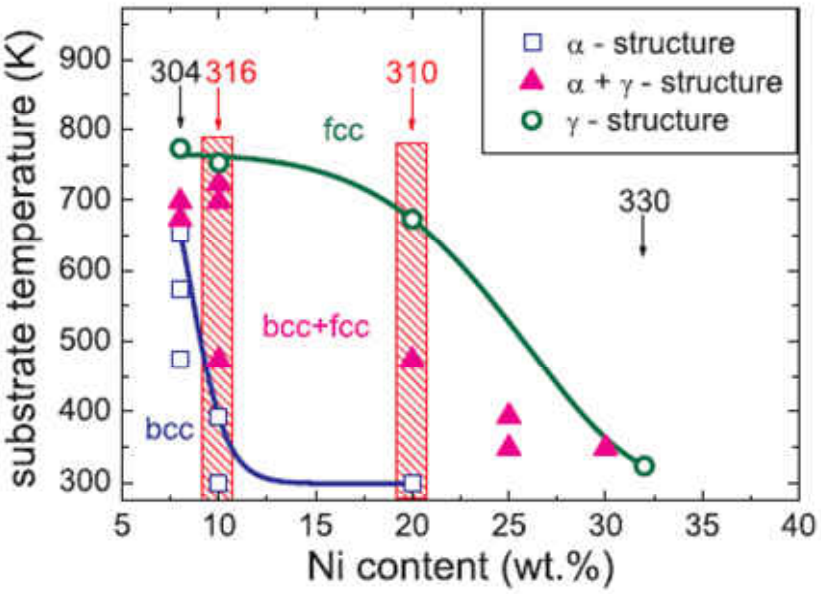

Figure 5.6: Effect of Ni content on the phase formation of various stainless steels [9]

In the current study, a deposition/substrate temperature less than 78 °C was estimated. Further Ni content was found out to be about 7 wt.%. Both these conditions are in the bcc zone of the Figure 5.6 and hence it is quite evident that ferrite (bcc) phase is more stable instead of austenite fcc in SS304 during sputter-deposition.

5.3.2. Formation of Sigma Phase

While ferrite phase formation was commonly observed in sputter-deposited 304 steels, formation of sigma phase in SS304 was rarely reported [15]. The following aspects are considered to discuss the formation of sigma phase.

5.3.2.1. Cr and Ni Contents, and Equilibrium Sigma Phase Fields

As seen from the introduction of this chapter, sigma phase in steels could appear by the addition of elements like Cr, Mo and V. However, only Cr could influence sigma phase in the present case as the total quantity of Mo and V is less than 0.33 wt.%, which is negligible. According to the binary Fe-Cr phase diagram [20] above 460 °C, sigma phase can co-exist with Fe and Cr based BCC phases from as low as 7 wt.% Cr to as high as 88 wt.% Cr. As Cr content increases quantity of sigma phase also increases (up to about 48 wt.%).

It is possible to study the sigma phase in ternary Fe-Cr-Ni by correlating the above description on binary Fe-Cr alloys. Figure 5.7(a) shows the ternary Fe-Cr-Ni phase diagram at 650 °C. Sigma phase can be stable between 18% Cr to 66% Cr at this temperature. Higher the Cr content higher is the quantity of sigma phase (up to about 50 wt.% Cr depending on Ni content).

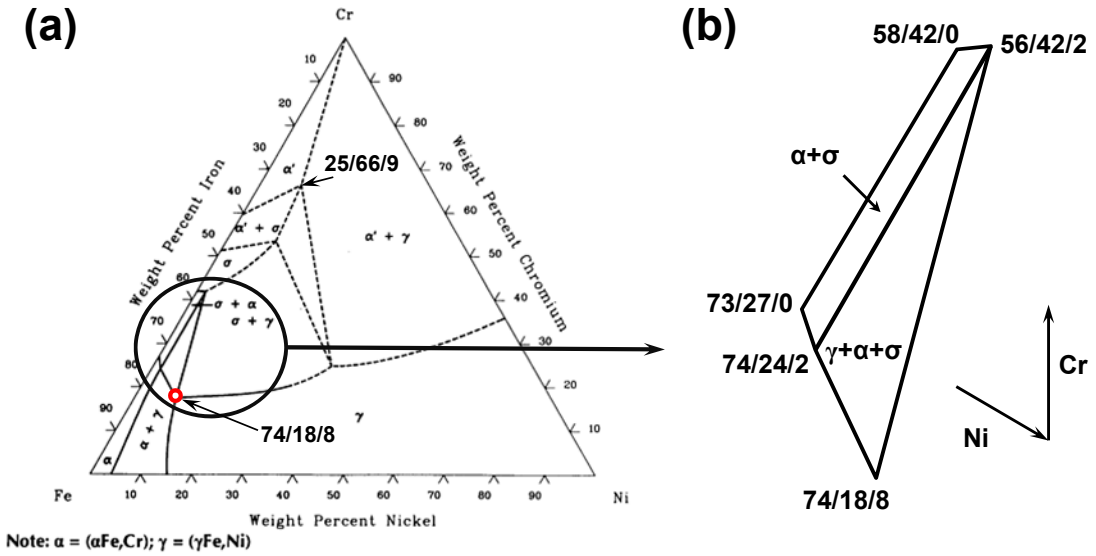

Figure 5.7: Fe-Cr-Ni ternary phase diagram with isothermal section at 650 °C [20] with a circle showing zones where sigma phase is present (b) enlarged version of the sigma phase fields with Fe/Cr/Ni compositions marked. Arrows show the direction of increasing Cr and Ni. The numbers (ex. 74/18/8) represent Fe/Cr/Ni wt.% compositions.

Figure 5.7(a) also shows an encircled zone highlighting sigma phase fields. The region is redrawn in a magnified scale in Figure 5.7(b) which also shows Fe/Cr/Ni ternary compositions at intersecting boundaries. The zone has two different phase fields. One of them has α and σ while the second one has γ, σ and α phases, as shown. All the observed coating compositions fall in the zone and hence thermodynamically, the steel coating can develop sigma phase, although the relative quantity of which, depends on actual composition.

Table 5.3 shows the Fe, Cr and Ni contents obtained either from EDS analysis in SEM studies of the coating or substrate or target compositions obtained from the manufacturer. All these compositions fall in the enclosed phase diagram zone.

Table 5.3: Fe-Cr-Ni compositions of coating, substrate and target. Increase in Cr content and decrease in Ni content is noticed in the SS304+0Al coating. Both these factors promote ferrite and sigma phase formation/stabilization.

	Fe	**Cr**	**Ni**
0% Al Coating (x-ray mapping)	72.27	**19.82**	**6.99**
Coating (line scan)	71.27	**23.02**	**4.92**
Substrate (line scan)	71.37	17.96	8.10
Substrate (Manufacturer)	71.33	18.25	8.09
Target (Manufacturer)	71.05	18.52	8.13

The Cr and Ni arrows in Figure 5.7(b) indicate an increase in their quantity in the direction of arrow. Starting from 74/18/8 of Fe/Cr/Ni (bottom corner), it can be seen that with increasing Cr and decreasing Ni, the resultant movement is towards the center of the zone in

Figure 5.7(b). Since the zone contains three phases γ, σ and α, they should appear under equilibrium conditions.

In the above section, it is reported that the γ to α transformation is common in sputter-deposited SS304. Since austenite to ferrite transformation is usual in the sputter-deposited 304 steels, ferrite is observed instead of austenite. However, more intriguing problem here is the formation of sigma phase at temperatures less than 78 °C (the deposition temperature). The condition that needs to be met here is to have high temperature. Since the sigma phase is forming at room temperature, and is not seen in usual solidification conditions, it is presumably a non-equilibrium phase.

5.3.2.2. Ni Depletion and Cr Enrichment

Ni depletion was consistently observed through the EDS both in SEM and TEM studies. Figure 5.3 and Table 5.3 show the difference in Cr and Ni contents in the coating compared to substrate. Very similar depletion was also observed by other researchers [8] and formation of ferrite was solely attributed to depletion of Ni. Reasons for Ni depletion are not very clear. It could be because of its lower deposition rate compared to Fe and Cr. Ni content varied significantly displaying as low as about 2 wt.% (with Cr content of about 30 wt.% in the same location). However, such variations are much localized. The localized Ni depletion could indirectly cause more Fe/Cr interactions and hence the formation of sigma phase. In fact, if the Ni content were to be zero, Fe and Cr would have highest chance for interaction during deposition, which favors the formation of sigma phase. In reality, even if the Ni content is not zero, but much less than the actual 8 wt.%, it could create a similar situation locally, ultimately causing sigma phase formation in that region.

Even if there is higher Cr and lower Ni, temperature is a primary factor in the formation of sigma phase. Higher temperatures are generally required to observe this tetragonal phase. One of the ways to understand its formation is to assume that the high temperature phase gets stabilized at lower temperatures during vapor deposition processes. If this were to be true, sigma phase must have been observed by earlier researchers [1-10] who deposited SS304 by vapor deposition. But none of the vapor deposition studies on SS304 reported the sigma phase formation. Therefore, the argument that stabilization of high temperature phase occurs at lower temperatures, cannot be applied here. Two possible causes for the sigma phase formation have been studied here. One of them is nanocrystalline grain size and the second is strain.

5.3.2.3. Grain Size

The fact that grain boundaries are nucleation sites has long been known. Since smaller grains have more grain boundary area per unit volume, they can act as nucleation sites for precipitation. The average grain size of ferrite phase in the SS304 sputter-deposited coating is 96 nm, which is in the nanocrystalline regime. The grain size is significantly lower than conventionally solidified steels that have few microns of grain size. Hence the free energy rise resulting from grain size reduction could be the cause for the formation of sigma phase. However, in magnetron sputtered SS304, the grain size obtained by Barbee et al. [3] was about 40 nm, is much smaller than that observed in the present study, but no sigma phase was reported. Also, Idiri et al. [22] did not observe sigma phase formation in their ion beam sputtered 304 L steel, even though the grain size was about 10 nm (obtained by XRD). Hence, the argument that smaller grain size is a reason for the formation of sigma phase is not applicable.

5.3.2.4. Strain

Other than sputter-deposition, formation of sigma phase was noticed in austenitic steels during heat treatment at or near recrystallization temperatures [16-18]. However, the kinetics of formation of sigma phase were slow. From the literature study, it is noticed that the strain relief during heat treatment is causing the sigma phase formation rapidly. For instance, accelerated formation of sigma phase after tensile test and subsequent heat treatment was noticed in a nominal composition 20Cr-11Ni stainless steel [23]. In a different study, it was observed that formation of the sigma phase was significantly accelerated by strain in 308 stainless steels during aging which was performed between 550 and 850 °C for times up to 10000 h [17]. Additionally, Ameyama et al. [24] have reported that ferrite rapidly decomposed to sigma in ultrafine microduplex (ferrite and austenite) microstructure produced by the high strain powder metallurgy process during sintering of 316 austenitic stainless steel. Strain as a possible reason for rapid formation of sigma phase in SS304 during friction stir welding was also reported [25]. These results suggest that high strain and the subsequent thermal treatment can lead to the rapid formation of sigma phase by the process of strain relief. In order to estimate the strain present in the coating, the Williamson-Hall (W-H) approach was used [26-27].

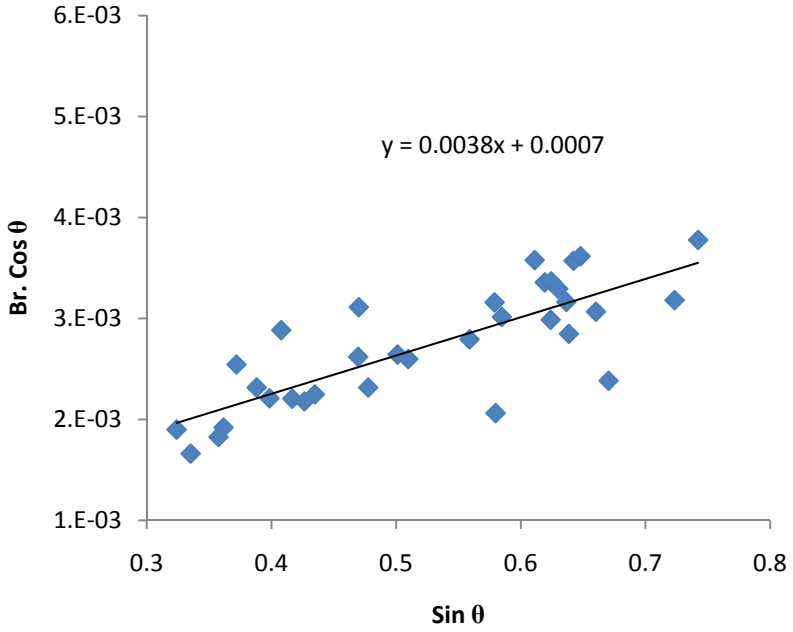

Figure 5.8: Williamson-Hall plots of sigma phase derived from the XRD pattern of SS304.

W-H approach has been traditionally used to distinguish and estimate the magnitudes of the peak broadening by strain and crystallite size of polycrystalline materials. Figure 5.8 shows the W-H plot for sigma phase. The strain in the sigma phase was calculated from slope of W-H plot which was found out to be 0.38% which is very less. Assuming there was prior strain during vapor deposition, a strain relief mechanism could have operated in the present case of SS304 coating. One of the possibilities of strain relief is through the nanoporosity, which could locally relieve the strain during deposition, causing sigma phase formation.

5.4. Conclusions

Metastable phases, ferrite and sigma, were observed in sputter-deposited SS304 steel. Both are non-equilibrium phases as austenite is the equilibrium phase. Ferrite formation is either because of Ni depletion leading to austenite destabilization. Coating showed significantly higher Cr and lower Ni than the average contents of 18Cr-8Ni steel (SS304). Such changes could promote sigma phase formation. Strain is another parameter that could influence the non-equilibrium sigma phase formation.

5.5. References

1. S.D. Dahlgren, E.D. McClanahan, J.W. Johnston, and A.G. Graybeal, Microstructure of sputter-deposited 304L stainless steel, Journal of Vacuum Science and Technology, 7 (1970), p.398
2. S.D. Dahlgren, Equilibrium phases in 304L stainless steel obtained by sputter-deposition, Metallurgical Transactions, 1 (1970), p.3095
3. T.W. Barbee, B.E. Jacobson, and D.L. Keith, Microstructure of mmorphous 304 stainless steel-carbon alloys synthesized by magnetron sputter deposition, Thin Solid Films, 63 (1979),
4. J. Childress, S.H. Liou, and C.L. Chien, Ferromagnetism in metastable 304 stainless steel with bcc structure, Journal of Applied Physics, 64 (1988), p.6059
5. M.J. Godbole, A.J. Pedraza, L.F. Allard, and G. Geesey, Characterization of sputter-deposited 316L stainless steel films, Journal of Materials Science, 27 (1992), p.5585
6. F.S. Li, J.J. Sun, and C.L. Chien, ^{57}Fe Moessbauer study of metastable 304 stainless steel film with BCC structure, Journal of Physics Condensed Matter, 7 (1995), p.1921
7. J.P. Eymery, N. Merakeb, P. Goudeau, A. Fnidiki, and B. Bouzabata, A Mössbauer comparative study of the local environment in metastable 304 stainless steel films depending on the preparation mode, Journal of Magnetism and Magnetic Materials, 256 (2003), p.227

8. X. Zhang, A. Misra, R.K. Schulze, C.J. Wetteland, H. Wang, and M. Nastasi, Critical factors that determine face-centered cubic to body-centered cubic phase transformation in sputter-deposited austenitic stainless steel films, Journal of Materials Research, 19 (2004), p.1696
9. S. Cusenza, C. Borchers, E. Carpene, and P. Schaaf, The Gibbs-Thomson effect in magnetron-sputtered austenitic stainless steel films, Journal of Physics, Condensed Matter, 19 (2007), p.106211
10. S. Inoue, T. Saeki, H. Uchida, K. Koterazawa, and M. Iwasa, Effects of ion flux on the properties of dc magnetron-sputtered stainless steel films, Vacuum, 66 (2002), p.257
11. T.F. Kelly, M. Cohen, and J.B. Vander Sande, Rapid solidification of a droplet-processed stainless steel, Metallurgical and Materials Transactions A, 15 (1984), p.819
12. R. Wright, J. Flinn, G. Korth, J. Bae, and T. Kelly, The microstructure and phase relationships in rapidly solidified type 304 stainless steel powders, Metallurgical and Materials Transactions A, 19 (1988), p.2399
13. J.M. Vitek, A. Dasgupta, and S.A. David, Microstructural modification of austenitic stainless steels by rapid solidification, Metallurgical and Materials Transactions A, 14 (1983), p.1833
14. H. Huang, J. Ding, and P.G. McCormick, Microstructural evolution of 304 stainless steel during mechanical milling, Materials Science and Engineering A, 216 (1996), p.178
15. N. Yukawa, M. Hida, T. Imura, Y. Mizuno, and M. Kawamura, Structure of chromium-rich Cr-Ni, Cr-Fe, Cr-Co, and Cr-Ni-Fe alloy particles made by evaporation in argon, Metallurgical Transactions B, 3 (1972), p.887
16. J. Barcik, Mechanism of σ-phase precipitation in Cr-Ni austenitic steels, Materials Science and Technology, 4 (1988), p.5
17. J.M. Vitek, S.A. David, W.H. Smith, and R.W. Reed, *Solidification and Aging Behavior of Types 308 and 308 CRE Stainless Steel Welds*. (Report) 1984, ORNL/TM-9086, Oak Ridge National Lab., TN (USA).
18. Y. Minami, H. Kimura, and Y. Ihara, Microstructural changes in austenitic stainless steels during long-term aging, Materials Science and Technology, 2 (1986), p.795
19. J.M. Joubert, Crystal chemistry and Calphad modeling of the sigma phase, Progress in Materials Science, 53 (2008), p.528
20. H. Baker, Alloy Phase Diagrams (1992), ASM International, Materials Park, Ohio.

21. Y.-Y. Chuang and Y. Chang, A thermodynamic analysis and calculation of the Fe-Ni-Cr phase diagram, Metallurgical and Materials Transactions A, 18 (1987), p.733
22. M. Idiri, B. Boubeker, R. Sabot, P. Goudeau, J.F. Dinhut, and J.L. Grosseau-Poussard, Structure and related corrosion behaviour in 1M H2SO4 of b.c.c. 304L films prepared by ion beam sputtering, Surface and Coatings Technology, 122 (1999), p.230
23. E.E. Levin, E.M. Pivnik, and P.M. Libman, The effect of sigma phase on the mechanical properties of heat resistant steels, Metal Science and Heat Treatment, 1 (1959), p.19
24. K. Ameyama, M. Hiromitsu, and N. Imai, Tetsu-to-Hogane, 84 (1998), p.357
25. S.H.C. Park, Y.S. Sato, H. Kokawa, K. Okamoto, S. Hirano, and M. Inagaki, Rapid formation of the sigma phase in 304 stainless steel during friction stir welding, Scripta Materialia, 49 (2003), p.1175
26. B.D. Cullity and S.R. Stock, Elements of X-ray Diffraction (1990), 2nd. ed., Addison-Wesley Publishing Company, Massachusetts, USA.
27. C. Suryanarayana and M.G. Norton, X-Ray Diffraction: A Practical Approach (1998), Plenum Press, New York.

CHAPTER 6: MICROSTRUCTURAL CHARACTERIZATION OF SPUTTER-DEPOSITED 304 STAINLESS STEEL-10 Wt.% Al COATINGS

6.1. Introduction

In the previous chapters, grain size, phase evolution and microstructure of different SS304+Al coatings were studied. The objective of the present chapter is to provide details of microstructure of the SS304+10 wt.% Al (17 at.% Al) coating. The characterization techniques XRD, TEM and 3DAP coupled with field ion microscope (FIM) were used. 3DAP is a useful tool in microstructural characterization of materials at nanoscale [1].

6.2. Results

Results are divided into three separate sections, namely x-ray diffraction, transmission electron microscopy and three-dimensional atom probe.

6.2.1. X-ray Diffraction

Figure 6.1 shows the XRD pattern of SS304+10Al sample. Five peaks are observed and are indexed in the pattern. Based on their *d*-spacings and indexing, the phase is identified as B2. Only one superlattice peak of B2 phase (at 2θ of about 31° - (100) peak), is present in XRD pattern but all other superlattice peaks are absent (or too weak to be observed) in the range from 20-100°. Another observation is that the most intense peak in the pattern is (200), whereas the (110) peak is expected to be the most intense in B2. This indicates that there is preferred orientation in the (200) of the coating.

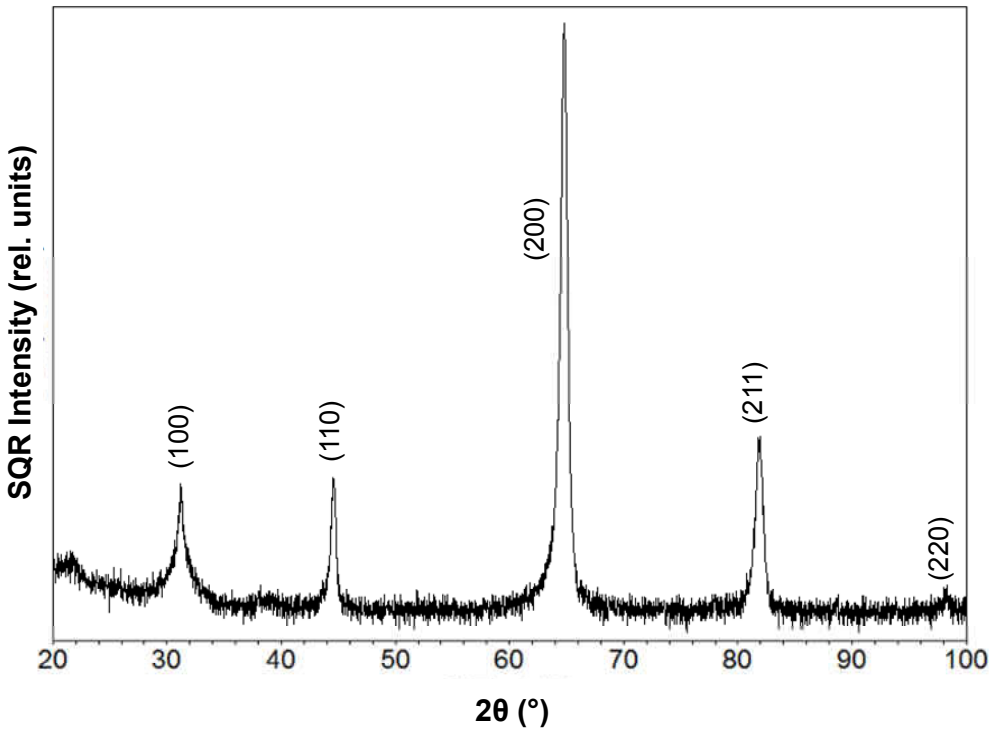

Figure 6.1: XRD pattern of SS304+10Al coating; Indexing shows the presence of B2 phase

6.2.2. Transmission Electron Microscopy

TEM samples were studied in two orientations (i) cross-section view and (ii) in-plane view.

6.2.2.1. Overall Microstructure of Cross-Section TEM Sample

As described in the grain size chapter, columnar grains of the size range from 130 nm to about 3 μm were observed in SS304+10Al coating. Figure 6.2 shows the typical BF micrographs from the sample.

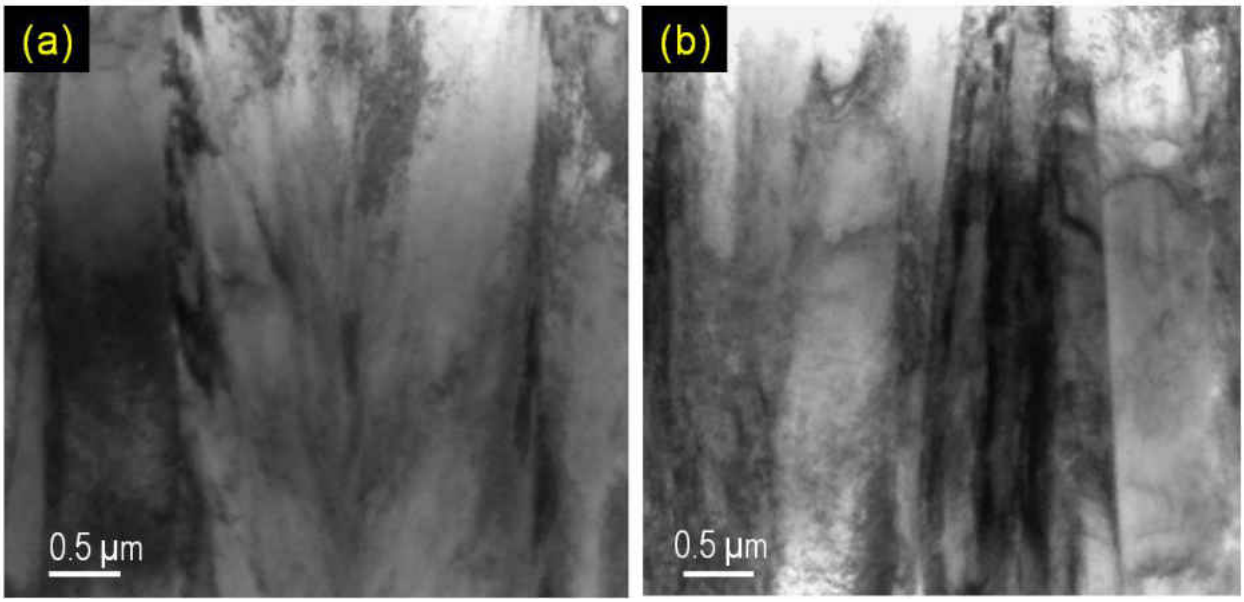

Figure 6.2: Typical BF micrographs from SS304+10Al sample showing the columnar grains of about 1 μm average grain size

6.2.2.1.1. Layered Structure

An important observation in the microstructure at high magnifications of the coating is the presence of layered structure. Figure 6.3(a) shows the uniformly distributed layered structure in the cross-section sample. Two types of layers, bright and grey in contrast, were observed. The layers were parallel to the deposition surface. Columnar grains were filled with the stacks of these layers. The spacing between a set of the layers was about 3.2 nm. In order to explore the layered structure further, HRTEM and nano beam diffraction (NBD) were carried out which are shown in Figure 6.3(b). From the combined HRTEM and NBD study, it was assessed that the layers were chemically and crystallographically similar. Any difference that is present is minor. Consequently, 3DAP was performed on this coating to study these multilayers for their detailed chemistry and elemental distribution.

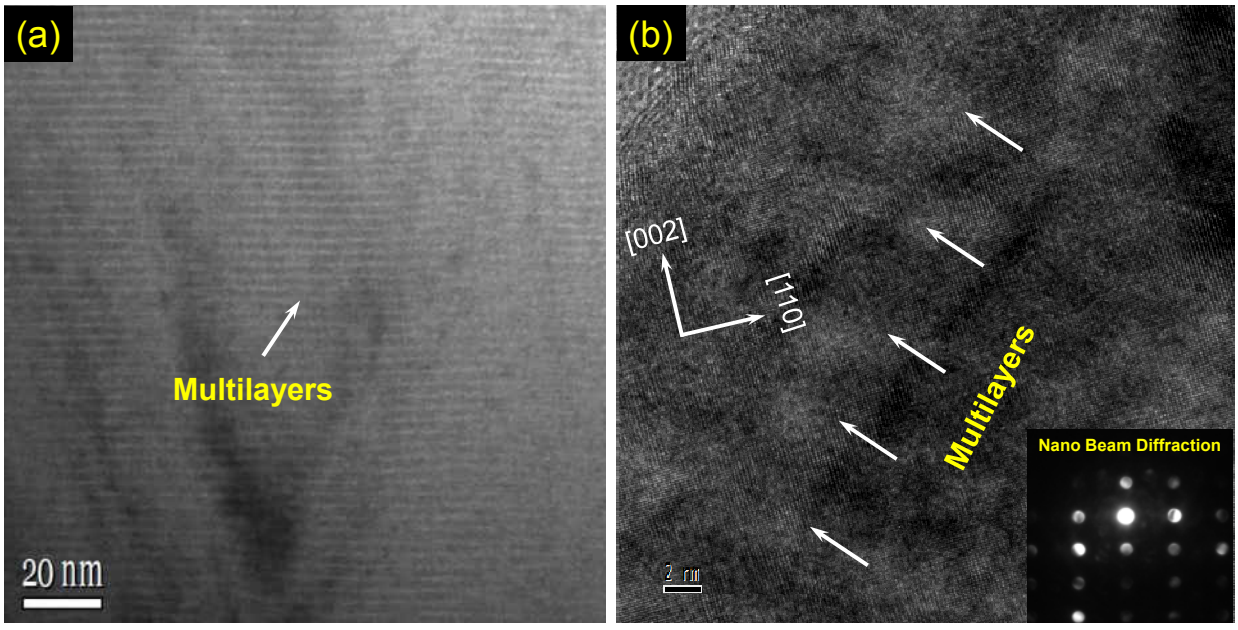

Figure 6.3: TEM micrographs showing the layered structure, (a) BF and (b) high resolution micrograph hardly showing any contrast between the layers; inset shows the NBD

6.2.2.2. Overall Microstructure of In-Plane TEM Sample

Figure 6.4 shows TEM BF microstructures in the planar view. Particular advantage with the in-plane sample was that the whole range of grain size (from minimum 130 nm to maximum up to about 3 μm) could be observed. The layered structure was not observed in the in-plane samples. If the layers are formed due to deposition, obviously they are normal to the electron beam and cannot be seen in the in-plane sample. Thus it appears that the layers were formed during deposition.

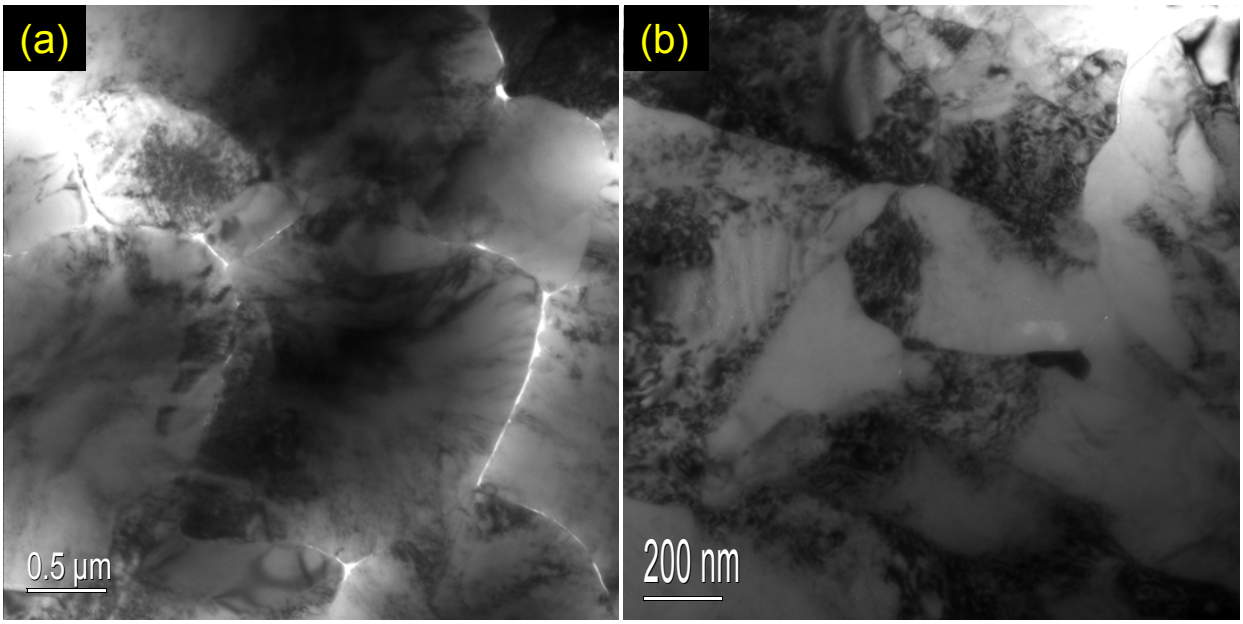

Figure 6.4: In-plane view of the SS304+10Al sample at different magnifications. The porous regions in (a) are a result of preferential removal of material at the grain boundaries during ion milling

6.2.2.3. B2 Phase in Cross-Section TEM Sample

The distribution of B2 phase was studied in cross-section sample. Figure 6.5 shows the BF, DF and DP in [001] zone axis. The DF was recorded from superlattice (100) spot of the SADP which represents the B2 phase. From the microstructure, it can be assessed that the B2 phase exists as broad domains up to about 10 nm in size. Randomly oriented nanoparticles cause rings in electron diffraction pattern. However, ring pattern was not seen in the present case. Instead, a single crystal DP was observed as shown in inset of Figure 6.5(b). This is possible only when there is an orientation relationship between B2 and ferrite.

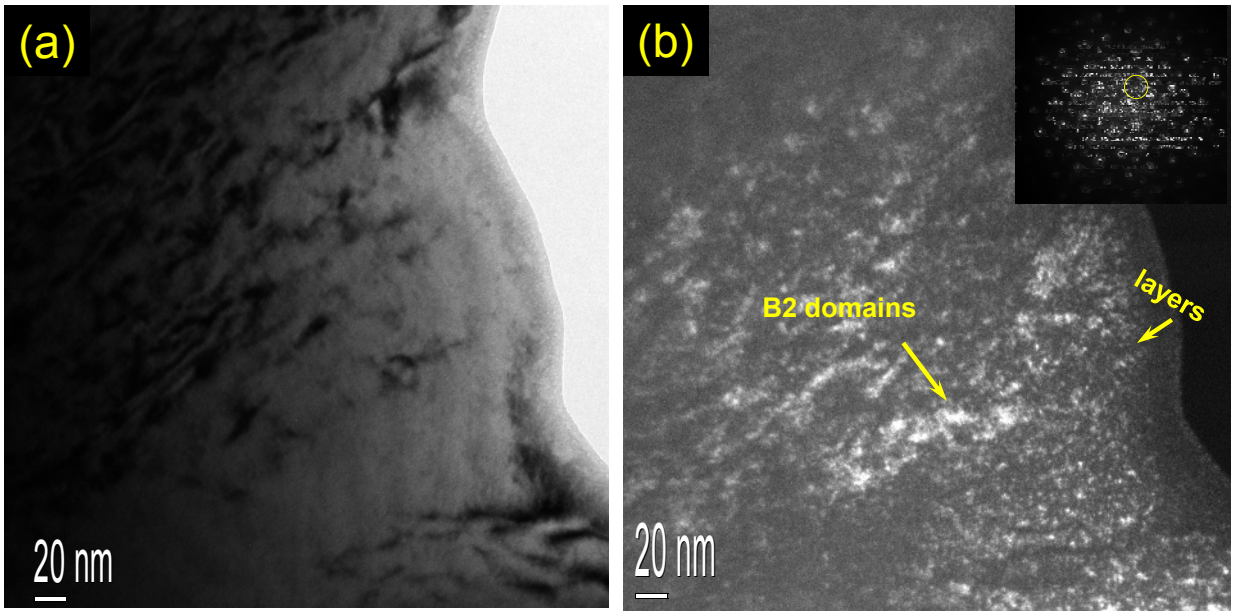

Figure 6.5: (a) BF TEM micrograph of region at high magnification obtained from using [001] beam (b) DF from (100) superlattice spot; the DF clearly shows the B2 phase in the form of clusters and layers with a spacing of about 3.2 nm

As can be noticed from Figure 6.5(b), the distribution of B2 phase (contrast of brighter areas) is uneven. This indicates that there are two phases present in the microstructure. While the bright domains are B2 phase, the grey area is ferrite phase.

From careful observation of the DF microstructure, decoration of B2 phase along near the edges or very thin areas of the sample in the form of lines was noticed (Figure 6.5(b)). Figure 6.6 is another DF which shows the layered structure. The lines match up with the layered structure as the spacing between them is about 3 nm. Hence, it was inferred that there is some relation between the B2 phase and the layered structure. To be precise, layered structure consists of B2 phase. The other layer could be inferred as ferrite.

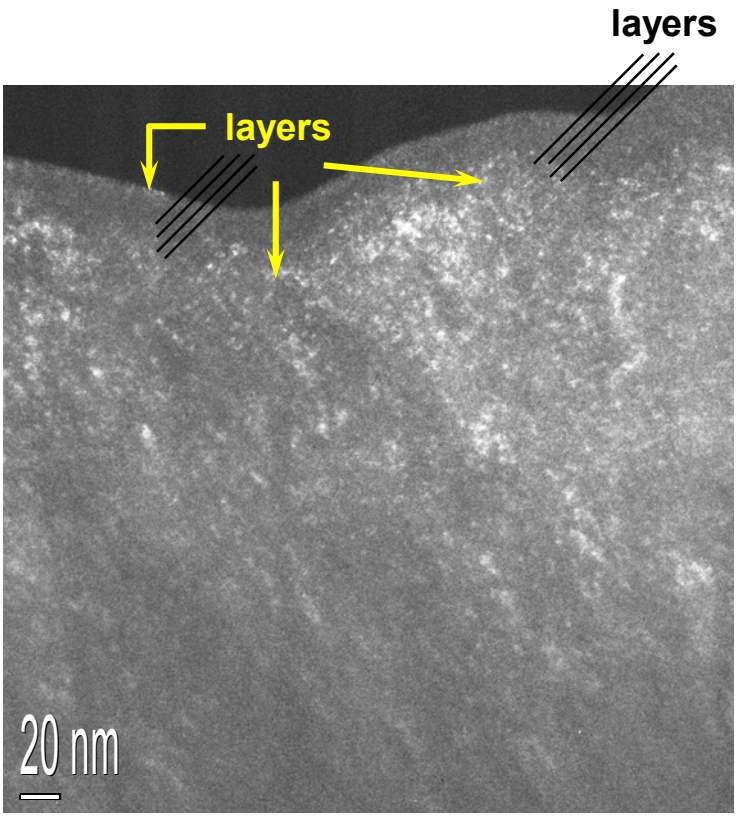

Figure 6.6: Decoration of layers in dark field micrograph taken from (100) superlattice spot of [001] zone axis; the layered structure may be seen near the edge of the sample

6.2.2.4. B2 Phase in In-Plane TEM Sample

Figure 6.7 shows the BF, DF and SAD pattern for the in-plane sample. The DF in Figure 6.7 was taken using (100) superlattice spot near the transmitted beam. It was found from the DF that the B2 phase was in the form of nano clusters of up to 5 nm in size and occupied most of the area in the microstructure.

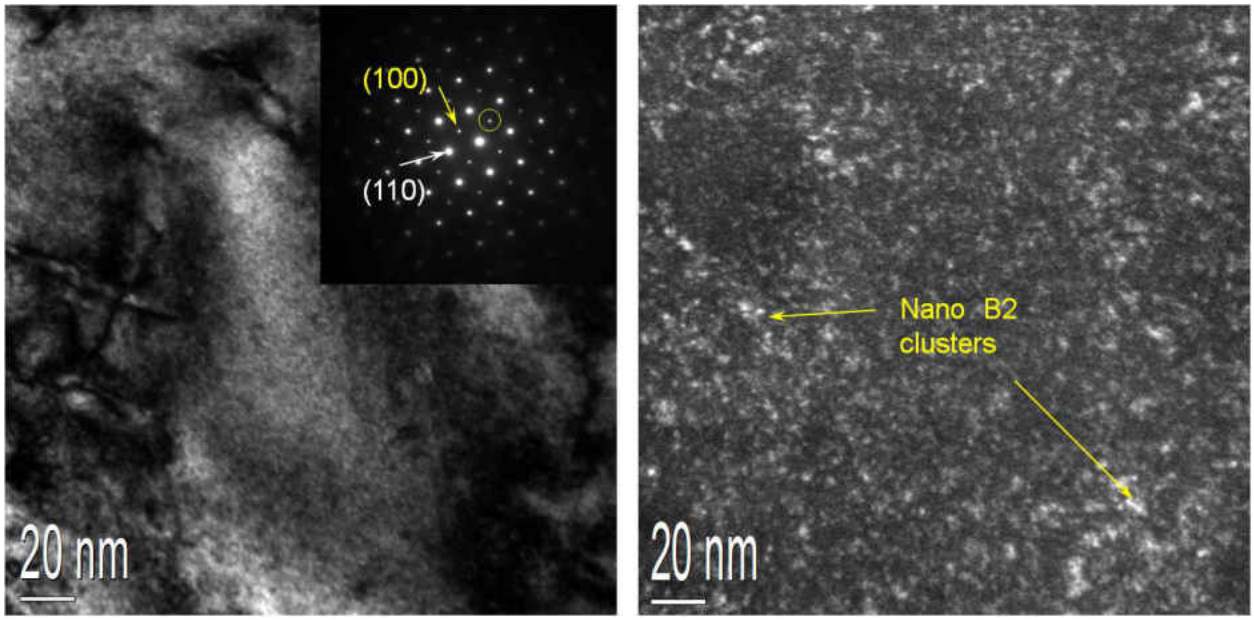

Figure 6.7: BF, DF and SADP from [001] zone axis. The DF clearly shows the presence of clusters of nano B2

6.2.2.5. B2 Phase in High Resolution TEM (HRTEM)

HRTEM was performed in order to characterize the B2 phase. Figure 6.8(a) shows a high resolution TEM micrograph in-plane SS304+10Al sample taken from [001] zone axis. Two neighboring regions of the micrograph were highlighted with square boxes and the corresponding Live Fast Fourier Transform patterns (FFTs) are shown in Figure 6.8(b) and Figure 6.8(c). The difference between the two FFT patterns was the presence of superlattice spots. While the area corresponding to the FFT pattern in Figure 6.8(b) which has superlattice

spots is the B2 phase, the area corresponding to the Figure 6.8(c) belongs to ferrite since there are only fundamental spots in FFT pattern. Despite the difference in FFT patterns of B2 and ferrite phases, no lattice mismatch was observed between the two in HRTEM. Therefore, it is completely logical to conclude that there is coherency between B2 and ferrite. This result is in agreement with the SADP results on coherency between the two phases.

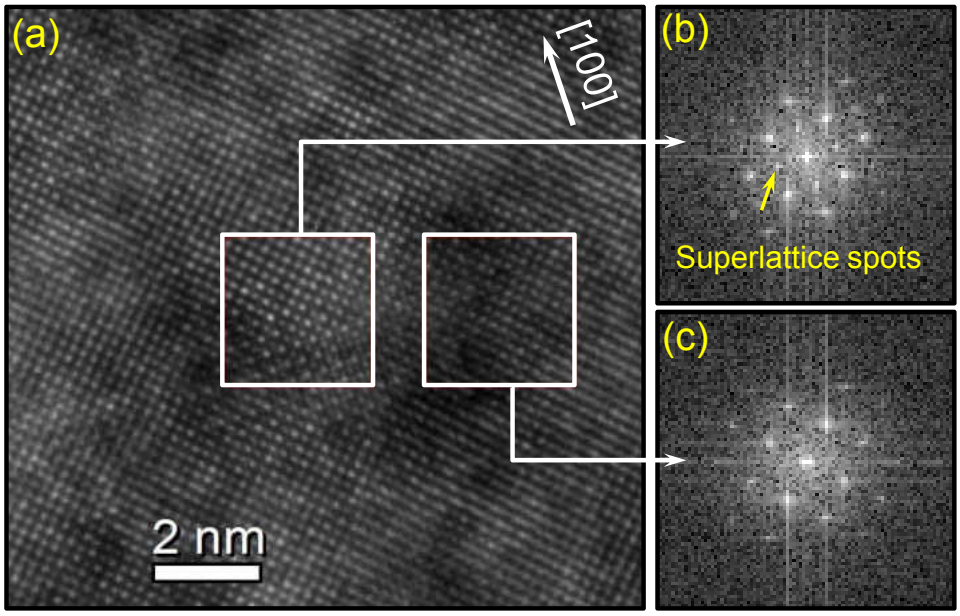

Figure 6.8: (a) HRTEM micrograph from an in-plane sample of SS304+10Al coating containing both bcc and B2 phases. From Live FFT analysis, it was found that the left box was B2 phase (b) and right box was bcc phase (c)

6.2.3. Three-Dimensional Atom Probe (3DAP)

3DAP is a very useful tool for obtaining chemical and morphological information from extremely small length scales [2]. The nanometer layered structure and B2 phase observed were studied by the 3DAP technique. The objective was to identify the origin for the layered structure formation and to identify the distribution of B2 phase.

6.2.3.1. Acquisition of Data from 3DAP Needle Sample

Figure 6.9 shows the mass spectrum that is resulted from the 3DAP acquisition. Mass-to-charge ratio (related to the atomic number and isotopes of the elements present) is shown on x-axis while a factor corresponding to relative abundance of ions (of elements present) is shown on y-axis. Mass resolution was 0.01 atomic mass units with sub-nanometer spatial resolution.

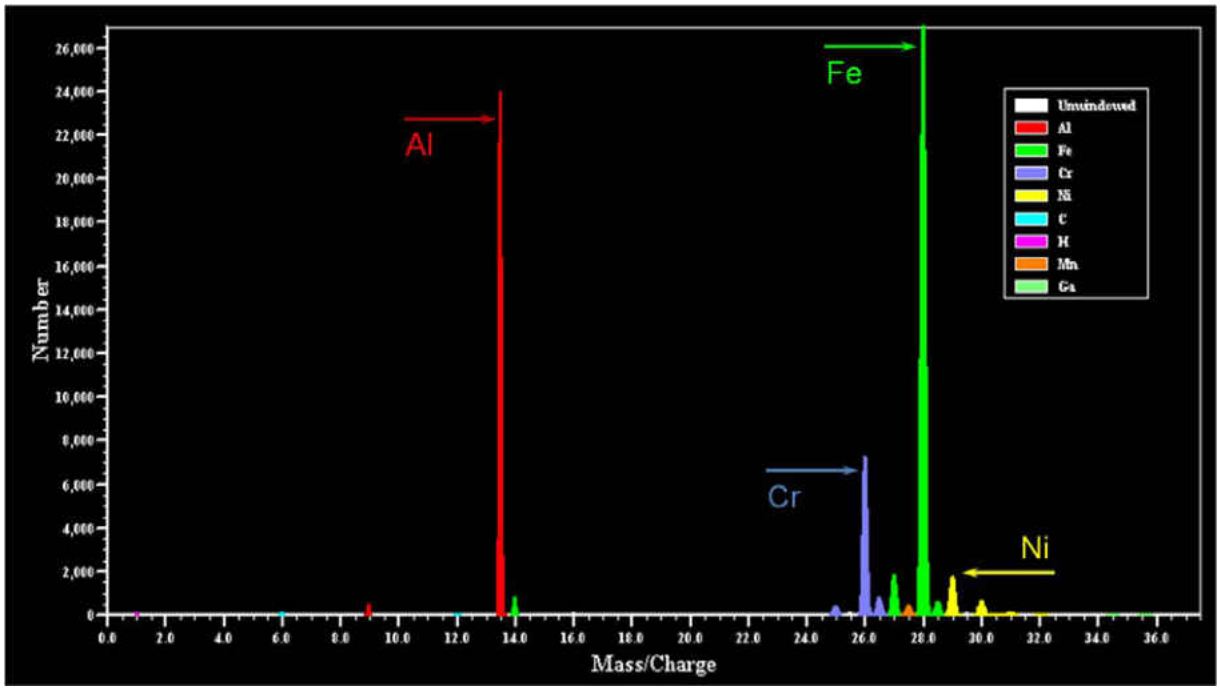

Figure 6.9: Mass spectrum from SS304+10Al 3DAP sample

6.2.3.2. Selection of Elements

From the mass spectrum, the elements identified were Fe, Cr, Ni, Al, Mn, C, Ga and H. Only the major elements were studied for any useful data analysis. Trace elements were ignored as they did not seem to affect the chemistry. For example, Mn and C were distributed uniformly with no effect on composition. Ga is generally embedded in the sample during FIB (Focused Ion Beam) sample preparation. The relative quantity of Ga is quite low and negligible as we move away from the tip of the needle. We studied an area far from the tip of the needle in order to avoid any conflict. The atoms that were considered for analysis are basically Fe (the solvent element), Al (the main solute element), Cr and Ni. Figure 6.10 shows the reconstructed maps of only Fe, Al and Ga from the overall acquisition of needle.

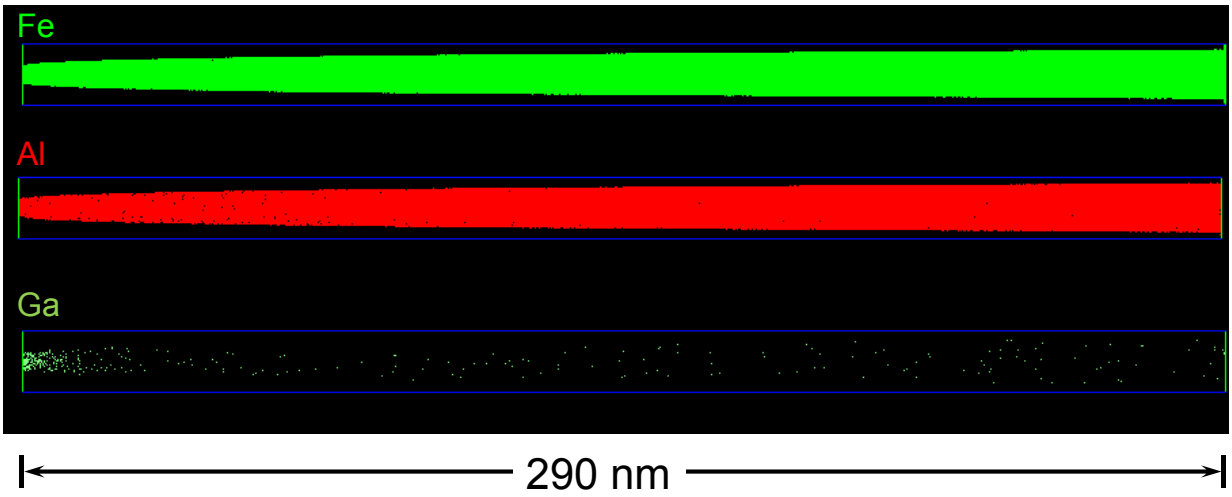

Figure 6.10: Reconstructed atom maps of entire needle; 3 elements Fe, Al and Ga are shown in atom maps. Fe is the element with maximum quantity (solvent), Al is the element of interest and Ga contamination

6.2.3.3. Selected Area Analysis

Figure 6.11(a) shows the 3-D atom reconstruction map of Al. In order to study the atomic density distribution and concentration profiles, a portion of the sample away from the needle tip was chosen. The chosen volume of 64x11x13 nm is shown in Figure 6.11(b). A further smaller volume was selected from Figure 6.11(b) which is shown in Figure 6.11(c). Important point to notice here is the difference in the density of atoms along the length of the needle.

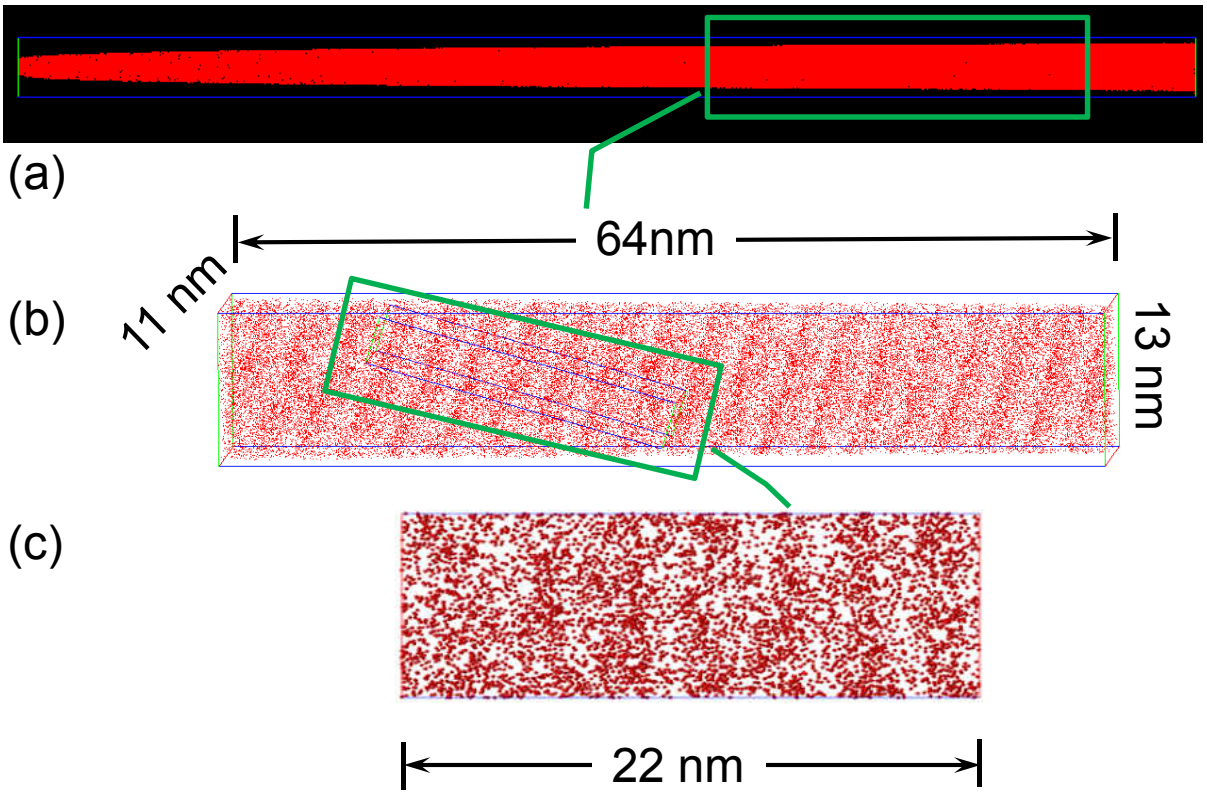

Figure 6.11: (a) Reconstructed 3DAP map of only Al atoms (b) layered structure in a volume of 64 nm x 13 nm x 11 nm of the needle (c) Further smaller volume shown in 2D of length 22 nm x 5 nm

Reconstructed 3DAP map of selected elements is shown in Figure 6.12. The difference in the density of atoms exists in all the elements. Figure 6.12(a) shows Al atoms in red color (appears grey in black and white print) and Ni in yellow color (appears as white color in black and white print). It is evident that Ni atoms are distributed along the Al enriched layers.

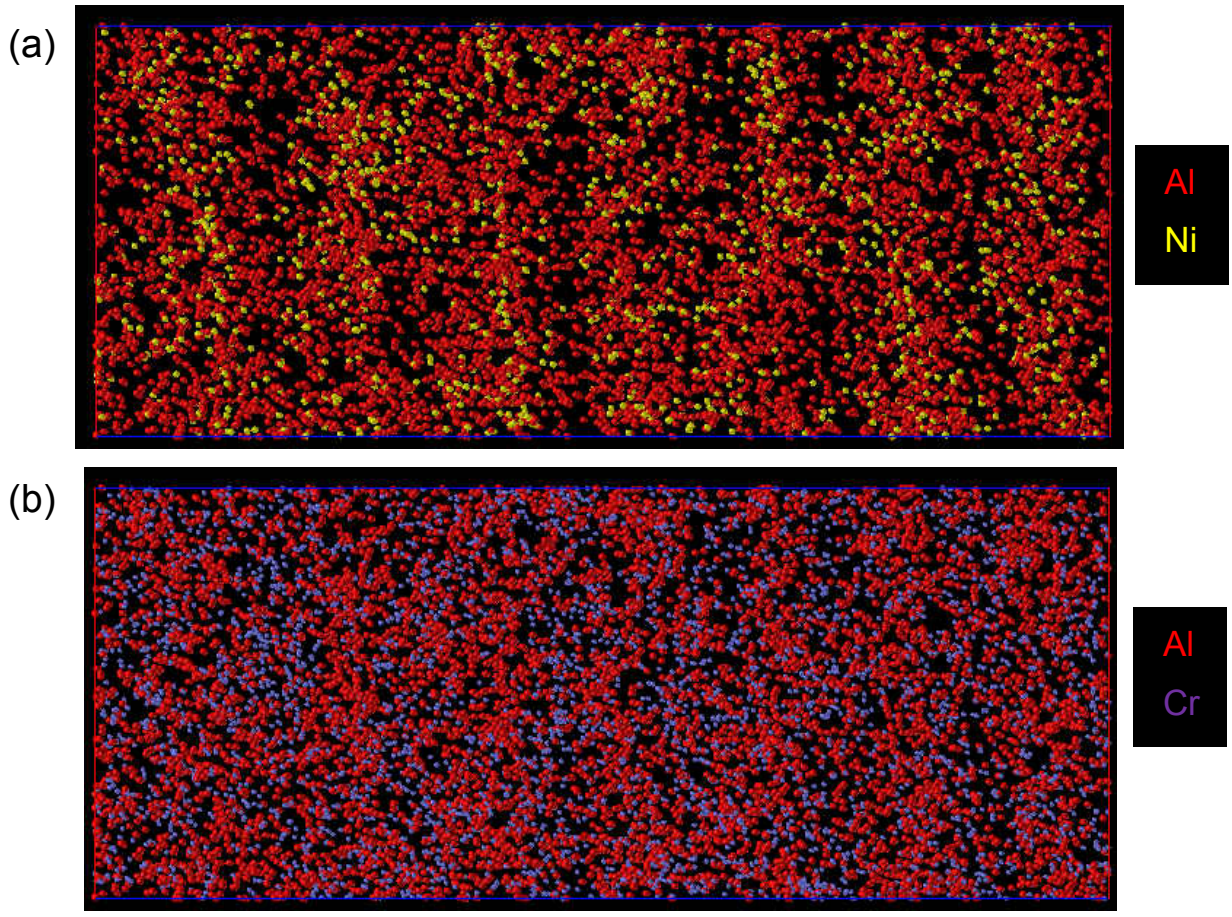

Figure 6.12: Reconstructed 3DAP map of selected elements (a) Distribution of Al and Ni atoms in the 22 nm x 5 nm area (b) distribution of Al and Cr atoms in the same area. While the relative density of Ni atoms is more in Al enriched layers, relative density of Cr atoms is less in the Al enriched layers

The composition profile of all the elements gives full details of their distribution. Figure 6.13 is the profile of Fe, Cr, Ni and Al atoms along the 22 nm selected region.

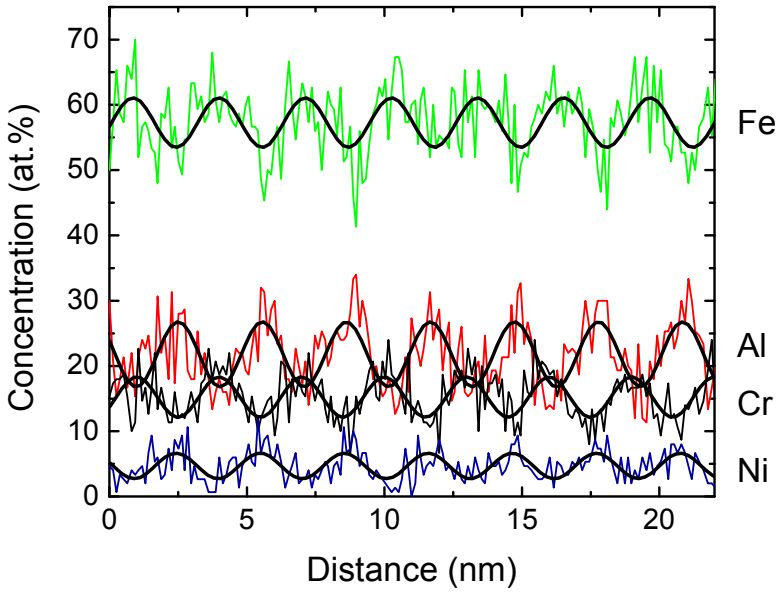

Figure 6.13: Composition profile of the layers in selected area of SS304+10Al sample; it takes about 10 seconds to deposit the 22 nm thick layered structure

The composition fluctuations in the layers could be fitted to sine function of the type

$$At.\%\, M = M_{avg} + A\, sin\left(\frac{2\pi m}{\lambda} \pm \emptyset\right)$$

where M is Metal, M_{avg} is average metal content in any layer, A is the amplitude of compositional variation of the metal, λ is the wavelength of the compositional fluctuations, Φ is the factor deciding the phase difference and *m* is the abscissa indicating the spatial distance in nm. Figure 6.13 also shows the sine wave fitting.

It is observed from the Figure 6.13 that the composition profiles of Fe and Cr are in-phase, and that Al and Ni are in-phase. In other words, Fe and Cr enriched layers are depleted in Al and Ni whereas Fe and Cr diminished layers are enriched in Al and Ni.

The resultant fitting equations are,

$$At.\%\ Fe = 57.3 + 3.8\ sin\ \left(\frac{m-0.1}{1.6}.\pi\right)$$

$$At.\%\ Cr = 15.2 + 3.1\ \sin\ \left(\frac{\mathrm{m}-0.2}{1.5}.\pi\right)$$

$$At.\%\ Ni = \ 4.7 + 2.0\ \sin\ \left(\frac{\mathrm{m}-1.7}{1.5}.\pi\right)$$

$$At.\%\ Al = 21.8 + 5.0\ \sin\ \left(\frac{\mathrm{m}-1.7}{1.5}.\pi\right)$$

The average concentrations of Fe, Cr, Ni and Al in atomic percentages were 57.3, 15.2, 4.7 and 21.8, respectively. The same in wt.% were, 65.4, 16.1, 5.6, and 12.0% respectively. The layered structure was mainly Fe-rich with a minimum of 45 at.% Fe in any layer. For further discussions, it is convenient to label the alternative layers as Fe_{Max} and Fe_{Min} depending on the Fe concentrations. Fe_{Max} is the layer with maximum Fe content (Fe enriched layer) where as Fe_{Min} is the layer with minimum Fe content (Al enriched layer). Fe_{Max} layer contained more Fe, Cr, and less Ni, Al than average; Fe_{Min} layer contained less Fe, Cr and more Ni, Al than average.

6.3. Discussion

It was shown in chapter 4 with the help of ternary Fe-Ni-Al phase diagram, that the phases present in SS304+10Al coating are B2 and ferrite. This is in agreement with the phases that have been observed experimentally by XRD and TEM. Further to the phases, two major features from the results section of this chapter deserve special attention. One of them is layered structure and the second is B2 phase distribution. The issues with layered structure are finding its origin and finding how these layers have formed. On the other hand, the focus on B2 phase is to identify if it is FeAl or NiAl.

6.3.1. Origin of Layered Structure

Since the deposition was done using two targets and the substrate was rotated, a layered structure could have resulted from the deposition process. If that were to be the case, the layer dimensions can be estimated from experimental conditions. Accounting for substrate rotation, the wavelength (spacing between two alternative layers) was calculated from the coating thickness to be 4.4 nm. On the other hand, the observed wavelength in TEM is 3.2 nm. The small difference in the calculated and observed layer wavelengths can be attributed to the variation in thickness of SS304+10Al coating from which the wavelength has been calculated. It is thus concluded that the layered structure was induced by deposition and not by any other means. One interesting point here is, the calculated wavelength in 4Al and 7Al coatings is 3.1 nm which is close to the observed wavelength of 3.2 nm in 10Al coating.

6.3.2. Distribution of Fe, Cr, Ni and Al in the Layers

Assuming no chemical interactions among atoms, deposition with two targets SS304 and Al should induce two layers (i) a layer that is enriched in Fe, Cr and Ni, and (ii) a layer that is enriched in Al as shown in the schematic Figure 6.14(a). In other words, the composition profiles of Fe, Cr and Ni in layers should be in-phase, exhibiting almost 90° phase difference with that of Al enriched layer. However, the observation is different. Fe, Cr and Ni profiles all are not in-phase; Ni is out-of phase. Ni joined Al enriched layer making Ni and Al profiles in-phase as shown in Figure 6.14(b).

Figure 6.14: Description of layered structure (a) anticipated layered structure as a result of deposition from SS304 and Al targets (b) Obtained layered structure with Ni taken away by Al enriched layer.

In summary, Al and Ni are enriched in zones where Fe and Cr are diminished, whereas Al and Ni are depleted in zones where Fe and Cr are enriched. Very similar behavior was observed by Guo et al. [3] in precipitates of PH13-8 steel aged at 510 °C for 40 min to 4 h. It was observed that NiAl precipitates had grown bigger in size up to about 10 nm with aging time of 4 h. In another atom probe microanalysis study of Fe-20Cr-2Ni-2Al (at.%) alloy [4], it was found that the composition of the B2 intermetallic phase was close to the stoichiometric composition

NiAl with only a limited amount of dissolved iron. In a different report, comparative study on medium carbon secondary hardening steel and PH13-8 steel, (both steels containing Ni and Al), Erlach et al. [5] found that NiAl phase was the one to precipitate at nano scale during aging treatment at 610 °C. This indicates that at nano scale Ni atom prefers Al atom as neighbor and vice versa. The above studies together with current observation strongly suggest that the early stage precipitation in Ni-containing steels is indeed NiAl and not FeAl. This behavior can be explained on the basis of heat of mixing that is described in the following section.

6.3.3. Effect of Heat of Mixing

Heat of mixing (ΔH^{Mix}) between atoms decides the nearest atomic neighbor. Negative ΔH^{Mix} between any two elements keeps them attracted to each other and hence favors solution, whereas positive ΔH^{Mix} causes separation (precipitation). The preference of Ni for Al can be understood based on the heat of mixing between Fe, Ni and Al. Table 6.1 shows the average ΔH^{Mix} values obtained from de Boer et al. [6].

Table 6.1: Heat of mixing among the elements Fe, Cr, Ni and Al in kJ/mole at 50-50 compositions [6]

	Fe	Cr	Ni	Al
Fe	-	5.9	-3.9	-26.0
Cr	5.9	-	6.4	*
Ni	-3.9	6.4	-	-71.0
Al	-26.0	*	-71.0	-

* not available at 50-50 composition of Cr and Al. For $CrAl_7$, the value at 298 K is -13.

The ΔH^{Mix} of Fe and Al, is -26 kJ/mole while that of Ni and Al is -71 kJ/mole. Since the ΔH^{Mix} is more negative with Ni, Al prefers Ni as neighbor to Fe. That was how Ni was pulled to Al enriched layer during deposition. As seen from Figure 6.13, Ni content in Fe enriched layer (Fe_{Max}) is often close to zero whereas Ni is highest in Al enriched layer (Fe_{Min}). Therefore, the B2 phase at this scale is judged as NiAl. It is timely to recall the observation of B2 phase in the layers with a spacing of about 3 nm in TEM DF studies. The B2 phase is nothing but NiAl.

6.3.4. Phase in Fe-enriched Layer

As seen earlier, Al enriched layer has Ni enrichment which form the NiAl. However the next layer was enriched in Fe and diminished in Al. Typical composition of the layer in at.% is 65Fe-18Cr-15Al-3Ni. This composition can have ferrite and B2 phases. This B2 is different from the B2 phase in the Al enriched layer. The B2 within the ferrite layer could be mostly FeAl whereas the B2 in the Al enriched layer is NiAl. The average quantity of Ni in the coating is 4.7 at.% (about 5.6 wt.%). To form stoichiometric NiAl, the atomic percentage of Al required is then just 4.7 at.%. Since Al has strong preference for Ni as neighbor, Al joins Ni to form NiAl. But the quantity of Al (21.8 at.%) is much more than 4.7 at.%. Therefore, plenty of Al is left even after forming NiAl. Once the Ni is consumed up, the remaining Al either forms Fe solid solution (ferrite) or FeAl (B2). On the whole it can be rationalized that Al has preference to form NiAl first and then FeAl in Al added steels.

6.4. Conclusions

SS304+10Al alloy was deposited by two target sputter-deposition and was characterized by XRD, TEM and 3DAP techniques. Ferrite and B2 phases were present in the coatings. There

was also layered structure that is a result of the dual-target deposition. The layers were either enriched or diminished in Fe, Cr, Ni and Al contents. The Fe enriched layers were depleted in Al content while the Fe diminished layers were enriched in Al content. Also, Fe and Cr composition profiles were in-phase; while Al and Ni profiles were also in-phase. The two types of layers have a wavelength of about 3.2 nm. It was shown that B2 phase in the layer was NiAl. The reason for the formation of NiAl at nano scale in preference to FeAl is the higher negative heat of mixing between Ni and Al compared to Fe and Al.

6.5. References

1. K. Hono, Nanoscale microstructural analysis of metallic materials by atom probe field ion microscopy, Progress in Materials Science, 47 (2002), p.621
2. M.K. Miller, Atom Probe Tomography: Analysis at the Atomic Level (2000), 1st edition, Kluwer Academic/Plenum Publishers, New York.
3. Z. Guo, W. Sha, and D. Vaumousse, Microstructural evolution in a PH13-8 stainless steel after ageing, Acta Materialia, 51 (2003), p.101
4. D. Blavette, C. Martin, and J. Gallot, Atomic probe analysis of precipitates in a FeCr20Ni2Al2 alloy, Scripta Metallurgica, 16 (1982), p.59
5. S.D. Erlach, H. Leitner, M. Bischof, H. Clemens, F. Danoix, D. Lemarchand, and I. Siller, Comparison of NiAl precipitation in a medium carbon secondary hardening steel and C-free PH13-8 maraging steel, Materials Science and Engineering A, 429 (2006), p.96
6. F.R. de Boer, R. Boom, W.C.M. Mattens, A.R. Miedema, and A.K. Niessen, Cohesion in Metals: Transition Metal Alloys. Vol. 1 (1988), Elsevier Science Publishers B. V, P. O. Box 103, 1000 AC Amsterdam, The Netherlands,

CHAPTER 7: MECHANICALLY INDUCED FCC PHASE FORMATION IN NANOCRYSTALLINE HAFNIUM

7.1. Introduction

Nanocrystalline materials have been receiving the serious attention of researchers in recent years. This has been essentially due to the fact that, in comparison to the coarse-grained materials, nanocrystalline materials possess different and often superior mechanical, electrical, and magnetic properties [1-5]. In addition to the improvement in properties, there have also been several reports on constitutional changes and phase transformations in materials that have nanometered grain sizes. These transformations include allotropic transformations in pure metals [6-10], alloys [11], and compounds [12]. It has also been reported that solid solubility limits could be significantly increased by nanostructure pressing [13-14]. Thus, there appears to be great potential in altering the crystal structure and consequently the properties of nanocrystalline materials. In addition to these experimental observations, there have also been some theoretical studies which reported that allotropic transformations could be induced in pure metals when their grain sizes reach below some critical values [15]. Crystal lattice distortion and interfacial effects were found to be the reasons for structural instability.

During a detailed investigation on the effects of mechanical alloying on the amorphization behavior and constitution of Cu-Hf binary powder mixtures containing about 35 at.% Hf, we noted the formation of a face-centered cubic (FCC) phase with a lattice parameter of 0.4566 nm. Occurrence of such an FCC phase in the Cu-Hf system could not be explained on the basis of formation of a supersaturated solid solution of Hf in Cu achieved by mechanical alloying methods. It was also not possible to explain this observation on the basis of a metastable intermetallic phase with the composition of either Cu_2Hf or Hf_2Cu having the CaF_2-type crystal

structure. Since it is possible that the equilibrium hexagonal close-packed (HCP) form of Hf could undergo an allotropic transformation to the FCC form under the non-equilibrium conditions of mechanical alloying, it was decided to investigate whether this is a possibility in the pure metal Hf. Thus, we report here the HCP → FCC phase transformation in nanostructured elemental hafnium induced by mechanical milling. Under equilibrium conditions Hf exists in the HCP form with a = 0.3195 nm, c = 0.5051 nm, and c/a = 1.581 up to 1743 ^{o}C. Above this temperature, it transforms to the body-centered cubic (BCC) form with a = 0.3610 nm [16].

7.2. Results

Figure 7.1 shows the XRD patterns of Hf as a function of milling time. The as-received powder showed all the peaks expected from the HCP structure with the lattice parameters a = 0.3196 nm and c = 0.5054 nm. On milling the powder, the diffraction peaks became broader due to grain refinement and introduction of lattice strain. But, after milling for as short as 0.5 h, some new diffraction peaks, although with low intensity, started appearing. The intensity of these new peaks continued to increase with milling time and that of the HCP peaks decreased. Such a situation continued till 5 h, when the peaks characteristic of the HCP phase were completely absent and therefore, it could be concluded that the HCP phase has completely transformed to this new phase. All the peaks of this new phase could be most satisfactorily indexed on the basis of an FCC structure. Based on the appropriate extrapolation functions to obtain the precise lattice parameter, it was noted that the lattice parameter for this new FCC phase was a = 0.4566 nm. No further structural changes in the powder occurred even after milling the powder for longer periods of time, say 10 h.

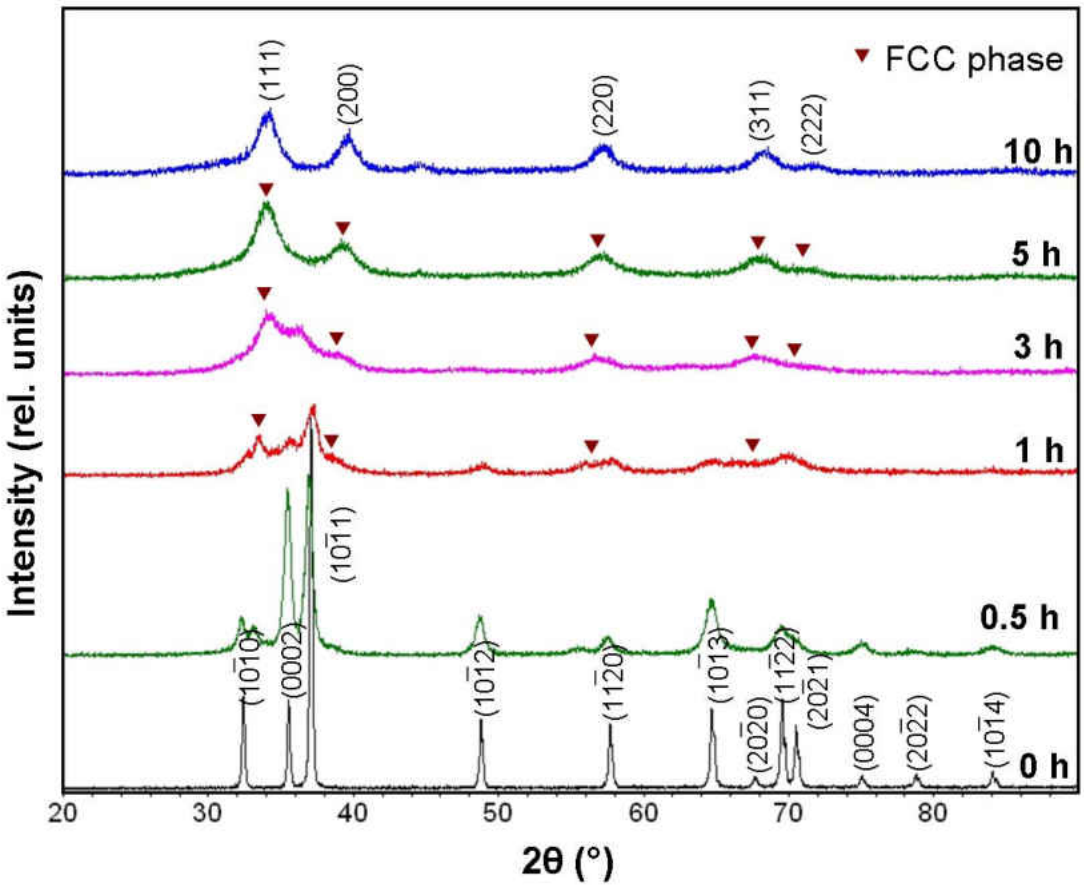

Figure 7.1: X-ray diffraction patterns of the pure metal powder hafnium mechanically milled from 0.5 to 10 h. HCP → FCC phase transformation was observed which was completed by 5 h of milling. No further changes were detected on continued milling up to 10 h.

Figure 7.2 shows the fraction of the FCC phase formed in the milled Hf powder as a function of milling time. It was noted that the kinetics of formation of the FCC phase were quite fast in the early stages of milling and then they decreased at a later stage. Complete transformation from the HCP to the FCC phase took place in about 5 h.

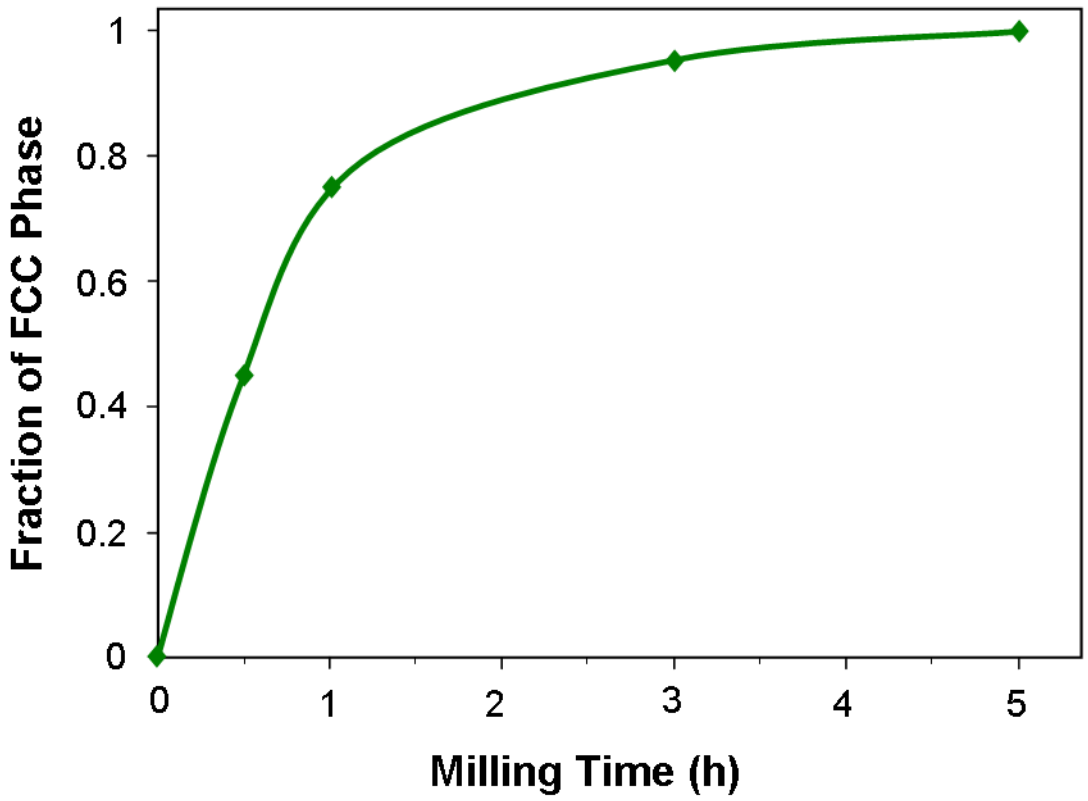

Figure 7.2: Variation of the fraction of FCC phase formed in mechanically milled Hf powder as a function of milling time. While the transformation from the HCP to the FCC phase started on milling the powder for 0.5 h, the transformation was complete in about 5 h.

Formation of the FCC phase was confirmed through electron diffraction methods also. Figure 7.3 shows the electron diffraction pattern from the powder milled for 5 h. The pattern was indexed on the basis of an FCC structure with the lattice parameter a = 0.45 nm, and this value is very close to the result obtained from the XRD patterns.

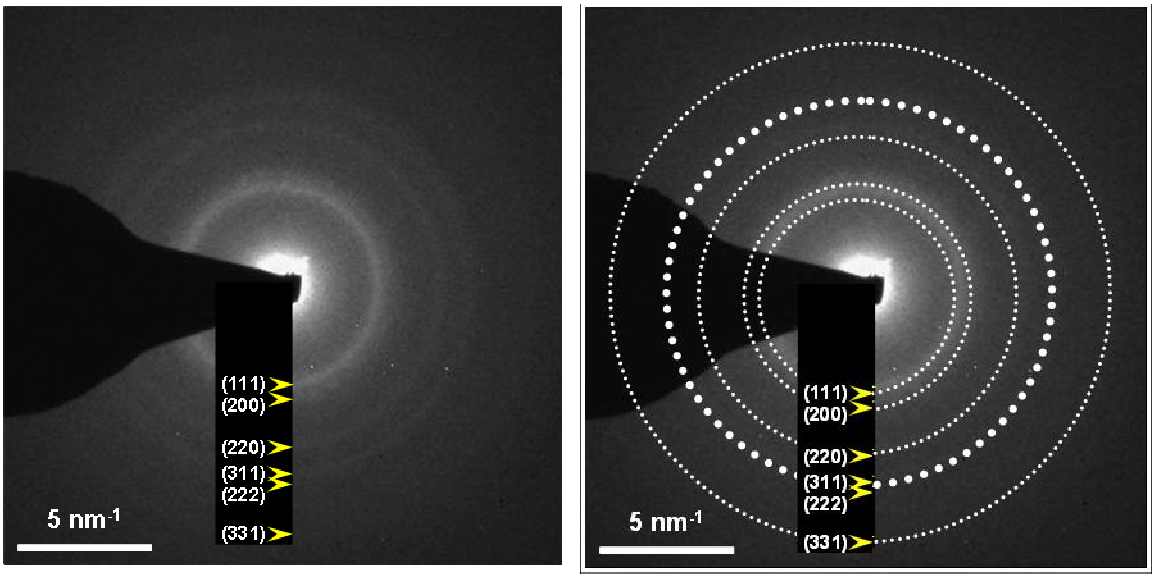

Figure 7.3: Electron diffraction pattern of the Hf powder milled for 5 h, confirming the presence of only an FCC phase at this stage.

The crystallite (grain) size of both the parent HCP and product FCC phases was measured at different milling times and the results are shown in Figure 7.4. The crystallite size variation is typical of mechanically milled powders. The grain size decreased initially at a very fast rate and reached about 10 nm on milling the powder for 1 h. From then onwards, the rate of decrease of crystallite size was slow. The minimum crystallite size achieved in the HCP phase was 5 nm. The crystallite size of the FCC phase at the start of its formation was approximately 7 nm and decreased slowly to a value of 3 nm at 5 h, suggesting that the formation of this phase could probably be associated with grain size reduction into the nanometer range.

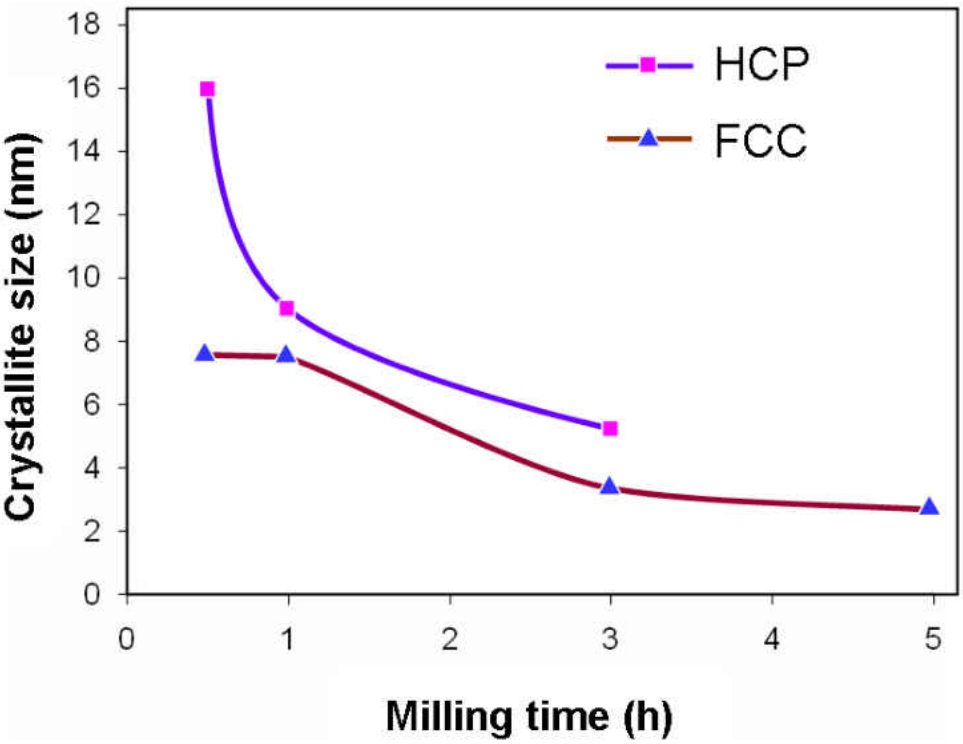

Figure 7.4: Variation of the crystallite size in both the HCP and FCC phases of hafnium as a function of milling time. The crystallite size decreased rapidly in the early stages of milling and reached a minimum value of about 3 nm in the FCC phase.

The variation of lattice strain in the milled powder in both the HCP and FCC forms of Hf was estimated from the peak widths and the values are plotted in Figure 7.5. The lattice strain increased in both the cases with milling time. While the strain was compressive in nature when the powder was in the FCC form, it was tensile in the HCP form.

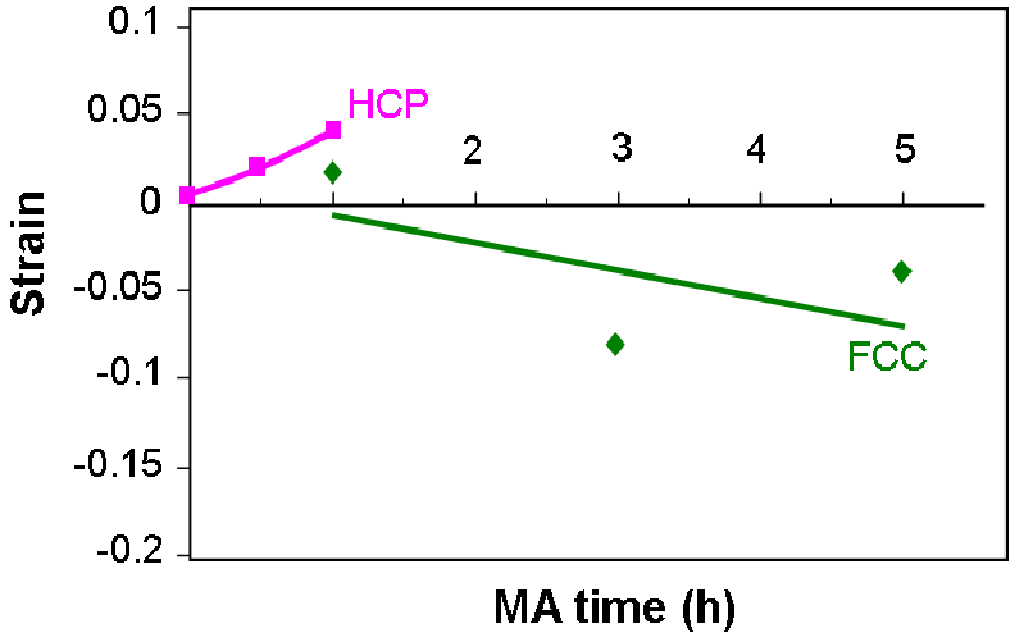

Figure 7.5: Variation of lattice strain in the mechanically milled Hf powder as a function of milling time. Note that the strain increases with increasing milling time (up to the time investigated) and that the strain is compressive in nature in the FCC form

7.3. Discussion

From the above results, it becomes clear that an FCC phase had formed on mechanically milling the Hf metal powder for 5 h. Since there is no stable equilibrium phase of Hf with the FCC structure, it can be assumed that this is a metastable form of Hf formed under the non-equilibrium conditions of MM. Therefore, it becomes important for us to investigate the reasons for its formation.

Assuming that the Hf metal has undergone an allotropic transformation, we can calculate the lattice parameter of the hypothetical FCC phase of Hf on the basis of the lattice parameters of the equilibrium HCP structure and using the relationship:

$$a_{FCC} = \sqrt{2} \times a_{HCP} = \sqrt{2} \times 0.3195 \text{ nm} = 0.4517 \text{ nm} \quad \ldots\ldots \quad \text{Eq.(2)}$$

Assuming an ideal axial ratio of 1.633 for the HCP structure of Hf, even though this is not actually true, and it is 1.581, the lattice parameter of the FCC phase can also be calculated using the relationship:

$$a_{FCC} = \sqrt{2} \times (c_{HCP}/1.633) = \sqrt{2} \times (0.5051 \text{ nm}/1.633) = 0.4374 \text{ nm}. \quad \ldots\ldots \quad \text{Eq.(3)}$$

Alternatively, assuming that the closest distance of approach between two atoms, $2r$ in an HCP structure with a non-ideal axial ratio is given by

$$2r = \sqrt{\frac{a^2}{3} + \frac{c^2}{4}} \quad \ldots\ldots \quad \text{Eq.(4)}$$

the lattice parameter of the hypothetical FCC phase formed from such an HCP structure is calculated to be 0.4422 nm.

It has also been suggested [17] that the closest distance of approach between atoms in the HCP structure is along the <20$\bar{2}$3> directions and is given by:

$$2r = \frac{a\left[4+3\left(\frac{c}{a}\right)^2\right]^{1/2}}{2\sqrt{3}} \qquad \ldots\ldots \quad \text{Eq.(5)}$$

According to this equation, the closest distance of approach in the HCP structure of Hf is calculated to be 0.3128 nm and therefore, the lattice parameter of the hypothetical FCC phase is 0.4422 nm.

Thus, the lattice parameters of the FCC phase calculated by any of the above four methods are somewhat close to each other, differing only by about 3%. The lattice parameter of the FCC phase formed in the Hf powder in the present investigation (0.4566 nm) is slightly larger than any of these values. We will see later that this increase is related to the nanostructured grains formed, and possibly contamination, in the milled powder.

Allotropic phase transformations in pure metals can occur due to changes in temperature, pressure, or alloying additions. Additionally, changes in microstructural parameters such as grain size, surface energy, or stacking fault energy can have a significant influence in affecting these transformations. Stabilization of some phases due to the presence of impurities, especially during mechanical alloying/milling of powders, is also well known [18-20]. Let us now look at the different possibilities to explain the occurrence of the HCP → FCC transformation in elemental Hf.

7.3.1. Effect of Temperature

As mentioned earlier, Hf exists in the HCP form at room temperature and transforms to the BCC form, which is stable at temperatures >1743 ^{o}C. The process of MM takes place at or near room temperature. But, due to the high-energy milling conditions, a slight rise in powder temperature is reported to occur. There have been different estimates of the local temperature rise, but it is now accepted that it is not more than about 200 ^{o}C [19, 21-22]. Thus, this temperature rise obtained during milling is not sufficient enough to cause any crystal structure change in the Hf powder. Further, irrespective of whether the temperature rise is responsible for this transformation or not, there is no reported stable phase of Hf with the FCC structure at high temperatures. Therefore, formation of an FCC phase in Hf due to changes in temperature can be completely ruled out.

7.3.2. Effect of Pressure

Allotropic phase transformations in pure metals due to application of high pressures have been known for a long time [23]. New metastable phases have also been reported to form at relatively high pressures [24]. It has been estimated that very high pressures of the order of 6-8 GPa could be developed during mechanical alloying/milling due to the impact forces exerted by the grinding medium on the powders [25]. But, there have not been any reports of formation of an FCC phase in Hf under high pressures so far. Thus, even though it is possible that this FCC phase could be a high-pressure polymorph of Hf, this fact can only be confirmed if an FCC form of Hf is obtained by subjecting the pure metal Hf to regular high pressures and not inside the SPEX milling container.

7.3.3. Effect of Stacking-fault Energy

Metals with low stacking-fault energy, e.g., Co are expected to easily undergo allotropic transformations through a twinning mechanism, similar to a martensitic transformation [26]. This has been reported in mechanically milled metal powders also [6]. Thus, a possibility for the HCP → FCC allotropic transformation in Hf in the present study is a twinning process. Formation of twins occurs easily in materials with a low stacking-fault energy [27]. But, Igarashi et al. [28] have estimated the stacking-fault energy of Hf to be about 111 mJ/m^2. This value is neither very low (20 to 40 mJ/m^2) like that in Co or austenitic stainless steel nor very high (200 mJ/m^2) like that in Al. However, formation of twins has been reported to occur in the so-called high stacking-fault energy metals also when they exist in the nanocrystalline state. Accordingly, twins were reported to form in cryomilled nanocrystalline Al [29-30], as predicted by molecular dynamics simulation studies [31]. It has been suggested that the stacking-fault energy of a metal decreases with a decrease in the grain size to nanometer dimensions and helps in the formation of twins. A rationale was recently provided for the strong dependence of mechanical twinning on grain size [32]. Since the grain size obtained in the present investigation is in the nanometer range, it is possible that low stacking-fault energy (and consequently twinning) could be the reason for the formation of the FCC phase in Hf.

Zheng et al. [33] have recently reported, through molecular dynamics simulations, that the HCP → FCC transformation in nanocrystalline cobalt during tension and compression was due to the accumulation of deformation faults.

7.3.4. Effect of Nanocrystallinity

From Figure 7.4 it is clear that the FCC-Hf phase produced in this investigation is nanocrystalline in nature with a typical crystallite (grain) size of a few nanometers. Since nanocrystalline materials are characterized by small grain sizes and a large volume fraction of atoms residing at the grain boundaries (and therefore large surface areas), the thermodynamic stabilities of the different phases could be significantly altered [1-5]. Consequently, it has been possible to synthesize metastable phases which are different from those present in their coarse-grained counterparts. Further, a significant amount of strain is also stored in the lattice of the milled powder (Figure 7.5). Therefore, it is worthwhile to consider the effects of nanocrystallinity on the thermodynamic stabilities of the competing phases in Hf under the conditions of MM.

The different factors that contribute to the free energy of the nanocrystalline system are the surface energy, excess free volume, and lattice strain. The contribution to the increase in the free energy in a nanocrystalline material has to be considered in terms of the decreased grain size and associated increase in the grain boundary component.

A reduction in grain size (L) leads to an increase in the free energy, ΔG of the system due to the Gibbs-Thompson effect according to the equation [34]

$$\Delta G = \frac{4\gamma N_A V_a}{L} \qquad \text{..... Eq.(6)}$$

where γ is the interfacial energy, N_A is the Avogadro's number, and V_a is the atomic volume. The atomic volumes of Hf in the HCP and FCC forms were calculated, from the respective lattice parameter values, as $V_{HCP} = 0.0223$ nm^3 and $V_{FCC} = 0.0236$ nm^3, suggesting that the HCP

→ FCC transformation is associated with an approximately 6% volume increase. Such lattice expansions on phase transformations and/or on decreasing the grain size were reported earlier in Nb [35], Ni [36], Ti [9], and Zr [8], among others. This increase in V_a is expected to result in an increase in the free energy of the system.

On the other hand, it has been shown earlier [37] that atoms in the grain boundaries of nanocrystalline materials are randomly displaced from their regular atomic sites and therefore they contain a certain amount of excess free volume. The excess free volume, ΔV_F associated with the atoms in the grain boundaries can be calculated using the equation:

$$\Delta V_F = \frac{(L+\Delta/2)^2 - L^2}{L^2} \qquad \ldots\ldots \quad \text{Eq.(7)}$$

where L is the grain size and Δ is the grain boundary width. Even though Δ has been traditionally assumed to be 1 nm, and independent of grain size [38] it has been shown recently [35] that the value of Δ changes with the grain size of the nanocrystalline material and that it increases with a decrease in the grain size. This excess free volume generates a negative hydrostatic pressure (from core to periphery) and could result in crystal lattice expansion. At a grain size of d = 7.5 nm, the value of ΔV_F has been calculated to be 0.14.

Rose et al. [39] used a lattice dilatation model known as the isothermal equation of state, which was subsequently adopted by Fecht [40] to calculate the hydrostatic pressure at the grain boundaries in nanocrystalline materials. The hydrostatic pressure, P_h was calculated using the equation:

$$P_h = -\frac{3B_o\left[(V/V_o)^{1/3} - 1\right]}{(V/V_o)^{2/3}} \exp(-a^*) \times \left[1 - 0.15a^* + 0.05(a^*)^2\right] \qquad \ldots\ldots \quad \text{Eq.(8)}$$

where B_o is the equilibrium bulk modulus, V_o is the volume per atom of the equilibrium coarse-grained material, V is the volume per atom in the nanocrystalline state, and a^* is the scaling parameter defined as $(r_{WS} - r_{WSe})/L$, where r_{WS} is the real Wigner-Seitz cell radius of the atom with a volume V and r_{WSe} is the Wigner-Seitz cell radius of the atom with a volume V_o, and L is the length scale (grain size) characteristic of the metal. It is to be noted that ΔV_F in equation (7) is related to equation (8) through the relationship:

$$\Delta V_F = \frac{V - V_o}{V_o} \qquad \ldots\ldots \quad \text{Eq. (9)}$$

Using the appropriate values for the different parameters, P_h has been calculated to be -10.5 GPa for a grain size of 7.5 nm in Hf.

The product of the negative hydrostatic pressure and atomic volume change (difference in the atomic volumes of the HCP and FCC forms of Hf), i.e., $P_h \times \Delta V_a$, is an energy term and these values can be calculated as a function of grain size. It is noted that the energy increases with a decrease in grain size. For the grain size of 7.5 nm observed in the present study, the $P_h \times \Delta V_a$, value has been calculated to be 3,450 cal/mol. Kaufman [41] has theoretically estimated the free energy change necessary for the transformation of metals from the HCP to FCC structures as 800 cal/mol. That amount of energy can be obtained when the grain size of Hf metal is reduced to about 18.7 nm. That is, below a grain size of 18.7 nm, the Hf metal has sufficiently high energy to transform from the HCP to the FCC structure. Since the grain size obtained in the milled Hf powder (with the FCC structure) was 7.5 nm (and therefore the energy available is large), it can be argued that the excess energy present, as a result of reduction in grain size, could have stabilized the FCC phase in Hf.

The increase in energy due to the combination of the above effects may eventually cause a high order of lattice instability and consequently the HCP phase of Hf could adopt a new polymorph with greater topological or surface density of atoms, but without altering the crystal packing density (=74%) [8-9, 11]. Thus, the HCP → FCC transformation observed in elemental Hf in this investigation can be considered an allotropic transformation.

It has been frequently highlighted in the literature on crystal chemistry that metals in the same group of the periodic table have the same (or similar) crystal structures. Thus, under equilibrium conditions, the Group IV transition metals Ti, Zr, and Hf have the HCP crystal structure at room temperature and transform to the BCC structure at elevated temperatures. Formation of metastable FCC allotropes has been reported to occur in mechanically milled Ti [9] and Zr [8] powders. Therefore, it can be expected that a similar metastable FCC phase would form in mechanically milled Hf powder and the result obtained in the present investigation fulfills this expectation.

7.3.5. Presence of Impurities

This is yet another possibility for a phase transformation to occur in pure metals. Since we are dealing with only a pure metal in this investigation, presence of alloying elements as responsible for the formation of an FCC phase can be ruled out. But, the technique of mechanical alloying/milling is known to introduce impurities (both substitutional and interstitial) into the milled powder and this has been recognized as a serious limitation of the technique in developing novel materials for advanced applications. The impurities could be either metallic in nature from the milling medium and/or the milling container or gaseous from the ambient atmosphere in

which the milling is done, or the process control agent added occasionally to minimize excessive cold welding between ductile metal particles [21].

Interstitial phases with an FCC structure are present in the Hf-C and Hf-N systems. Table 7.1 lists the crystal structures and lattice parameters of these phases. The lattice parameter of the FCC phase synthesized by mechanical milling of Hf powders was calculated as a = 0.4566 nm. Comparison with the values in Table 7.1 clearly suggests that the FCC phase obtained in this investigation has a lattice parameter smaller than that of HfC (a = 0.4633 nm), but larger than that of HfN (a = 0.4525 nm). Thus, we need to decide whether it is possible for the new FCC phase formed in the milled Hf powder to be either HfC or HfN.

Table 7.1: Structural parameters of pure Hf and the interstitial phases with an FCC structure in the Hf-C and Hf-N systems

Phase	Crystal structure (Prototype, Strukturbericht designation)	Pearson symbol	Space group	Composition range of stability* (at.%)	Lattice parameters	
					a (nm)	c (nm)
α-Hf	HCP (Mg, A3-type)	hP2	$Im\bar{3}m$	100% Hf	0.3195	0.5051
β-Hf	BCC (W, A2-type)	cI2	$P6_3/mmc$	100% Hf	0.3610	-
HfC	FCC (NaCl, B1-type)	cF8	$Fm\bar{3}m$	37.5 - 49.5 at.% C	0.4633	-
HfN	FCC (NaCl, B1-type)	cF8	$Fm\bar{3}m$	46 - 52.5 at.% N	0.4525	-

*at room temperature

Further, assuming that the HfN phase may also exist in a metastable condition with the ZnS, B3-type (cubic) structure, the lattice parameter for this hypothetical phase was calculated to be 0.4883 nm. Since this value is substantially larger than the experimentally observed value, the possibility that the observed FCC phase in the present investigation could be the ZnS-type cubic HfN has been discounted.

Apart from a match of the diffraction angles, the relative intensities of the different diffraction peaks in the structure also need to match to ensure that the structure assigned to it is correct. Accordingly, the relative intensities, I_{rel} of the first five allowed reflections in the FCC structure, viz., 111, 200, 220, 311, and 222 have been calculated using the equation:

$$I_{rel} = \left|F_{hkl}\right|^2 \, p\left(\frac{1+\cos^2 2\theta}{\sin^2\theta\cos\theta}\right) \qquad \ldots\ldots \quad \text{Eq.(10)}$$

where F_{hkl} is the structure factor for the *hkl* reflection, p is the multiplicity factor, $\left(\frac{1+\cos^2 2\theta}{\sin^2\theta\cos\theta}\right)$ is the Lorentz-polarization factor, and θ is the Bragg angle. The intensity values were calculated for three different crystal structures, viz., B1-type HfC, B1-type HfN, and hypothetical FCC form of Hf. Figure 7.6 compares these calculated intensities with the intensities observed for the FCC phase in the present investigation.

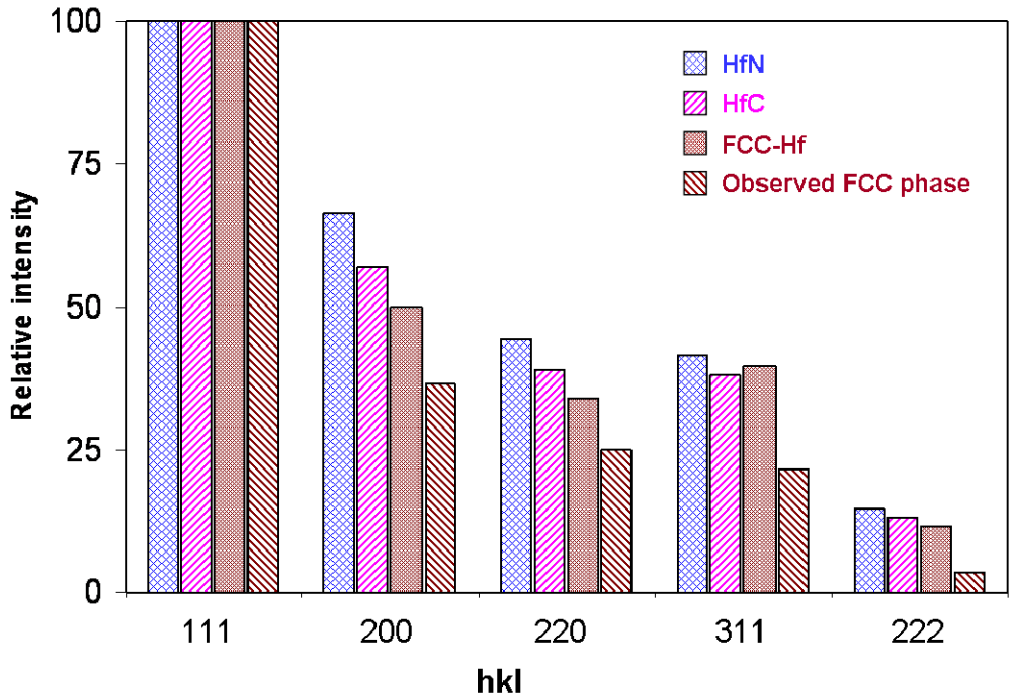

Figure 7.6: Comparison of the relative intensities of the first five diffraction peaks of the FCC structure (111, 200, 220, 311, and 222) for four different cases – experimentally observed FCC phase, hypothetical FCC phase of Hf, NaCl, B1-type HfC, and NaCl, B1-type HfN. Note that the observed intensities seem to match better with the hypothetical FCC phase.

A few general observations may be noted from the Figure 7.6. Firstly, it is clear that the trend of variation of the intensities for the different diffraction peaks is the same for all the four structures – observed FCC phase, hypothetical FCC Hf, NaCl (B1)-type HfC, and NaCl (B1)-type HfN phases. Secondly, it may be noted that the intensities of the hypothetical FCC-Hf phase and the observed FCC phase are somewhat lower than those of the HfC and HfN phases for the 200, 220, 311, and 222 reflections (except for a small reversal between FCC-Hf and HfC phases for the 311 reflection). In fact, the intensities of the observed FCC phase are significantly lower than those calculated for the HfC and HfN phases, but much closer to those of hypothetical FCC-Hf phase. Therefore, from these intensity calculations, it is very unlikely that the observed

FCC phase in the present investigation is either the B1-type HfN or HfC phase. It is more likely that it is the hypothetical (metastable) FCC phase of Hf.

In addition to the diffraction angles and relative intensities of the different diffraction peaks, it is also important to ensure that the chemical composition of the new phase matches with that of the identified phase. According to the binary Hf-N and Hf-C phase diagrams, the HfN phase exists over a composition range of 46 to 52.5 at.% N, and the HfC phase in the composition range of 37.5 to 49.5 at.% C, at room temperature. That means for the homogeneous HfN and HfC phases to form in the milled powder, one needs a minimum of 46 at.% nitrogen and 37.5 at.% carbon, respectively.

Conventional wet chemical analysis of the Hf powder milled for 5 h showed that the nitrogen content in the powder was a maximum of 14 at.% and 12 at.% on milling for 5 h and 10 h, respectively in the worst possible milling condition. (Since the chemical analysis was done some time after the powders were milled, it is possible that the powders picked up additional nitrogen during storage.) Even though these values are slightly high (the nitrogen contamination was much less when proper precautions were taken), they are not high enough to form the HfN phase. According to the Hf-N binary phase diagram, the solid solubility of nitrogen in hafnium at room temperature is 29 at.% and therefore, only an interstitial solid solution of nitrogen in HCP-Hf is expected to form up to this nitrogen level. But, we did not detect the presence of any HCP phase along with the FCC phase in the powder milled for 5 h or longer. This observation suggests that with the amount of nitrogen present, it is not possible to produce even a small amount of the HfN phase in the milled powder and that the FCC phase observed in the milled

powder cannot be the HfN phase. Hf(N) solid solution phase with the HCP structure is also not present in the milled powder.

Similarly, the carbon content in the Hf powder was 10 at.% on milling for 5 h and 9 at.% in the powder milled for 10 h. These values are not again high enough for any HfC to form in the powder. Accordingly, it is fair to assume that the new FCC phase formed in the milled Hf powder is neither HfN nor HfC.

Significant levels of impurities were also reported in mechanically milled titanium [9], and other metals earlier and these authors also had discounted the possibility of the new FCC phases being interstitial compounds containing nitrogen, carbon, or oxygen. In view of these observations, it will be difficult to interpret the formation of the FCC phase in the milled Hf powder purely as a contaminant phase.

From the above discussion, it appears that it will be difficult to decide the origin of the FCC phase in the milled Hf powder. Three possibilities stand out – one is the allotropic transformation, the second is the nanocrystalline nature of the powder, and the last is powder contamination. It cannot be determined unambiguously that an allotropic transformation is occurring in the pure metal Hf since the powder contained significant amount of nitrogen and carbon as impurities. But, the powder contamination by either nitrogen or carbon alone is not sufficiently high to homogeneously form either HfN or HfC. However, if we consider that the FCC phase formed in the milled powder is a solid solution of these two phases, i.e., hafnium carbonitride [Hf(N,C)] with unequal proportions of carbon and nitrogen, it may be possible to resolve the confusion to some extent.

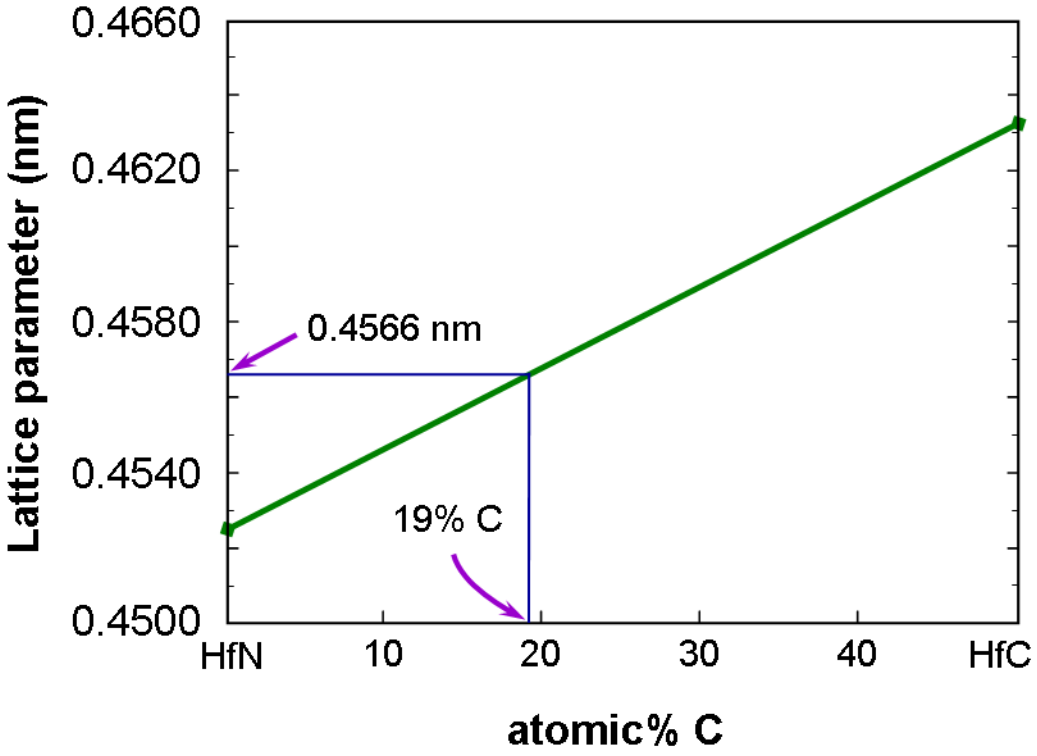

Figure 7.7: Variation of the lattice parameter of the Hf(N,C) phase as a function of carbon content. From this plot, the lattice parameter of 0.4566 nm observed for the FCC phase in the present investigation corresponds to a carbon content of 19 at.% and a nitrogen content of 31 at.%, or in the ratio of approximately 2:3.

Assuming that the HfN and HfC phases form an isomorphous system, and that the system obeys the Vegard's law (linear variation of lattice parameter with solute content), Figure 7.7 plots the variation of the lattice parameter of the Hf(N,C) phase as a function of carbon content. If we assume that the FCC phase formed in the present investigation is a contaminant Hf(N,C) phase, the calculated lattice parameter of 0.4566 nm for the FCC phase corresponds to a carbon content of 19 at.% and a nitrogen content of 31 at.%, or in the ratio of 0.38 to 0.62 (and the rest Hf). Thus, it can be estimated that the FCC phase has a stoichiometry of $Hf(C_{0.4}N_{0.6})$. But, the

measured carbon and nitrogen contents in the milled powder are only about 10 at.% carbon and 14 at.% nitrogen, or approximately half the required concentrations. From these observations, it can be assumed that the milled powder certainly contains the contaminant phase, but only to the extent of about 50%. Since the carbon and nitrogen contents are not sufficiently high to form the $Hf(C_{0.4}N_{0.6})$ phase homogeneously, it is likely that the milled powder contains about 50% of the $Hf(C_{0.4}N_{0.6})$ phase and the rest another phase. But, it should be noted that the observed XRD pattern contains only one phase with the FCC structure and a = 0.4566 nm. Therefore, it can be inferred that in addition to the $Hf(C_{0.4}N_{0.6})$ phase, the milled powder contains another phase with the same structure and lattice parameter. It is very likely that this additional phase is the FCC allotrope of Hf formed under the non-equilibrium conditions of MM. But, since the lattice parameter calculated for the FCC allotrope of Hf is smaller than the observed value, the observed larger value could be due to the nanocrystallinity of the powder. Thus, it appears that the FCC phase in the milled Hf powder in the present investigation can be considered to be a mixture of the product of an allotropic transformation and a contaminant phase. At present it is not clear whether the FCC allotrope has formed first and subsequently the contaminant phase has formed due to contamination of the powder or the contaminant FCC phase has triggered the allotropic transformation. Additional and detailed investigations are required to unambiguously determine whether a true allotropic transformation is occurring in Hf.

7.4. Conclusions

A phase transformation from the equilibrium HCP structure to the FCC structure occurred on milling pure Hf metal powder in a high-energy SPEX shaker mill. It was noted that during milling of the Hf powder, the grain (crystallite) size decreased to the nanometer level and there was also significant lattice strain in the milled powder. The formation of the FCC phase was also accompanied by lattice expansion, leading to an increase in volume per atom by about 6%. Based on the different possibilities for the formation of the FCC phase in Hf, viz., effects of temperature, pressure, nanocrystallinity, allotropic transformation, and impurities, etc., it was difficult to pinpoint the exact reason for the formation of the FCC phase. From the available evidence, it appears that the final powder may contain about 50% of the FCC phase as a result of the allotropic transformation and the rest, a contaminant $Hf(C_{0.4}N_{0.6})$ phase. This conclusion was reached because the amount of interstitial impurities (10 at.% carbon and 14 at.% nitrogen) was not sufficiently high to form the $Hf(C_{0.4}N_{0.6})$ phase homogeneously.

7.5. References

1. H. Gleiter, Nanocrystalline materials, Progress in Materials Science, 33 (1989), p.223
2. C. Suryanarayana, Nanocrystalline materials, International Materials Reviews, 40 (1995), p.41
3. H. Gleiter, Nanostructured materials: basic concepts and microstructure, Acta Materialia, 48 (2000), p.1
4. C. Suryanarayana, Recent developments in nanostructured materials, Advanced Engineering Materials, 7 (2005), p.983
5. C.C. Koch, ed., Nanostructured Materials, 2nd. edition, (2007), William Andrew, Norwich, NY.
6. J.Y. Huang, Y.K. Wu, and H.Q. Ye, Allotropic transformation of cobalt induced by ball milling, Acta Materialia, 44 (1996), p.1201
7. L. Del Bianco, C. Ballesteros, J.M. Rojo, and A. Hernando, Magnetically ordered fcc structure at the relaxed grain boundaries of pure nanocrystalline Fe, Physical Review Letters, 81 (1998), p.4500
8. I. Manna, P.P. Chattopadhyay, F. Banhart, and H.J. Fecht, Formation of face-centered-cubic zirconium by mechanical attrition, Applied Physics Letters, 81 (2002), p.4136
9. I. Manna, P.P. Chattopadhyay, P. Nandi, F. Banhart, and H.J. Fecht, Formation of face-centered-cubic titanium by mechanical attrition, Journal of Applied Physics, 93 (2003), p.1520
10. P.P. Chattopadhyay, S.K. Pabi, and I. Manna, A metastable allotropic transformation in Nb induced by planetary ball milling, Materials Science and Engineering A, 304-306 (2001), p.424
11. S. Bera and I. Manna, Polymorphic phase transformation in $Ti_{50}Zr_{50}$ binary alloy by mechanical alloying, Materials Science and Engineering A, 417 (2006), p.110
12. Z. Li, H. Hahn, and R. Siegel, New phases of erbium oxides, Materials Letters, 6 (1988), p.342
13. C. Suryanarayana and F.H. Froes, Nanocrystalline titanium-magnesium alloys through mechanical alloying, Journal of Materials Research, 5 (1990), p.1880

14. Y. Ogino, S. Murayama, and T. Yamasaki, Influence of milling atmosphere on amorphization of chromium and Cr-Cu powders by ball milling, Journal of the Less Common Metals, 168 (1991), p.221
15. W. Qin, T. Nagase, and Y. Umakoshi, Phase stability in nanocrystalline metals: A thermodynamic consideration, Journal of Applied Physics, 102 (2007), p.124303
16. T.B. Massalski, ed., Binary Alloy Phase Diagrams 2 edition (1990), ASM International, Materials Park, Ohio.
17. J. Christian, The Theory of Transformations in Metals and Alloys (Part I) (2002), Pergamon Press, Oxford.
18. C. Suryanarayana and M.G. Norton, X-Ray Diffraction: A Practical Approach (1998), Plenum Press, New York.
19. C. Suryanarayana, Mechanical Alloying and Milling (2004), Marcel Dekker, New York.
20. C. Suryanarayana, Does a disordered γ-TiAl phase exist in mechanically alloyed Ti-Al powders?, Intermetallics, 3 (1995), p.153
21. C. Suryanarayana, Mechanical alloying and milling, Progress in Materials Science, 46 (2001), p.1
22. C. Koch, Temperature effect during mechanical attrition, Int. J. Mechanochem. Mech. Alloying, 1 (1994), p.56
23. C.S. Barrett and T.B. Massalski, Structure of Metals (1966), 3rd edition, McGraw Hill, New York.
24. J. Jamieson and A. Lawson, X-ray diffraction studies in the 100 kilobar pressure range, Journal of Applied Physics, 33 (1962), p.776
25. D. Maurice and T. Courtney, The physics of mechanical alloying: a first report, Metallurgical and Materials Transactions A, 21 (1990), p.289
26. P. Tolédano, G. Krexner, M. Prem, H. Weber, and V. Dmitriev, Theory of the martensitic transformation in cobalt, Physical Review B, 64 (2001), p.144104
27. R. Abbaschian, L. Abbaschian, and R. Reed-Hill, Physical Metallurgy Principles (2009), 4th edition, Cengage Learning, Stamford, CT.
28. M. Igarashi, M. Khantha, and V. Vitek, N-body interatomic potentials for hexagonal close-packed metals, Philosophical Magazine Part B, 63 (1991), p.603

29. X. Liao, F. Zhou, E. Lavernia, D. He, and Y. Zhu, Deformation twins in nanocrystalline Al, Applied Physics Letters, 83 (2003), p.5062
30. M. Chen, E. Ma, K. Hemker, H. Sheng, Y. Wang, and X. Cheng, Deformation twinning in nanocrystalline aluminum, Science, 300 (2003), p.1275
31. V. Yamakov, D. Wolf, S.R. Phillpot, A.K. Mukherjee, and H. Gleiter, Dislocation processes in the deformation of nanocrystalline aluminium by molecular-dynamics simulation, Nature Materials, 1 (2002), p.45
32. M. Barnett, A rationale for the strong dependence of mechanical twinning on grain size, Scripta Materialia, 59 (2008), p.696
33. G.P. Zheng, Y.M. Wang, and M. Li, Atomistic simulation studies on deformation mechanism of nanocrystalline cobalt, Acta Materialia, 53 (2005), p.3893
34. D.A. Porter and K.E. Easterling, Phase Transformations in Metals and Alloys (2005), Thornton Publishers, London.
35. R. Banerjee, E.A. Sperling, G.B. Thompson, H.L. Fraser, S. Bose, and P. Ayyub, Lattice expansion in nanocrystalline niobium thin films, Applied Physics Letters, 82 (2003), p.4250
36. X.D. Liu, H.Y. Zhang, K. Lu, and Z.Q. Hu, The lattice expansion in nanometre-sized Ni polycrystals, Journal of Physics: Condensed Matter, 6 (1994), p.L497
37. S. Phillpot, D. Wolf, and H. Gleiter, Molecular dynamics study of the synthesis and characterization of a fully dense, three dimensional nanocrystalline material, Journal of Applied Physics, 78 (1995), p.847
38. R. Siegel, Processing of Metals and Alloys, edited by R.W. Cahn, (1991), VCH Publishers, Weinheim, p. 583.
39. J.H. Rose, J.R. Smith, F. Guinea, and J. Ferrante, Universal features of the equation of state of metals, Physical Review B, 29 (1984), p.2963
40. H.J. Fecht, Thermodynamic properties and stability of grain boundaries in metals based on the universal equation of state at negative pressure, Acta Metallurgica et Materialia, 38 (1990), p.1927
41. L. Kaufman, in *Phase Stability in Metals and Alloys*, P.S. Rudman, J. Stringer, and R.I. Jaffee, editors. (1967), McGraw Hill, New York.

CHAPTER 8: HCP → FCC TRANSFORMATION IN MECHANICALLY MILLED GROUP IV B ELEMENTS

8.1. Introduction

In the previous chapter (Ch.7), a hexagonal close-packed (HCP) to face-centered cubic (FCC) transformation in nanocrystalline hafnium was studied in detail. In addition to Hf, there have been reports and suggestions in recent times that the Group IVB elements Ti and Zr undergo a HCP to FCC transformation on mechanical milling of their powders [1-3]. Allotropic transformations have also been reported to occur in some other metals such as Co [4-5], Fe [6] and Nb [7-8]. Formation of an FCC Ti phase has also been reported in as-deposited multilayers of Ti and Al on ion milling in cross section [9-10]. Table 8.1 lists the structural details of these transformations along with the crystal structure data of the equilibrium phases [11-12].

Table 8.1: Crystal structure data for the equilibrium and metastable FCC allotrope phases formed in mechanically milled metals (Ref. [11-12]).

Metal	**Equilibrium crystal structure at room temperature**	**Lattice parameters**		**Lattice parameter of the FCC metastable allotrope (nm)**	**Minimum crystallite size (nm)**	**Ref.**
		***a* (nm)**	***c* (nm)**			
Ti	HCP	0.2951	0.4684	0.4356	5.3	7
				0.442	-	15, 16
Zr	HCP	0.3232	0.5148	0.4667	5.6	8
Hf	HCP	0.3195	0.5051	0.4566	7.0	9
Co	HCP	0.2507	0.4069	0.356	13	10, 11
Fe	BCC	0.2867	-	0.351	10	12
Nb	BCC	0.3300	-	0.441	6.6	13
				0.428	8	14

Among the several possibilities for the occurrence of these transformations, it has been suggested that metastable allotropic transformations could occur in metals when their grain sizes are reduced to nanometer levels [13-14]. Thus, the formation of an FCC phase in Group IV B elements and also in Co and Nb metals was explained on the basis that the grain sizes in the milled conditions were less than about 15 nm [5.3 nm for Ti [1], 5.6 nm for Zr [2], 13 nm for Co [4-5], and 7-8 nm for Nb [7-8]. An important result of mechanical milling is the formation of ultrafine grain sizes (down to the nanometer range) with significant lattice strain. The nanometer-sized grains in these mechanically milled powders also exhibited an increase in atomic volume. All these factors contribute to an increase in the free energy to a level higher than that of the equilibrium crystalline phase and consequently the metastable phase gets stabilized.

Some doubts have been expressed about the real nature of these transformations. While some researchers believe that these are true allotropic transformations, affected by a reduction in crystallite size down to less than about 15 nm, others believe that these new FCC phases are stabilized by interstitial impurities introduced during milling. As an example, an FCC phase was reported to form in mechanically alloyed Ti-Al alloys [15-16] and the powders were shown to contain about 32.6 at.% nitrogen. It was later shown by Suryanarayana [17] that the widely reported FCC phase in the Ti-Al system was neither a supersaturated solid solution of Ti and Al, nor a disordered γ-TiAl phase, but a B1 (NaCl-type) TiN phase, formed due to substantial contamination of the milled powder with nitrogen. Similar arguments were also extended to explain the formation of FCC phases in mechanically alloyed Zr [18] and Nb alloys [19]. It is also useful to note that the BCC → FCC allotropic transformation observed in mechanically

milled Nb [7-8] was not confirmed by Banerjee et al. [20], in their magnetron-sputtered thin films even though the grain size in these sputtered thin films was below 5 nm. Thus, it is doubtful if these allotropic transformations in mechanically milled metal powders are true transformations. This becomes even more serious when it is realized that mechanical milling of powders can introduce substantial amounts of impurities unless proper precautions are taken to prevent that from happening [21-22].

Even though convincing arguments have been put forward by both the rival groups to support their conclusions, the problem can be most easily resolved by milling the powders in an ultra-clean environment to minimize/avoid impurity pick-up and seeing whether the FCC phase still forms in these metals. If an FCC phase is produced under these high-purity conditions of milling also, it can then be concluded that this is a true allotropic transformation; otherwise it will be an impurity-stabilized phase. Thus, we report in this paper, our results on the mechanical milling of Group IV B elements Ti, Zr, and Hf in two different milling conditions – one regular and the other the ultra-high purity environment.

Group IV B metals Ti, Zr, and Hf exist in the HCP structure at room temperature and transform to the body-centered cubic (BCC) structure at elevated temperatures. There have not been any reports on the formation of an FCC phase in these metals either under equilibrium or non-equilibrium conditions, prior to the results obtained by mechanical milling, except in the case of Ti, where the HCP-Ti transformed to the FCC structure in multilayers during ion milling in cross section [9-10]. The crystal structure details of these metals under equilibrium conditions are listed in Table 8.2 [11-12].

Table 8.2: Crystal structure data of the equilibrium phases of Group IVB elements Ti, Zr, and Hf [12].

Phase	**Crystal structure (Prototype, Strukturbericht designation)**	**Pearson symbol**	**Space group**	**Lattice parameters**		**Comments**
				***a* (nm)**	**c (nm)**	
α-Ti	HCP (Mg, A3-type)	hP2	$P6_3/mmc$	0.2951	0.4684	-
β-Ti	BCC (W, A2-type)	cI2	$Im\bar{3}m$	0.3307	-	Stable above 882 ^oC
α-Zr	HCP (Mg, A3-type)	hP2	$P6_3/mmc$	0.3232	0.5148	-
β-Zr	BCC (W, A2-type)	cI2	$Im\bar{3}m$	0.3609	-	Stable above 863 ^oC
α-Hf	HCP (Mg, A3-type)	hP2	$P6_3/mmc$	0.3195	0.5051	-
β-Hf	BCC (W, A2-type)	cI2	$Im\bar{3}m$	0.3610	-	Stable above 1743 ^oC

8.2. Results

Figure 8.1 shows the XRD patterns of the Hf powder as a function of milling time, milled under regular conditions. The starting unmilled powder clearly showed the presence of sharp diffraction peaks, and all these peaks could be satisfactorily indexed on the basis of the equilibrium HCP structure and with the expected lattice parameters. On the other hand, XRD patterns of the milled powder exhibited broad diffraction peaks with lower intensities, caused by the combined effects of small grain sizes and lattice strain. The peak broadening increased with increasing milling time suggesting that, with milling time, the strain had increased and that the grain size had decreased to nanometer levels. In addition, new diffraction peaks started appearing after milling the powder for as short as 1 h. The equilibrium HCP phase, with reduced diffraction peak intensities, co-existed with the new phase, up to a milling time of 3 h. The HCP peaks, which are reasonably intense in the starting powder, only could be observed at milling

times of 1 to 3 h. When the powders were milled for 5 h, the XRD pattern showed only these new peaks and all the diffraction peaks characteristic of the HCP phase had disappeared. All the new peaks were most satisfactorily indexed on the basis of an FCC structure with the lattice parameter a = 0.4566 nm. No further structural changes were noted on further milling the powders to 10 h. Similar HCP → FCC phase transformations were noted in the Ti and Zr powders milled under regular conditions, noting that the time required for the formation of the FCC phase was 10 and 5 h, respectively for Ti and Zr.

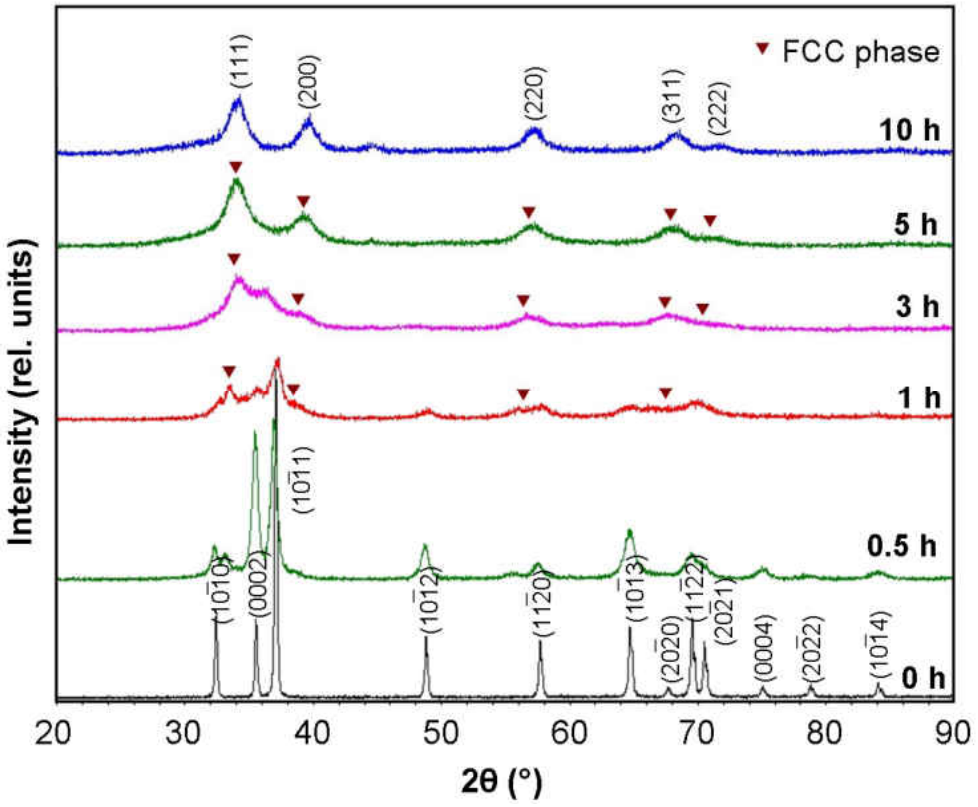

Figure 8.1: XRD patterns of the pure metal powder hafnium as a function of milling time up to 10 h, under regular conditions. While all the diffraction peaks at the expected positions and with the expected intensities characteristic of the HCP phase are present in the unmilled (0 h) powder, new peaks characteristic of an FCC phase started appearing on milling the powder for 1 h. The HCP → FCC phase transformation was complete at 5 h of milling.

Figure 8.2 shows the evolution of XRD patterns when the Hf powder was milled under ultra-high purity (UHP) conditions. The HCP structure, noted in the starting powder, continued to be present even after milling the powder for 10 h. The only perceptible changes in the patterns were a decrease in the peak intensity and increase in the width of the diffraction peaks; attributed to a decrease in the crystallite size and increase in lattice strain introduced into the powder during milling. In other words, when the Hf powder was milled under UHP conditions, no new phase had formed and the HCP → FCC allotropic phase transformation was not observed in the milled powder. Similarly, the HCP → FCC allotropic transformations were not observed in the milled Ti and Zr powders also, when milled under UHP conditions.

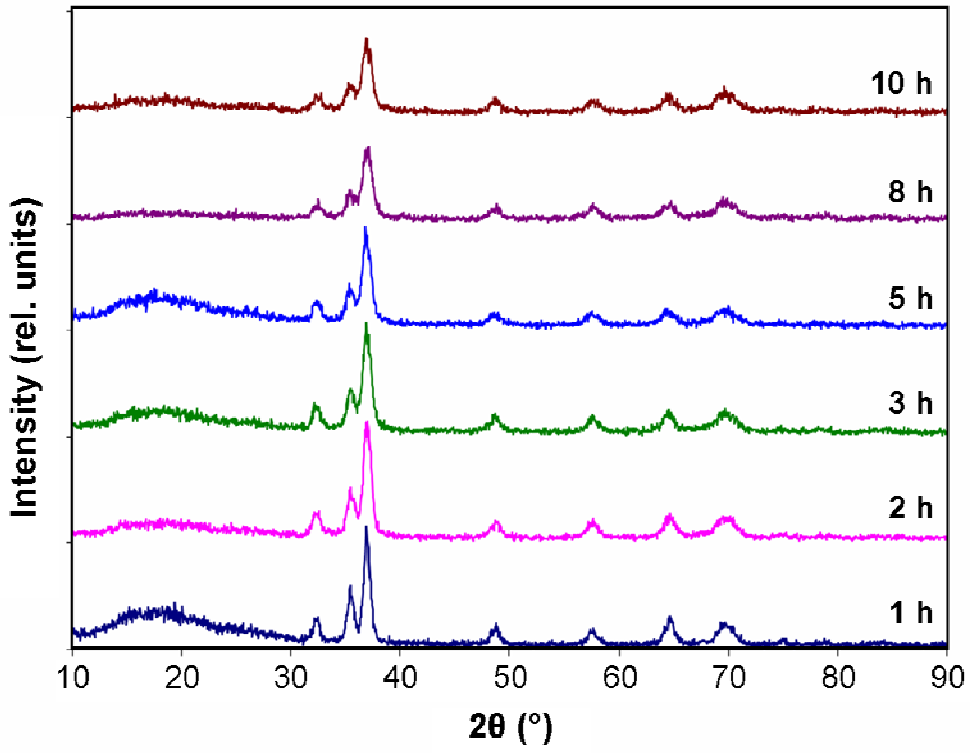

Figure 8.2: XRD patterns of Hf milled under ultra-high purity conditions for 10 h. No HCP → FCC phase transformation was noted during milling.

Figure 8.3 compares the XRD patterns of Ti, Zr, and Hf milled under both regular and UHP conditions. While the HCP → FCC transformation occurred in all the cases during regular milling, even though the time required for the formation of the FCC phase was different, there was no such transformation when the powders were milled under UHP conditions even after 25 h for Ti and Zr and 10 h for Hf. This observation clearly suggests that the formation of the FCC phase was not a result of the allotropic transformation, but is probably associated with possible impurities picked up during milling. One important difference in the powders milled under these two conditions, however, is that the crystallite size reached a minimum of 12, 10, and 9 nm for Ti, Zr and Hf, respectively during UHP milling, whereas they are 9, 4, and 3 nm, respectively, when milled under regular conditions and the FCC phase had formed.

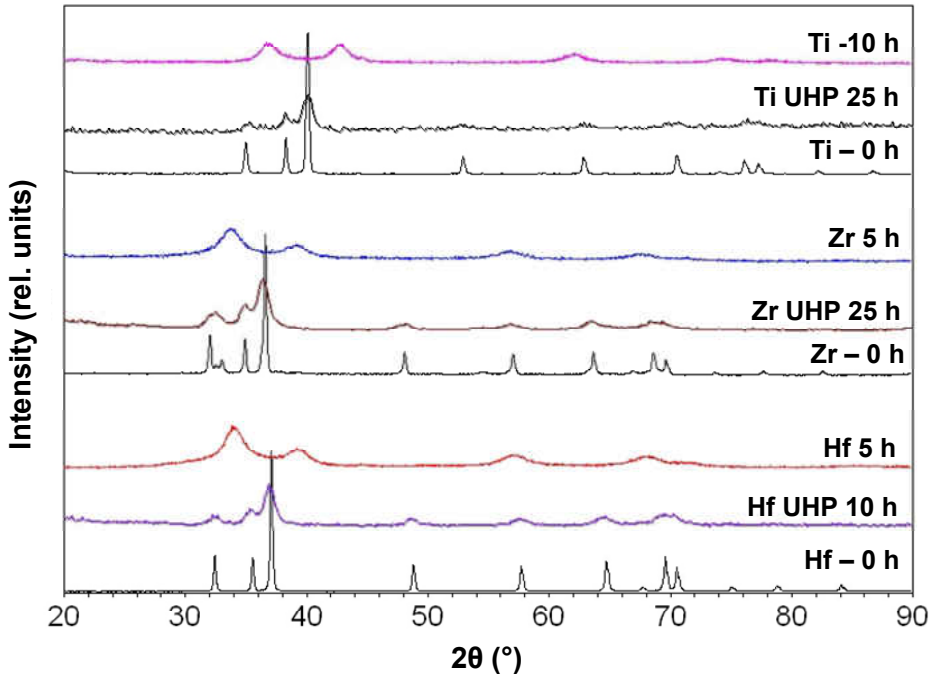

Figure 8.3: Comparison of the XRD patterns of Ti, Zr, and Hf powders in the as-received (0 h) and milled state under both UHP and regular milling conditions. While the FCC phase had formed in all the metals when milled under regular conditions, the FCC phase did not form under UHP conditions of milling.

8.3. Discussion

From the above results it is clear that an FCC phase had formed in the Ti, Zr, and Hf powders when they were milled under regular conditions and that it did not form when these powders were milled under UHP conditions. Therefore, it becomes important to decide why the FCC phase had formed when milled only under regular conditions and not under UHP conditions, and whether this is a true allotropic transformation.

One important difference noted between the two sets of powders was that the minimum grain size achieved was lower when the powders were milled under regular conditions. Even though the difference in the minimum grain size for any metal, under the two conditions of milling, was small, the smaller grain size in the regular-milled condition can be ascribed to the probable incursion of air or other gaseous impurities into the vial during milling. This air could have acted like a process control agent covering the surface layers of the powder particles which would have prevented excessive cold welding resulting in more fracture events and eventually formation of smaller grain sizes.

Allotropic phase transformations in pure metals can occur due to changes in temperature, pressure, or alloying additions. Additionally, changes in microstructural parameters such as grain size, surface energy, and stacking-fault energy can have a significant effect in affecting these transformations. There are no reports of stable FCC phases at higher temperatures or pressures in the metals Ti, Zr, and Hf studied in the present investigation. Therefore, irrespective of the temperatures and pressures generated in the milling process, one cannot understand the formation of the FCC phases as a result of the allotropic transformation under metastable

conditions. But, it is possible that the FCC phases themselves are completely metastable existing at room temperature and pressure.

It has been known that nanostructure processing could result in the formation of unusual phases in metallic systems. Therefore, it is possible that the powders with nanometer grain sizes could lead to the formation of new phases such as new allotropes. Kaufman [23] has suggested that a free energy value of 800 cal/mol (about 0.04 eV/atom) was required for the hypothetical HCP → FCC transformation to occur in Ti, Zr, and Hf metals. Based on the equation-of-state model [24-25], it was calculated that this amount of energy could be stored in a metal by decreasing its grain size to a value of 16.2, 19.1, and 18.7 nm for Ti, Zr, and Hf, respectively [3]. From our investigation on milling the powders under UHP conditions, the minimum grain sizes obtained were 12, 10, and 9 nm, respectively for Ti, Zr, and Hf. Since these values are well below the values of 16.2 nm (for Ti), 19.1 nm (for Zr) and 18.7 nm (for Hf) calculated above, and also because no HCP → FCC transformation occurred under UHP conditions of milling, it is reasonable to conclude that the transformations observed in these powders are not true allotropic transformations brought about by reducing their grain sizes down to nanometer levels. It was also noted earlier that the FCC phase attributed to the allotropic transformation in milled Nb and Nb-alloys [7-8] was not present in magnetron-sputtered thin films of Nb [20]. Thus, the reason for the formation of the FCC phase in these metals has to be different from the allotropic transformation.

The main difference in the processing of powders under the regular and UHP conditions of milling is the milling environment and the possible contamination of the milled powder by interstitial impurities. There is no chance for gaseous contaminants to enter into the powder

during UHP milling conditions since the atmosphere both inside the vial and outside the vial and the mill is also inert. But, during regular milling, the environment outside the vial is air, and, in spite of the "tight" sealing of the lid on the vial, a strong possibility exists for the powder to pick up interstitial elements such as nitrogen and oxygen from the air ambient surrounding the vial. This pick up will be much more significant due to the nanocrystalline nature of the milled powder which has a larger surface area.

Results of conventional wet chemical analysis of the powder milled under regular conditions are presented in Table 8.3. It may be noted that substantial amount of impurities are present in all the three powders. On the other hand, the amount of impurities present in the powders milled under UHP conditions was insignificant; it just amounted to the interstitial impurity content present in the starting powders. From these observations, it becomes apparent that it is most likely that the FCC phases observed in these milled powders are impurity-stabilized.

Table 8.3: Interstitial contamination levels of the milled Ti, Zr, and Hf powders

Metal	**Milling time (h)**	**N (at.%)**	**O (at.%)**	**C (at.%)**
Ti	15	6.4	9.4	2.3
Zr	5	8.8	11.7	3.2
Hf	5	12.0	11.8	9.0

All the metals used in the present investigation are reactive in nature. They can easily combine with elements such as hydrogen, oxygen, carbon, and nitrogen and form hydrides, oxides, carbides, and nitrides. Majority of these interstitial compounds have a cubic structure and therefore it is possible that the FCC phases observed in these metal powders could be one of these interstitial phases. Table 8.4 summarizes the crystal structure data of the cubic interstitial phases that can form with Ti, Zr, and Hf [11-12].

Table 8.4: Crystal structure data for the equilibrium interstitial cubic compounds that form between Ti, Zr, and Hf and hydrogen, carbon, nitrogen, and oxygen (Ref. [11-12])

Phase	**Crystal structure (Prototype, Strukturbericht designation)**	**Pearson symbol**	**Space group**	**Composition range of stability (at.%)**	**Lattice parameter (nm)**
δ-TiH_2	FCC (CaF_2, C1-type)	cF12	$Fm\bar{3}m$	50 – 66.7 at.% H	0.4431
δ-ZrH_2	FCC (CaF_2, C1-type)	cF12	$Fm\bar{3}m$	56.7 – 66.4 at.% H	0.4779
HfH_2	FCC (CaF_2, C1-type)	cF12	$Fm\bar{3}m$	24 – 64 at.% H	0.4681
TiC	FCC (NaCl, B-1 type)	cF8	$Fm\bar{3}m$	~32 – 48.8 at.% C	0.4327
ZrC	FCC (NaCl, B-1 type)	cF8	$Fm\bar{3}m$	33 – 50 at.% C	0.4698
HfC	FCC (NaCl, B-1 type)	cF8	$Fm\bar{3}m$	37.5 – 49.5 at.% C	0.4633
TiN	FCC (NaCl, B-1 type)	cF8	$Fm\bar{3}m$	28 – 50 at.% N	0.4239
ZrN	FCC (NaCl, B-1 type)	cF8	$Fm\bar{3}m$	40 – ? at.% N	0.4573
HfN	FCC (NaCl, B-1 type)	cF8	$Fm\bar{3}m$	46 – 52.5 at.% N	0.4525
γ-TiO	FCC (NaCl, B-1 type)	cF8	$Fm\bar{3}m$	34.9 – 55.5 at.% O	0.4177
γ-ZrO_2	FCC (CaF_2, C1-type)	cF12	$Fm\bar{3}m$	61 – 66.6 at.% O	0.5114
HfO_2	FCC (CaF_2, C1-type)	cF12	$Fm\bar{3}m$	~63 – 67 at.% O	0.5115

Among these, the hydride phases have a fluorite (CaF_2)-type crystal structure and the hydrogen content required for the formation of these phases is really large. Further, the lattice parameters of these hydride phases are larger than the lattice parameters of the FCC phases observed in the present investigation. Since milling was conducted under dry conditions, it is impossible for the powder to absorb so much of hydrogen and so the possibility of the FCC phase in the Ti, Zr, and Hf powders being a hydride can be discounted.

Similarly, formation of the oxide phases also needs large amounts of oxygen (more than 61 at.% in the case of Zr and Hf and a minimum of 35 at.% in the case of Ti). The lattice parameters of these phases are much larger than the values observed in the present investigation. Therefore, the possibility of the FCC phases in the present investigation being the oxide impurity phases can also be ruled out.

Yet another possibility for the FCC phase observed in the present study is that they could be either the carbides or nitrides of the respective elements. Even though these phases also require large amounts of carbon or nitrogen, the lattice parameters of these phases (Table 8.4) are much closer to the values obtained in the present study. Therefore, let us look at this possibility a little more closely.

It is interesting that the lattice parameters of the FCC phases observed in the milled Ti, Zr, and Hf powders are very close to those of the corresponding nitride phases, as presented in Table 8.5 [12]. In fact, the lattice parameter of the FCC phase observed in Ti and Zr is almost exactly equal to those of the corresponding nitride phases. In the case of Hf metal, the lattice parameter of the HfN phase is slightly smaller than that of the FCC phase observed. The lattice parameters of the carbide phases also are not very different; they are slightly larger than the

lattice parameters of the FCC phases. Further, the carbide and nitride phases have a B1 (NaCl-type) FCC structure. Since nitrogen could be incorporated into the powder due to air ingress into the vial during milling, and carbon can be incorporated into the powder through the process control agent used (stearic acid) in the regular milling condition, the FCC phase in the milled powders can be either the carbide or nitride or a combination of both. Detailed calculations for the diffraction intensities of the carbide and nitride phases of Hf have been performed and it was shown that the intensities of the observed FCC phase in the milled Hf powder cannot be predicted on the basis of it being either only HfC or HfN. Considering the results of wet chemical analysis, and comparing the lattice parameter of the FCC phase with those of HfC and HfN, it was concluded that the observed FCC phase could be best described as a mixture of the HfN and HfC phases. The suggested chemical formula for the FCC phase in the milled Hf powder was $Hf(C_{0.4}N_{0.6})$. Since the Group IV B elements are expected to behave in a similar fashion, it is possible that the FCC phases observed in the milled Ti and Zr powders also could be either the nitrides or carbides or a combination of both, i.e., carbonitrides.

Table 8.5: Crystal structure data of the nitride phases formed in Ti, Zr, and Hf, and the FCC phases formed in the present investigation when the powders were milled under regular conditions. (Ref. [12])

Base metal	**Phase**	**Crystal structure**	**Lattice parameter (nm)**	**Ref.**
Ti	Observed allotrope phase	FCC	0.4238	Present investigation
	Observed allotrope phase	FCC	0.4356	[1]
	TiN*	FCC	0.4244	[12]
	TiC*	FCC	0.4327	[12]
Zr	Observed allotrope phase	FCC	0.4588	Present investigation
	Observed allotrope phase	FCC	0.4677	[2]
	ZrN*	FCC	0.4585	[12]
	ZrC*	FCC	0.4698	[12]
Hf	Observed allotrope phase	FCC	0.4566	Present investigation
	HfN*	FCC	0.4525	[12]
	HfC*	FCC	0.4633	[12]

*These phases have an NaCl, B1-type cubic structure with the space group $Fm\bar{3}m$ and their Pearson symbol is cF8.

However, as discussed in previous chapter (Ch.7), the minimum nitrogen content required to homogeneously form these nitride phases is much higher than the observed values. The situation is the same with respect to the carbon content. Even if the FCC phase were considered as the carbonitride phase, at least in the case of Hf powder, the available carbon and nitrogen contents will be sufficient to transform only about 50% of the powder to the

carbonitride FCC phase. But, since we have only one FCC phase in the powders milled under regular conditions, and also because these FCC phases are not formed when the powders were milled under UHP conditions, it is possible that the FCC phase has initially formed, due to powder contamination, with the required nitrogen and/or carbon content in part of the milled powder and then the remaining portion of the powder also got stabilized into the FCC structure under the non-equilibrium conditions of milling. It is possible that the FCC phase had acted as a nucleating agent for the remaining powder to transform to the FCC phase. A similar transformation was reported to occur during milling of γ-Al_2O_3 powders [26].

Because if the shear and impact forces experienced by the grinding balls during mechanical milling, there could be wear and tear of the grinding balls. Additionally, because of the impact of the balls against the inner walls of the milling container, the container may also get eroded. Due to these effects, it is also possible that the milled powder contains Fe, Cr and/or Ni since stainless steel balls and container were used. This possibility can be completely ignored for the following three reasons. Firstly, the milling times are relatively short and the ball-to-powder weight ratio (10:1) is moderate. Under these conditions, the powder contamination is expected to be low, and is usually < 1 at.% [21-22]. Secondly, the intermetallic phases that can form between Fe, Cr, and Ni with Ti, Zr, or Hf have either the fluorite-type (cF24) phases or the cF96 (the so-called big cube) phases. The lattice parameters of these phases are very large and larger than the lattice parameters of the FCC phases observed in the present investigation. Lastly, the milling conditions (time, ball-to-powder weight ratio, and the milling tools) are the same in both the regular milling and UHP milling conditions. The FCC phases of the powders are observed only under regular milling conditions and not otherwise. If the FCC phase were to be an intermetallic between Ti, Zr, or Hf and Fe, Cr, or Ni, it should have formed under both the

conditions of milling. The absence of the FCC phase in the powders milled under UHP conditions suggests that contamination of the powders by substitutional elements from the milling tools is not responsible for the formation of this phase.

From the above detailed discussion it becomes clear that the mechanism for the formation of the FCC phases in Group IV B metals (Ti, Zr, and Hf) is neither allotropic transformation obtained by reducing grain size nor the respective nitrides, carbides or oxides. Thus, it is possible that the FCC phases observed in these studies are impurity-stabilized, at least partially. This conclusion is supported by the fact that the FCC phases were not observed when these powders were milled under ultra-high purity conditions.

8.4. Conclusions

From the above results and the discussion, it is clear that the HCP → FCC allotropic transformation in the milled Group IVB metals Ti, Zr, and Hf is not a pure allotropic transformation, and is stabilized by contamination of the milled powder. From the strong evidence presented here, the occurrence of such a transformation can only be attributed to significant contamination of the milled powder by FCC-phase-forming elements such as nitrogen and carbon. This conclusion is strengthened by the observation that such an FCC phase formation was not present when the powders were milled under ultra-high purity conditions, where contamination is completely avoided. Thus, reports of allotropic or other phase transformations in pure metals, especially the reactive metals, have to be viewed carefully and the possibility of powder contamination has to be first discounted.

8.5. References

1. I. Manna, P.P. Chattopadhyay, P. Nandi, F. Banhart, and H.J. Fecht, Formation of face-centered-cubic titanium by mechanical attrition, Journal of Applied Physics, 93 (2003), p.1520
2. I. Manna, P.P. Chattopadhyay, F. Banhart, and H.J. Fecht, Formation of face-centered-cubic zirconium by mechanical attrition, Applied Physics Letters, 81 (2002), p.4136
3. U.M.R. Seelam and C. Suryanarayana, Mechanically induced fcc phase formation in nanocrystalline hafnium, Journal of Applied Physics, 105 (2009), p.063524
4. J.Y. Huang, Y.K. Wu, H.Q. Ye, and K. Lu, Allotropic transformation of cobalt induced by ball milling, Nanostructured Materials, 6 (1995), p.723
5. J.Y. Huang, Y.K. Wu, and H.Q. Ye, Allotropic transformation of cobalt induced by ball milling, Acta Materialia, 44 (1996), p.1201
6. L. Del Bianco, C. Ballesteros, J.M. Rojo, and A. Hernando, Magnetically ordered fcc structure at the relaxed grain boundaries of pure nanocrystalline Fe, Physical Review Letters, 81 (1998), p.4500
7. P.P. Chatterjee, S.K. Pabi, and I. Manna, An allotropic transformation induced by mechanical alloying, Journal of Applied Physics, 86 (1999), p.5912
8. P.P. Chattopadhyay, S.K. Pabi, and I. Manna, A metastable allotropic transformation in Nb induced by planetary ball milling, Materials Science and Engineering A, 304-306 (2001), p.424
9. D. Shechtman, D. Van Heerden, and D. Josell, FCC titanium in Ti-Al multilayers, Materials Letters, 20 (1994), p.329
10. D. Van Heerden, D. Josell, and D. Shechtman, The formation of fcc titanium in titanium-aluminum multilayers, Acta Materialia, 44 (1996), p.297
11. T.B. Massalski, ed., Binary Alloy Phase Diagrams 2nd edition (1990), ASM International, Ohio.
12. P. Villars and L.D. Calvart, eds. Pearson's Handbook of Crystallographic Data for Intermetallic Phases, 2nd. ed. (1991), ASM International, Materials Park, Ohio.

13. C. Suryanarayana, Nanocrystalline materials, International Materials Reviews, 40 (1995), p.41
14. C.C. Koch, ed., Nanostructured materials, 2nd. edition (2007), William Andrew, Norwich, NY.
15. W. Guo, S. Martelli, N. Burgio, M. Magini, F. Padella, E. Paradiso, and I. Soletta, Mechanical alloying of the Ti-Al system, Journal of Materials Science, 26 (1991), p.6190
16. W. Guo, S. Martelli, F. Padella, M. Magini, N. Burgio, E. Paradiso, and U. Franzoni, FCC. metastable phase induced in the Ti-Al system by mechanical alloying of pure elemental powders, Materials Science Forum, 88-90 (1992), p.139
17. C. Suryanarayana, Does a disordered γ-TiAl phase exist in mechanically alloyed Ti-Al powders?, Intermetallics, 3 (1995), p.153
18. H.J. Fecht, G. Han, Z. Fu, and W.L. Johnson, Metastable phase formation in the Zr-Al binary system induced by mechanical alloying, Journal of Applied Physics, 67 (1990), p.1744
19. Z. Peng, C. Suryanarayana, and F. Froes, Mechanical alloying of Nb-Al powders, Metallurgical and Materials Transactions A, 27 (1996), p.41
20. R. Banerjee, E.A. Sperling, G.B. Thompson, H.L. Fraser, S. Bose, and P. Ayyub, Lattice expansion in nanocrystalline niobium thin films, Applied Physics Letters, 82 (2003), p.4250
21. C. Suryanarayana, Mechanical alloying and milling, Progress in Materials Science, 46 (2001), p.1
22. C. Suryanarayana, Mechanical Alloying and Milling (2004), Marcel Dekker, New York.
23. L. Kaufman, in *Phase Stability in Metals and Alloys*, P.S. Rudman, J. Stringer, and R.I. Jaffee, editors. (1967), McGraw Hill, New York.
24. J.H. Rose, J.R. Smith, F. Guinea, and J. Ferrante, Universal features of the equation of state of metals, Physical Review B, 29 (1984), p.2963
25. H.J. Fecht, Thermodynamic properties and stability of grain boundaries in metals based on the universal equation of state at negative pressure, Acta Metallurgica et Materialia, 38 (1990), p.1927
26. Y. Wang, C. Suryanarayana, and L. An, Phase transformation in nanometer-sized g-alumina by mechanical milling, Journal of the American Ceramic Society, 88 (2005), p.780

CHAPTER 9: CONCLUDING REMARKS

In the summary of the study, microstructure, crystal structure, grain size, and phase formation were studied in the four sputter-deposited SS304+Al coatings (SS304+0Al, SS304+4Al, SS304+7Al and SS304+10Al coatings) and in the mechanically milled Hf, Ti and Zr powders.

The grain size of the SS304+Al varied widely from as small as 20 nm to as high as 3 μm. Such a large variation was attributed mainly to the variation in normalized deposition temperatures from less than 78 °C in SS304+0Al coating to greater than 416 °C in 10Al coating as identified from their grain structure zones. Any conclusions on the effect of Al on grain size could not be drawn as there was a huge variation in deposition temperature. The variation is due to the possible temperature differences (zones of different temperatures) in the sputtering chamber. This critical finding, of the presence of temperature zones in the sputtering chamber that are leading to variable deposition temperatures in the coatings, is a significant contribution of the present work.

Another critical point that the present study identified was the consistent Ni depletion in the coatings deposited from SS304 target. In the case of SS304+0Al coating, while the actual Ni content should be about 8 wt.%, the coating showed only about 7 wt.% Ni. This depletion in Ni directly had an influence in phase formation. Formation of ferrite and sigma phases in the SS304+0Al coating was related to the Ni depletion issue. The Ni depletion was observed in the SS304+4, 7 and 10Al coatings as well.

Metastable phases were found in both the sputter deposition of coatings and in the mechanical milling of powders. In the sputter deposited SS304+Al coatings, ferrite and sigma

phases were the two non-equilibrium phases obtained in Al-free SS304 coatings. Ferrite and B2 phases in SS304+4, 7 and 10Al coatings were the equilibrium phases. The main reason for the formation of ferrite in SS304+0Al coating was the depletion of Ni during sputter deposition. One of the main causes for the formation of sigma phase however appear to be the consistent localized Ni depletion and Cr enrichment which enhance interactions between Fe and Cr. The second cause could be a possible strain relief mechanism that is believed to be driving the phase transformation. Formation of the intermetallic phase sigma is still an evolving story and needs further understanding.

Another crucial finding of this investigation was the nano layers of about 3 to 4 nm. The layered structure was obtained as a result of using the two targets, SS304 and Al. This layered structure and the compositional fluctuations are something that cannot be avoided if two targets are used together with substrate rotation. Since such compositional fluctuations in the layers are relatively minor, this may not be as serious a problem as that of the deposition temperatures. However, this aspect is worth addressing while designing any new compositions for coatings.

The B2 phase and layered structure were closely related to each other. While one of layer was observed to be having NiAl, the other layer consisted of ferrite. Hence it was clear that NiAl was the preferred phase over FeAl phase.

In the metastable phases in mechanical milling of Ti, Zr and Hf powders, the FCC phase in the elemental Hf was found out to be based on Hf, but not any Hf allotrope, HfN, HfC or Hf(CN). It is an impurity-stabilized Hf based FCC phase. The same is true in the case of Ti and Zr as well. The FCC phases in milled Ti and Zr are not their respective allotropes, nitrides, carbides, or oxides. The HCP to FCC transformation in these metals was not an allotropic

transformation. It was impurity-stabilized transformation associated with formation of nanocrystalline grains and possibly strain induced during milling. This study shows the importance of ultra high purity environment during milling of the high reactive metals.

APPENDIX

List of Publications and Conference Presentations

Publications

- U.M.R. Seelam and C. Suryanarayana, "Mechanically-Induced FCC Phase Formation in Nanocrystalline Hafnium", J. Appl. Phys., 105 (2009), pages 063524 (1-8)
- Uma M.R. Seelam, G. Barkhordarian and C. Suryanarayana, "Is there a hcp → fcc allotropic transformation in mechanically milled Group IV B elements (Titanium, Zirconium and Hafnium)?", J. Mater. Res., 24 (2009), pages 3454-3461

Conference Presentations

- U.M.R. Seelam, N.S. Cheruvu and C. Suryanarayana, "Microstructure and Oxidation Resistance of Magnetron Sputtered 304 Stainless Steel", Materials Science & Technology 2009, (MS&T'09) Pittsburgh, PA (Oct. 25-29, 2009)
- U.M.R. Seelam, T. Ohkubo, K. Hono and C. Suryanarayana, "Microstructure of Magentron Sputtered 304 Stainless Steel+10Al Coating", International Symposium of Research Scholars (ISRS) 2008, IIT-Chennai, India (Dec. 10-12, 2008)
- U.M.R. Seelam, N.S. Cheruvu and C. Suryanarayana, "Effect of Al on the Microstructure of Stainless Steel + Al Sputter-deposited Coatings", MS&T'08, Pittsburgh, PA (Oct. 5-9, 2008)
- U.M.R. Seelam and C. Suryanarayana, "Mechanically Induced Allotropic Transformation in Nanocrystalline Hafnium", MS&T'07, Detroit, MI (Sep. 16-20, 2007)